Spin-Crossover Modulated Luminescence in Materials and Molecular Complexes

Glaus, Charlotte; Piguet, Claude

How to cite

GLAUS, Charlotte, PIGUET, Claude. Spin-Crossover Modulated Luminescence in Materials and Molecular Complexes. In: Helvetica chimica acta, 2026, vol. 109, n° 2, p. e00180. doi: 10.1002/hlca.202500180

This publication URL: https://archive-ouverte.unige.ch/unige:191681
Publication DOI: 10.1002/hlca.202500180

Helvetica Chimica Acta

HELVETICA chimica acta

REVIEW OPEN ACCESS

Spin-Crossover Modulated Luminescence in Materials and Molecular Complexes

Charlotte Egger | Claude Piguet

Department of Inorganic and Analytical Chemistry, University of Geneva Faculty of Science, Geneva, Switzerland

Correspondence: Charlotte Egger (charlotte.egger@unige.ch) | Claude Piguet (claude.piguet@unige.ch)

Received: 10 October 2025 | **Revised:** 3 December 2025 | **Accepted:** 4 December 2025

Keywords: iron | ligand design | luminescence | N ligands | spin crossover

ABSTRACT

The abrupt reorganization of the electronic configuration of spin-crossover (SCO) compounds upon the transition from the low-spin (LS) to the high-spin (HS) state leads to significant changes in their structural, optical, and magnetic properties. As spin-transitions can be triggered by a variety of external stimuli such as variations in temperature, pressure, or through light irradiation, these systems have attracted considerable attention for the design of multifunctional and stimuli-responsive molecular materials. In this context, the synergistic coupling of SCO and luminescent properties holds great promise for the development of molecular spintronic devices capable of correlating the luminescence with an external perturbation, or of probing the magnetic state of the metal center through variations in emission intensity. This contribution provides a comprehensive overview of the field of luminescent SCO materials, with particular emphasis on systems that exhibit a genuine interplay between the two properties, both in materials and at the molecular level.

1 | Introduction

Nearly a century after the pioneering work of Cambi and co-workers [1–3] on Fe(III) complexes with dithiocarbamate ligands led to the first experimental demonstration of what is now known as the spin-crossover (SCO) phenomenon, countless examples of molecular systems displaying spin-state equilibria have been, and are still actively being reported [4–7]. At first, the search for coordination complexes exhibiting magnetic bistability was tedious, but the development of the ligand-field theory in the 1950s [8], followed by decades of methodical investigations, eventually provided a reasonable understanding of the influence of both chemical modifications and physical perturbation on the SCO process. With this body of knowledge at hand, researchers in the field developed a growing interest in designing practical applications based on SCO compounds. The sudden reorganization of their electronic density in response to various external stimuli indeed bore great potential for the realization of molecule-based electronic and spintronics components, such as switching and memory devices [9, 10]. Moreover, the fact that numerous properties are affected by the spin-transition (magnetic susceptibility, dielectric permittivity, mass density, color, refractive index, and elastic moduli) [11] suggests that SCO complexes may be easily combined with a variety of other chemical or physical properties in a synergistic fashion, hence paving the way toward multifunctionality.

Among these various properties, luminescence stands out as an appealing candidate as it offers superior contrast and sensitivity compared to the techniques usually employed in the SCO field (magnetometry, differential scanning calorimetry, and optical absorption) [12], as well as high spatial and temporal resolution that can go down to the single molecular level [13]. In addition, a synergistic relationship between luminescence and SCO would

Dedicated to Professor Andreas Hauser who taught us photophysics coupled with spin-crossover.

afford the dual possibility of (i) probing the magnetic status of the metal center through a variation in luminescence intensity, or reversibly (ii) tuning the luminescence intensity with an external stimulus that would otherwise have a limited effect [11, 14]. All these benefits expand the scope of possible applications to new fields such as nanothermometry [15] and data storage [16]. In this context, substantial efforts have been invested in the search for molecule-based functional materials that undergo spin transitions while exhibiting detectable changes in their luminescent properties. All the attempts reported until now have followed one of two main strategies. The first one consists of physically mixing the luminescent and SCO moieties by doping an existing SCO material with a luminophore. The second one aims at combining the luminophore and the SCO unit in a single molecular entity, either by using a luminescent ligand or by covalently binding a luminophore to the SCO complex [12]. While these attempts have led to significant advancements, and a handful of systems have even proven successful, the design of luminescent spin-crossover materials remains a formidable challenge. One of the main hurdles lies in the preservation of both properties. The simultaneous integration of both functionalities in a common structure indeed risks significantly altering, or even losing one or both properties in an unpredictable manner [12]. Furthermore, even if the hybrid material displays the expected luminescent and SCO properties, there is no guarantee that they will be effectively correlated.

This review aims to present a comprehensive overview of the field, highlighting the advantages and drawbacks of the different synthetic approaches. The discussion will first address some fundamental aspects of the ligand-field theory, then provide some insights into the different energy transfer mechanisms, before reviewing the design and characterization of these innovative systems in both materials and molecular complexes.

2 | Theoretical Aspects of the Spin-Crossover Process

2.1 | Ligand-Field Considerations

Transition metal ions are characterized by their partially filled d orbitals, designated as d_{xy}, d_{yz}, d_{xz}, $d_{x^2-y^2}$, and d_{z^2} based on their orientation with respect to the Cartesian coordinate axis. In the absence of any potential or in a spherically symmetric field, all five d orbitals have the same energy. In coordination complexes, the non-spherical electric field formed by the donor atoms of the approaching ligands lifts the degeneracy. The energy of the newly formed molecular orbitals depends on the strength of the interaction between the ligands and the metal, which is heavily influenced by their relative orientation. In the case of an octahedral coordination sphere, stronger interactions arise with the d orbitals oriented along the bond axis ($d_{x^2-y^2}$ and d_{z^2}) than with those directed between these axes (d_{xy}, d_{yz}, and d_{xz}). As a result, the orbitals are split into two sets: a triply degenerate t_{2g} set at lower energy, and a doubly degenerate e_g* set at higher energy (Figure 1).

The energy difference between the two sets, known as the ligand-field splitting energy Δ (Δ_o in octahedral geometries), varies with the nature of both the metal and the ligands. For octahedral metal ions with electronic configurations d^1–d^3 and d^8–d^{10}, there is only one possible way of filling the d orbitals in an octahedral geometry, and the ligand-field strength has no influence on the distribution of electrons within the non-degenerate sets. In contrast, d^4–d^7 metal ions in octahedral geometry can exist in either a low-spin (LS) or a high-spin (HS) configuration depending on the relative values of the ligand-field splitting parameter Δ_o and the spin-pairing energy P, which represents the electrostatic penalty associated with the pairing of two electrons of opposite spins in the same orbital. When $\Delta_o > P$, the ligand-field stabilization energy (LFSE) overcomes the energetic cost associated with the pairing of electrons in the low-energy t_{2g} set, resulting in a LS configuration. Conversely, when $\Delta_o < P$, the limited LFSE cannot compensate for the electrostatic repulsion, and the distribution of unpaired electrons between the t_{2g} and e_g* sets becomes more favorable, hence leading to a HS configuration. The energy of each configuration relative to that of the spherical field can be easily calculated by summing all the stabilizing and destabilizing contributions, as shown in Figure 2 for a Fe(II) cation with a $3d^6$ configuration.

When the energy difference ΔE between the LS and the HS configuration is comparable with thermal energy (mRT, where m is a number such that $0 \leq m \leq 8$), the two spin-states can coexist at a given temperature [17, 18]. The reversible interconversion between these two electronic arrangements is referred to as the spin-crossover (SCO) phenomenon. This process is limited to a narrow range of ligand-field strengths, comprised between 11,000 and 12,500 cm^{-1} for an HS configuration, and between 19,000 and 22,000 cm^{-1} for an LS configuration [19]. The existence of a discontinuity between these two domains can be rationalized by the fact that the ligand field strength depends on the metal–ligand distance r, as shown in Equation (1):

$$\Delta_o \approx \frac{\mu}{r^6} \tag{1}$$

where μ is the dipole moment of the ligand [20]. During a thermal spin-transition (from the enthalpically favored LS state to the entropically favored HS state), r lengthens by circa 10% as a result of the population of the antibonding e_g* orbitals [4], which leads to a decrease in the ligand-field strength by a factor of approximately 1.75 (Equation 2) [19, 20]. This concomitant change in r and Δ_o implies that there exists a range of ligand-field strength that cannot be accessed, as the resulting complex would have a non-equilibrium geometry (i.e., one that does not correspond to a potential minimum).

$$\frac{r_{HS}}{r_{LS}} = 1.1 \approx \left(\frac{\Delta_o^{LS}}{\Delta_o^{HS}}\right)^{\frac{1}{6}} \Rightarrow \frac{\Delta_o^{LS}}{\Delta_o^{HS}} \approx 1.75 \tag{2}$$

The complete ligand-field picture is provided by the Tanabe–Sugano diagram for a d^6 configuration, which represents the relative energies of all the ^{2S+1}L terms as a function of the ligand-field strength (Figure 3) [21]. Both E and Δ_o are expressed in units of the Racah parameter B, which measures the intensity of the metal-centered electron-electron repulsion in the complex. Small values of Δ_o/B are thus associated with pure HS configurations (yellow area in Figure 3), whereas large Δ_o/B ratios are characteristic of pure LS configurations (purple area in Figure 3). Solving $\Delta E = 0 \pm 8\ RT$ by substituting Equation 2 into $\Delta E = \frac{12}{5}\Delta_o^{LS} -$

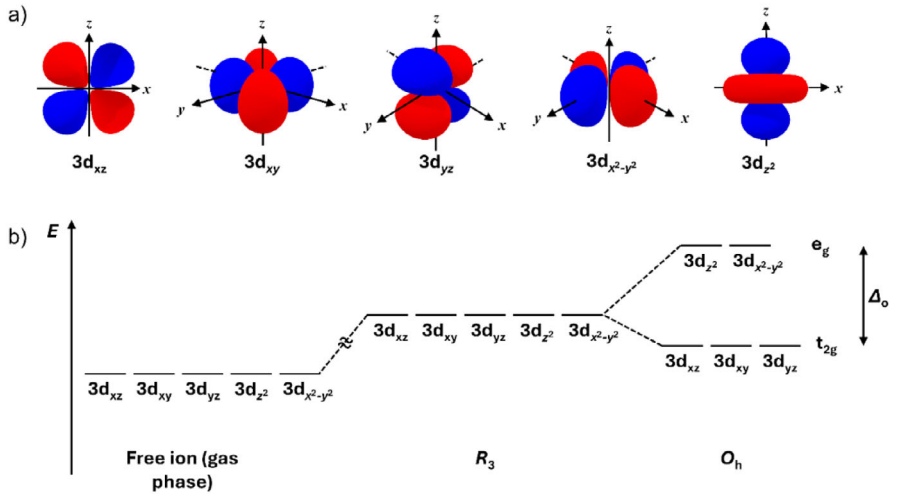

FIGURE 1 | Representation of (a) the boundary surface of the five d orbitals, highlighting the orientation of the lobes with respect to the Cartesian coordinate axis and (b) their energies in environments of decreasing symmetry.

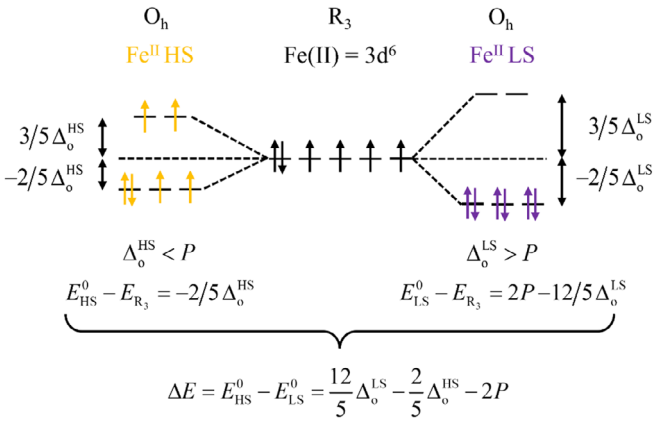

FIGURE 2 | Octahedral ligand field splitting diagram for the HS (weak field) and LS (strong field) ground-state configurations of Fe(II) complexes.

$\frac{2}{5}\Delta_o^{HS} - 2P$ provides the ligand-field domains compatible with the induction of a thermal spin-transition mentioned previously. Using the Racah parameters B and C to model P as $P = 2B + 4C \approx 19B$ [19], these domains can be written in units of B as $\Delta_o^{HS}/B = 10 \pm 0.5$ and $\Delta_o^{LS}/B = 17.5 \pm 1$ (green areas in Figure 3) [22]. The intervening domain, comprised between $10.5 < \Delta_o/B < 16.5$, corresponds to the inaccessible range where coordination complexes cannot exist in the ground-state due to the abrupt change in Δ_o during the spin-transition (red area in Figure 3).

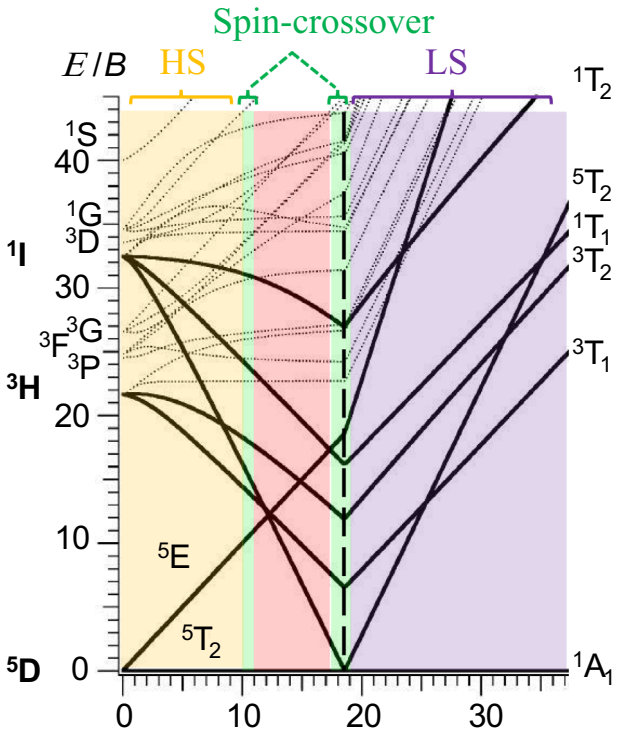

FIGURE 3 | Tanabe–Sugano diagram for a d^6 electronic configuration, highlighting in green the domains where HS and LS complexes coexist at accessible temperatures, and in red the non-accessible ligand-field strengths. The yellow and purple areas correspond to pure HS and LS configurations, respectively. Adapted from ref [21] with permission from the Royal Society of Chemistry.

2.2 | Electronic Properties of Spin-Crossover Complexes

The sudden reorganization of the electronic density during the SCO process has a significant impact on the structural, magnetic, and optical properties of the complex. As mentioned in the previous section, the population of the antibonding e_g^* orbitals in the HS state leads to an elongation of the metal–ligand bonds that usually results in a notable distortion of the octahedral coordination sphere. These structural changes, in turn, have consequences for the physical properties of the system. In solution, the increase in the volume of the coordination sphere affects the solvation energies, and therefore the thermodynamic equilibrium governing the transition [23]. In the solid state, the implications of increased bond lengths are amplified by the close proximity of the complexes, giving rise to highly sought-after cooperative and hysteretic behaviors [24, 25]. Alterations in the

density and rigidity of the lattice also affect the refractive index of the material [26]. In a recent dedicated review, Bousseksou and co-workers [27] showed that the relative change in the refractive index of SCO materials, expressed as $(n_{HS} - n_{LS})/(1 - n_{LS})$, approximately matched the relative volume expansion $(V_{HS} - V_{LS})/V_{LS}$ accompanying the spin-transition, a trend reminiscent of the empirical law proposed by Gladstone and Dale in 1863 (Equation 3) [28].

$$\frac{n_{HS} - n_{LS}}{1 - n_{LS}} = \frac{V_{HS} - V_{LS}}{V_{LS}} \tag{3}$$

As the unit-cell volume typically increases by 1%–10% upon switching from the LS to the HS state [29–31], one predicts a concomitant decrease in the refractive index ranging from 0.01 to 0.1 [27]. It is worth noting here that the refractive index n only corresponds to the real part of the complex refractive index n^*, defined in Equation (4) as

$$n^* = n + ik \tag{4}$$

where i is the imaginary unit ($i^2 = -1$), and k is the imaginary part of n^*, known as the extinction coefficient [27]. The complex refractive index describes how a given medium affects the characteristics of an incident light beam as it propagates through it. From a microscopic perspective, n^* arises from the polarization of the molecules in response to the oscillating electric field (the magnetic interaction is much weaker and often neglected) of the electromagnetic wave [32]. More specifically, the real part n describes how the phase of the radiation is altered, while the imaginary part k quantifies the loss in amplitude caused by optical absorption. Interestingly, the aforementioned modulation of the refractive index n in SCO materials is not caused by a change in the electronic polarizability of the molecule, but is a consequence of the change in the number of electronic oscillators per unit volume in the material following the spin-transition [27]. This means that even though n and k are related through the Kramers–Kronig Equations 5 and 6 [33] (P denotes the Cauchy principal value of the integral, Ω is the angular frequency running through the whole integration range, and n_∞ is the high-frequency refractive index) [27], significant changes in n occur over broad spectral ranges independently of any variation in k. In other words, the SCO process offers the opportunity to modulate the phase of an electromagnetic wave without altering its amplitude [27].

$$n(\omega) = n_\infty + \frac{2}{\pi} P \int_0^\infty \frac{\Omega k(\Omega)}{\Omega^2 - \omega^2} d\Omega \tag{5}$$

$$k(\omega) = -\frac{2\omega}{\pi} P \int_0^\infty \frac{n(\Omega) - n_\infty}{\Omega^2 - \omega^2} d\Omega \tag{6}$$

Aside from inducing major structural changes, the new electronic distribution in the HS state also leads to an increase in the number of unpaired electrons, which naturally influences the paramagnetic susceptibility of the system. In this regard, the most remarkable evolution of the magnetic moment upon spin-state switching can be found in $3d^6$ metal complexes (Fe^{II}, Co^{III}), which transition from a fully diamagnetic $^1A_1$ state (no unpaired electron) to a highly paramagnetic $^5T_2$ state (four unpaired electrons). This reversible "on-off" switch of the magnetic properties in response to an external perturbation is the key feature that has driven application-oriented research in the SCO field over the last three decades. This coveted behavior is also one of the main reasons why Fe(II)-based SCO complexes, and more specifically pseudo-octahedral $[Fe^{II}N_6]$ systems where N is a heterocyclic nitrogen donor atom, are the most extensively studied [20].

Lastly, the abrupt change in the ligand-field splitting energy Δ_o upon the spin-transition and the subsequent shift in the energy levels of the t_{2g} and e_g^* orbitals drastically alter the electronic absorption spectrum of the complex. According to the Tanabe–Sugano diagram for a d^6 configuration (Figure 3), one indeed predicts two spin-allowed $^1T_1 \leftarrow {}^1A_1$ and $^1T_2 \leftarrow A_1$ d-d transitions in the LS state, whereas only one transition of this type ($^5E \leftarrow {}^5T_2$) is expected in the HS state [12]. However, due to their parity-forbidden character, these intrashell d-d transitions are weak and often masked by much more intense charge-transfer transitions in the visible range. Metal–ligand charge transfers (MLCT) are the most observed, as the aromaticity of most ligands makes them effective electron acceptors. Since these transitions involve molecular orbitals primarily located on the metal center, their energy is inherently dependent on the spin state of the complex [12]. Consequently, a thermally induced spin-transition is usually associated with a pronounced thermochromism characterized by a strong absorption in the visible range in the LS state (producing deeply colored complexes), and a much weaker absorption at higher frequencies in the HS state (giving pale yellow or colorless compounds) [20]. The significant disparity between the absorption spectra of the LS and HS species thus offers an opportunity to design bifunctional systems combining a SCO complex with a light-emitting entity, the emission spectrum of which can be tailored to overlap with only one of the two spin states, thereby enabling an optical readout of the magnetic status.

3 | Mechanistic Insights Into The Modulation of The Luminescence by the Spin-State Equilibrium

Understanding the mechanism underlying the interaction between the SCO unit and the luminescent moiety is critical for optimizing the design of current systems. For an intermolecular photophysical process to occur between these two entities, electronic energy must be transferred from the species capable of absorbing the excitation energy (i.e., the luminophore, more generally referred to as the sensitizer S) to the species capable of receiving this energy (i.e., the SCO unit, more generally referred to as the acceptor A). The nature of the interaction and the modalities governing the transfer vary with the nature of S and A and the properties of the material. In the case of luminescent SCO complexes, the modulation of the luminescence by the spin-state equilibrium can occur through one of the three following pathways.

3.1 | Radiative Energy Transfer

One of the simplest ways of transferring energy from an excited sensitizer S* to a ground-state acceptor A is through the emission and subsequent reabsorption of a photon. This so-called

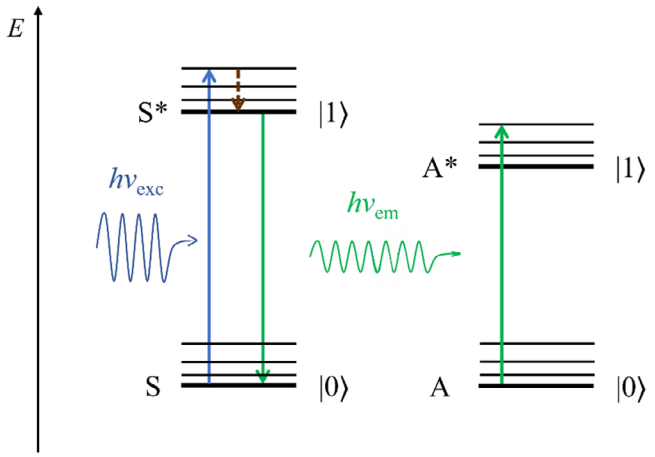

FIGURE 4 | Schematic representation of radiative energy transfer.

"emission-reabsorption" mechanism can be broken down into three steps that involve (i) the absorption of a photon of energy $h\nu_{em}$ by the ground-state sensitizer S, (ii) the radiative de-excitation of the excited sensitizer S* through the emission of another photon of energy $h\nu_{em} < h\nu_{exc}$, and (iii) the reabsorption of the photon of lower energy by the ground-state acceptor A (Figure 4). Once the acceptor has reabsorbed the emitted photon, it can return to the ground-state either through radiative or non-radiative processes. When the relaxation occurs through non-radiative processes, the luminescence of S* is effectively quenched [12].

A distinctive feature of the "emission-reabsorption" mechanism is that S and A do not interact directly but remain entirely independent of each other. As a result, the lifetime of S* is not affected by energy transfer, and the distance between the two entities does not influence the efficiency of reabsorption. The only important condition for this process to take place is that there should be a suitable spectral overlap between the emission of S* and the absorption of A. This being satisfied, the efficiency of the energy transfer will be a function of (i) the oscillator strength of the acceptor f_A, where f is a dimensionless parameter used to quantify the strength of a given transition (Equation 7) and (ii) the quantum yield of the sensitizer ϕ_{S^*}, where ϕ represents the ability of S* to decay radiatively and is defined as the ratio of the number of photons emitted to the number of photons absorbed (Equation 8, n is the refractive index, ε is the molar extinction coefficient, $\bar{\nu}$ is the frequency, and k_S^{rad} and $k_S^{non-rad}$ are the rate constants associated with radiative and non-radiative processes, respectively) [12].

$$f_A = \frac{4.32 \cdot 10^9}{n} \int \varepsilon(\bar{\nu})\, d\bar{\nu} \tag{7}$$

$$\phi_{S^*} = \frac{N_{photonsemitted}}{N_{photonsabsorbed}} = \frac{k_S^{rad}}{k_S^{rad} + \sum k_S^{non-rad}} \tag{8}$$

Moreover, since radiative energy transfer relies on a reabsorption event, the entire mechanism is under the influence of the Beer–Lambert law (Equation 9),

$$A = \varepsilon l c \tag{9}$$

where A is the total absorbance, c is the concentration of the acceptor, and l is the optical path length. Consequently, the concentration and spatial arrangement of the compounds should be considered carefully to ensure that A is on the path of the photons emitted by S* [12].

3.2 | Non-Radiative Energy Transfer

As the name suggests, non-radiative energy transfer refers to the process whereby electronic energy is transferred from the excited sensitizer S* to the ground-state acceptor A through non-radiative pathways, without photon emission or reabsorption. Unlike the previous mechanism, S* and A need to be electronically coupled, which only occurs when they are close enough to interact via the electric field or through chemical bonds. The probability $W_{S,A}$ that an interaction between S* and A will induce an energy transfer is given by Fermi's golden rule (Equation 10),

$$W_{S,A} = \frac{2\pi}{\hbar} |\langle SA^* | H | S^*A \rangle|^2 \Omega_{S,A} \tag{10}$$

where $\hbar$ is the reduced Planck constant, H is the perturbation Hamiltonian, and $\Omega_{D,A}$ is the spectral overlap integral [34]. As there are two potential interaction mechanisms that contribute to the perturbation Hamiltonian, H can be written as shown in Equation (11):

$$H = H_C + H_E \tag{11}$$

H_C represents the Coulombic interactions operating between the multipole changes associated with the S*→S and A*←A transitions, and H_E corresponds to the exchange interaction arising from the strong electronic coupling between S and A [35, 36].

The Coulombic mechanism was first studied by Theodor Förster in 1948 [37], and is now commonly referred to as "Fluorescent Resonance Energy Transfer" (or FRET) in the literature. In Förster's theory, the energy transfer occurs through the electrostatic interactions operating between the transition multipole moments associated with the simultaneous relaxation of S* and excitation of A [36]. It can thus be regarded as a two-electron process in which an excited-state multipole is transferred instead of an electron (Figure 5a) [38]. While the dipole-dipole interaction is usually considered to be the main component, higher-order multipolar contributions, such as dipole-quadrupole or quadrupole-quadrupole interactions, can sometimes play a role in the energy transfer when the former is weak or inoperative [35]. This mechanism is sometimes termed "through-space" as the interaction goes through the electric field and does not require a physical contact between S and A. However, its efficiency decreases as d^{-n}, where d represents the distance between S and A, and n corresponds to the order of the multipole involved in the interaction ($n = 6, 8, 10$) [36]. Furthermore, a significant spectral overlap between the emission of S* and the absorption of A is required, which limits this process to spin-allowed transitions, as the transition dipole moments associated with spin-forbidden ones are too small to promote an energy transfer [35].

The exchange mechanism, theoretically modeled by David Dexter in 1953 [39], involves a double electron exchange whereby one

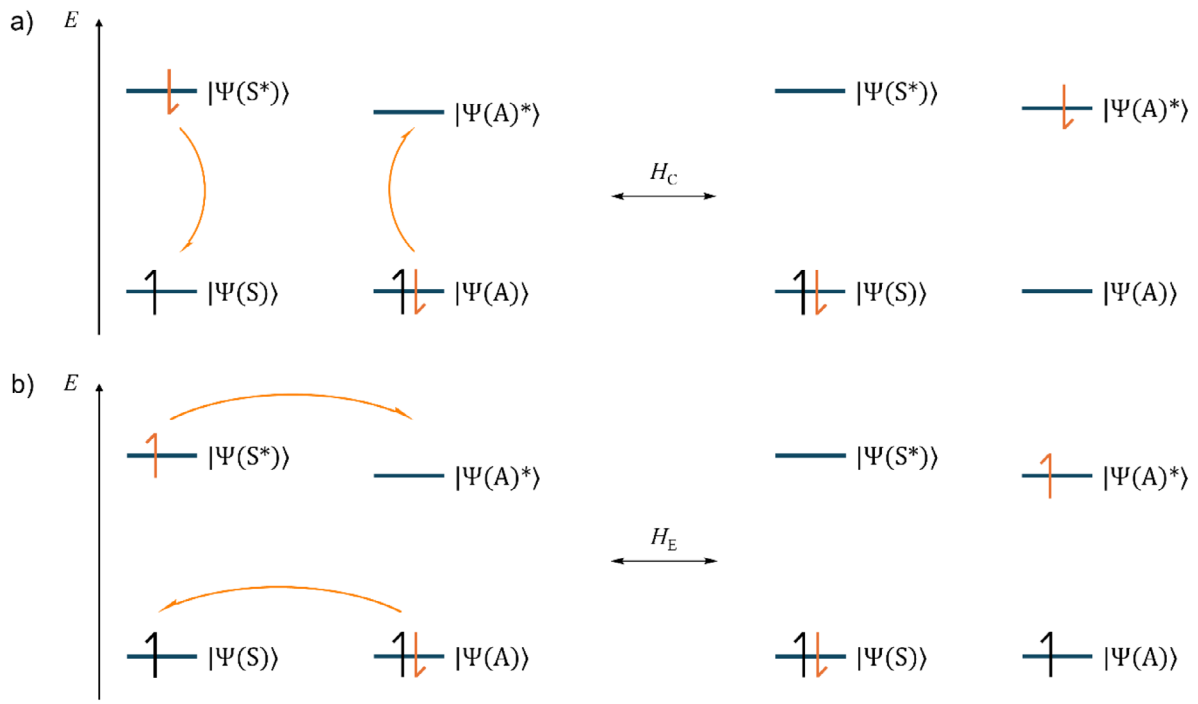

FIGURE 5 | Schematic representation of (a) Förster and (b) Dexter non-radiative energy transfers, highlighting their respective spin selection rules.

electron is transferred in each direction from S* and A to A* and S, respectively (Figure 5b) [35]. This process requires a strong electronic coupling between S and A, which can only be achieved through a double orbital overlap [38]. This has two important consequences: (i) since the probability density functions of electrons decay exponentially with increasing distance from the nucleus, Dexter energy transfer is only effective over short distances, with its efficiency decreasing as e^{-2d}, and (ii) because the exchange integral does not have strict selection rule at each center, spin-forbidden conversions, such as the relaxation of a triplet excited state of S* to a singlet ground state and the excitation of a singlet ground state of A to a triplet excited state, are permitted, provided that the total spin of the assembly is conserved [35, 39].

Despite their differences, both the Coulombic and the exchange mechanism represent additional relaxation pathways for the excited state of S*, complementing the radiative and other non-radiative processes without altering them [12]. Therefore, when non-radiative energy transfer occurs, the lifetime of the excited sensitizer τ_S can be expressed as shown in Equation (12):

$$\tau_S = \left(k_S^{rad} + k_S^{non-rad} + k_{EnT}\right)^{-1} \quad (12)$$

where k_{EnT} is the energy transfer rate constant. Depending on the nature of the interaction between S and A, k_{EnT} may take the form of either $k_{EnT}^{F\cong rster}$ (Equation 13) or k_{EnT}^{Dexter} (Equation 14).

$$k_{EnT}^{F\cong rster} = \frac{8.8 \cdot 10^{-25} \kappa^2 \phi_{S^*}}{n^4 \tau_{S^*} d^6} J_F \quad (13)$$

$$k_{EnT}^{Dexter} = \frac{4\pi^2 H^2}{h} J_D \quad (14)$$

where κ is the orientation factor (usually taken as 2/3 in randomly organized systems), n is the refractive index of the solvent, τs is the lifetime of the sensitizer in the absence of energy transfer, H is the electronic coupling, h is the Planck constant, and $J_F = \frac{\int S(\bar{\upsilon})A(\bar{\upsilon})/\bar{\upsilon}^4 d\bar{\upsilon}}{\int S(\bar{\upsilon})d\bar{\upsilon}}$ and $J_D = \frac{\int S(\bar{\upsilon})A(\bar{\upsilon})d\bar{\upsilon}}{\int S(\bar{\upsilon})d\bar{\upsilon} \int A(\bar{\upsilon})d\bar{\upsilon}}$ are the overlap integrals [35].

The distinct distance dependencies of $k_{EnT}^{F\cong rster}$ and k_{EnT}^{Dexter} represent the most straightforward way of diagnosing the nature of the interaction mechanism operating in SCO-luminescent systems. As discussed above, the strong electronic coupling required to achieve the double electron transfer in Dexter mechanism, expressed by H^2 in Equation 14, arises from direct orbital overlap between S and A. Since H^2 falls off as $e^{-2d/L}$, where L is a constant known as the effective average Bohr radius [40], k_{EnT}^{Dexter} decays sharply with distance, thereby limiting Dexter energy transfer to distances no greater than a few Ångstroms [35]. However, when S and A are embedded within a conjugated framework, the orbitals of intermediate bridging ligands may contribute to mediate the double electron-transfer over larger distances through a so-called superexchange mechanism [41]. In contrast, $k_{EnT}^{F\cong rster}$ "only" diminishes as d^{-6} (Equation 13), meaning that Förster-type electrostatic dipole-dipole interactions may be expected to operate over distances up to 100 Å [35]. Consequently, the majority of non-radiative energy-transfer processes operating in luminescent SCO materials follow a Förster mechanism, with Dexter-type contributions being generally limited to systems in which donor and acceptor units are incorporated into an extended π system.

3.3 | Environmental Effects

The considerable mechanical strains exerted on the lattice by the expansion (or the contraction) of the coordination sphere of the SCO unit during the spin transition heavily influence the properties and dynamics of the environment surrounding the excited

sensitizer S* [14]. As a result, local variations in polarity, rigidity, or vibrational frequencies following the transition can affect the luminescence intensity, shorten the lifetime of S* by promoting non-radiative processes, or induce spectral shifts. However, unlike emission-reabsorption and energy transfer mechanisms, which are readily identifiable, these effects remain difficult to predict and interpret. In most cases, their primary diagnostic feature is the weak correlation between the modulation of the luminescence and the spectral overlap. Nevertheless, there is no doubt that these environmental factors play a crucial role in shaping the luminescence response of most luminescent SCO materials [11].

4 | Spin-Crossover Modulated Luminescence in Materials

A widely explored strategy to design luminescent SCO materials consists of physically doping preexisting SCO frameworks with suitable luminophores. A significant advantage of this approach is that the low dopant concentrations in the host matrix minimize the risk of it adversely interfering with the SCO process, thereby improving the likelihood of preserving both magnetic and luminescent functionalities [12]. The straightforward preparation of these hybrid materials also eliminates the need for elaborate ligand design, which is attractive from a synthetic standpoint [11]. Moreover, as the SCO-active and luminescent components remain chemically independent, their properties can be individually optimized with minimal risk of disrupting the rest of the material [12]. However, this strategy suffers from several limitations. The structural relationship between the SCO center and the fluorophore is usually not well defined, which makes the elucidation of the interaction mechanism rather complex. In addition, the low stoichiometric ratio of luminophore to SCO units, combined with the difficulty of achieving a homogeneous distribution and reproducibility, may restrict the sensitivity of the probe to a localized region of the material, which may in turn not accurately reflect the behavior of the entire system. As such, this strategy appears better suited for practical applications than for mechanistic investigations [11, 12].

The following sections examine recent advances in three main classes of nanomaterials that integrate both SCO and luminescent properties.

4.1 | Thin Films

Matsuda and co-workers [42] fabricated a thin film of the SCO complex $[Fe(\mathbf{1})_2](BF_4)_2$ using the so-called spin-coating method, with a spin-transition measured around 260 K (Figure 6a). Interestingly, the temperature-dependence of the electrical resistance of the film decreased by 25% upon cooling from 260 to 240 K, coinciding with the temperature range over which the magnetic susceptibility dropped. Based on these results, the authors reckoned that the $[Fe(\mathbf{1})_2](BF_4)_2$ film could be used to control the electronic properties of organic thin films, which led them to develop a new organic light-emitting diode (OLED), in which the SCO complex was embedded into the light-emitting layer of a chlorophyll *a*-based OLED (Figure 6b) [43, 44].

Satisfyingly, variable-temperature electroluminescent spectra of the ITO/chlorophyll *a*:$[Fe(\mathbf{1})_2](BF4)_2$/Al device ($V$ = 3.5 V) showed the well-known luminescence of chlorophyll *a* (Chl *a*) at 689 nm, which suddenly disappeared below 260 K (Figure 6c). Repeating the measurements over several thermal cycles proved the reversibility and the reproducibility of the on/off switching process. Interestingly, concomitant photoluminescence measurements acquired at 200 and 300 K both displayed the emission of Chl *a*, indicating that the quenching of the electroluminescence by the LS-$[Fe(\mathbf{1})_2](BF_4)_2$ complex was not the result of an energy transfer (Figure 6d) [43, 44]. Further investigations eventually concluded that the modulation was caused by a drastic change in the carrier injection efficiency upon HS→LS spin transition, which prevented the formation of excited Chl *a* [45]. Inspired by their recent success in developing luminescent SCO nanoparticles in solution (see Section 4.2) [46, 47], Bousseksou and co-workers [48, 49] investigated the fluorescent detection of the polymeric SCO $[Fe(\mathbf{2})_3](OTs)_2$ complex doped with acridine orange both in spin-coated thin films and in single SCO nanomaterials patterned via soft lithography (Figure 7). The chromophore was selected for its robustness and for the substantial spectral overlap between its emission and the $^1A_1 \rightarrow {}^1T_1$ d-d absorption band of the LS-$[Fe(\mathbf{2})_3](OTs)_2$ complex (Figure 7a). In the thin films, the temperature-dependence of the luminescence intensity at 550 nm (λ_{exc} = 450 nm) showed abrupt variations synchronized with the increase/decrease in intensity of the $^1A_1 \rightarrow {}^1T_1$ absorption band upon the spin-transition. Repeated thermal cycling confirmed the reproducibility of the luminescence switching and the absence of photobleaching despite the continuous excitation (Figure 7b). A control experiment performed under similar conditions but with a glass barrier physically separating the SCO complex and the luminophore displayed no observable modulation of the acridine emission, thereby demonstrating the non-radiative nature of the energy transfer. The nanodot arrays fabricated via soft lithography exhibited the same thermally induced luminescence modulation for individual dots, without ensemble averaging. Remarkably, the SCO behavior of each nanodot could be correlated with its individual geometrical features, as determined by SEM [48, 49]. In light of these promising results, Bousseksou and co-workers [26] explored two potential applications of their luminescent SCO nano-films for thermometry and thermal imaging: (i) a spin-coated thin film of $[Fe(\mathbf{2})_3](OTs)_2$ doped with rhodamine 110 was deposited on a passivated gold microwire, where localized resistive heating triggered a spin-transition, leading to a luminescence increase that could be correlated with the local temperature, and (ii) nanodots of the $[Fe(\mathbf{2})_3](OTs)_2$ complex doped with acridine orange exhibited enhanced luminescence upon adsorption of ethanol vapor, opening new perspectives for real-time gas monitoring.

A few years later, Bousseksou and co-workers [11] introduced a new strategy for modulating luminescence by spin-state equilibria based on a "spatially controlled assembly" approach, in which the SCO complex and the luminophores are juxtaposed in a controlled manner. They designed a bilayer thin film consisting of a layer of the $[Ir(\mathbf{3})_3]$ luminophore, which exhibits a characteristic green emission band centered at 515 nm upon UV irradiation, covered by a layer of the SCO $[Fe(\mathbf{4})_2]$ complex, which undergoes a full and abrupt spin-transition around 337 K and strongly absorbs UV light in the LS state (MLCT band

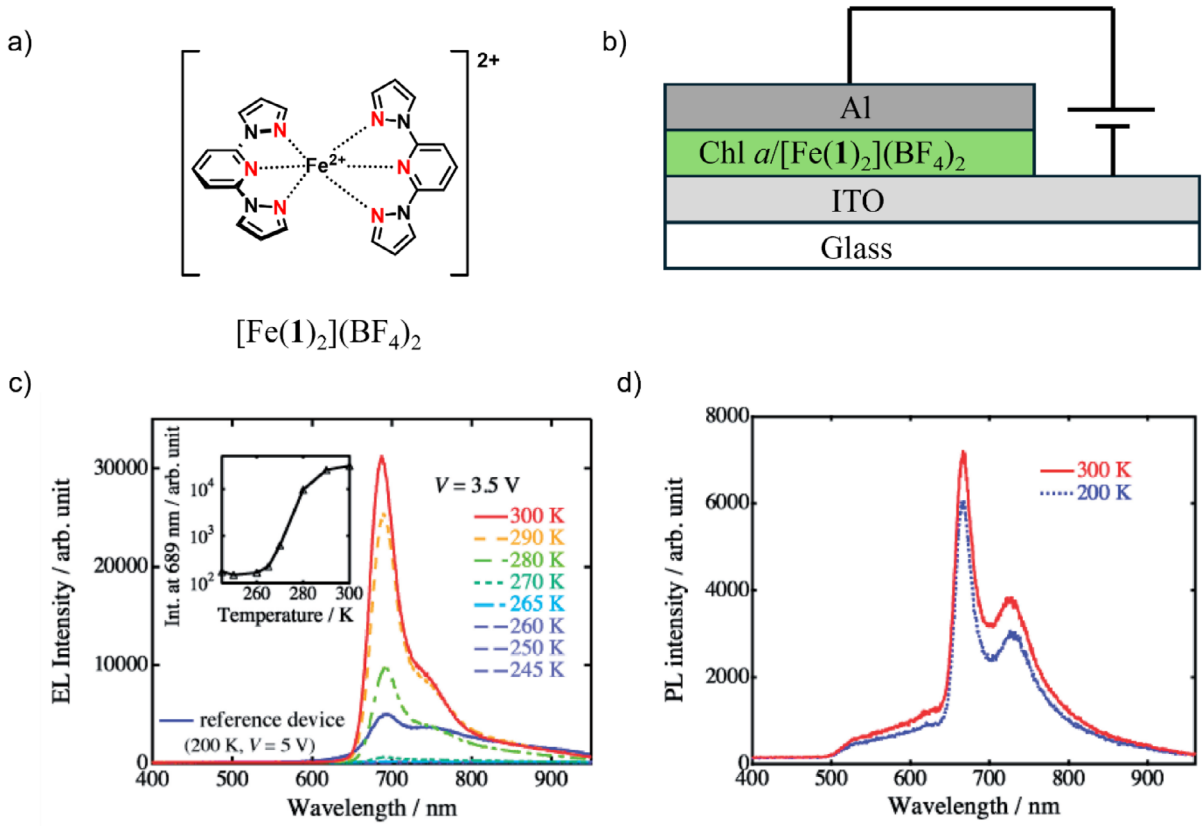

FIGURE 6 | (a) Chemical structure of $[Fe(\mathbf{1})_2](BF_4)_2$, (b) schematic representation of the OLED device, (c) electroluminescence spectra ($V = 3.5$ V) of the OLED device recorded at different temperatures, and (d) photoluminescence spectra ($\lambda_{exc} = 435$ nm) of the Chl *a*:$[Fe(\mathbf{1})_2](BF4)_2$ layer at 300 K (red trace) and 200 K (blue trace). Reprinted from ref [44] with permission of Oxford University Press and the Chemical Society of Japan through Copyright Clearance Center, Inc.

with $\varepsilon_{318\,nm} = 3{\cdot}10^4$ $M^{-1}cm^{-1}$) whereas the HS state is quasi-transparent (Figure 8). Upon heating, the optical density of the bilayer decreased dramatically ($\Delta_{abs} = 0.39$ at 318 nm) around 337 K, resulting in an abrupt luminescence enhancement between 333 and 350 K, while the emission lifetime remained unaffected. These measurements were reproducible over several heating-cooling cycles, despite a small continuous decrease in luminescence intensity attributed to photobleaching. Remarkably, the twofold increase in luminescence intensity was consistent with the twofold increase in transmittance. This scalability was further investigated in bilayers of increasing thickness, yielding a linear correlation between the luminescence modulation (I_{HS}/I_{LS}) and the change in transmittance in the SCO layer. Therefore, the luminescence intensity could be modulated "at will" by adjusting the thickness of the SCO layer [11].

Galán-Mascarós and co-workers [50] reported the fabrication of solution-processed thin films composed of various ratios of the fluorescent organic semiconductor polyfluorene (PFO), and the Fe(II)-based SCO 1D coordination polymer $[Fe(\mathbf{5})]_n{\bullet}n$X (X = Cl^-, TsO^-, Figure 9). Magnetic susceptibility measurements confirmed the SCO behavior, with $T_{1/2} = 344(2)$ K upon heating and $T_{1/2} = 326(2)$ K upon cooling, irrespective of the $[Fe(\mathbf{5})]_n{\bullet}n$X:PFO ratio. Variable-temperature fluorescence spectra of the $[Fe(\mathbf{5})]_n{\bullet}n$Cl:PFO blends showed a pronounced increase in the fluorescence intensity upon heating, accompanied by a small blue-shift and a broadening of the emission band. Reversibility was only observed when the cooling rate was sufficiently slow, or after holding the sample 1 h at RT.

In contrast, the $[Fe(\mathbf{5})]_n{\bullet}n$OTs:PFO blends exhibited an initial decrease in fluorescence intensity up to the transition temperature, followed by a modest increase, without any significant spectral shift or band broadening. Given that both a reference PFO film and an analogous $[Zn(\mathbf{5})]_n{\bullet}n$OTs:PFO blend exhibited the expected thermal quenching of fluorescence upon heating, the modulation of the emission in the Fe(II)-based systems was ascribed to the SCO process. The interplay between the spin-transition and the luminescence was further supported by the larger emission intensity differences observed in blends with higher $[Fe(\mathbf{5})]_n{\bullet}n$Cl contents. Considering (i) the strong influence of the counter anions on the intensity change, and (ii) the negligible absorption of the SCO complex relative to PFO in the composite films, the authors attributed the fluorescence switching to environmental lattice changes caused by the spin-transition [50].

4.2 | Nanoparticles

Over the years, Bousseksou and co-workers [12, 27] have contributed immensely to the development of luminescent SCO nanoparticles, reporting numerous systems that explored a variety of design strategies (Figure 10).

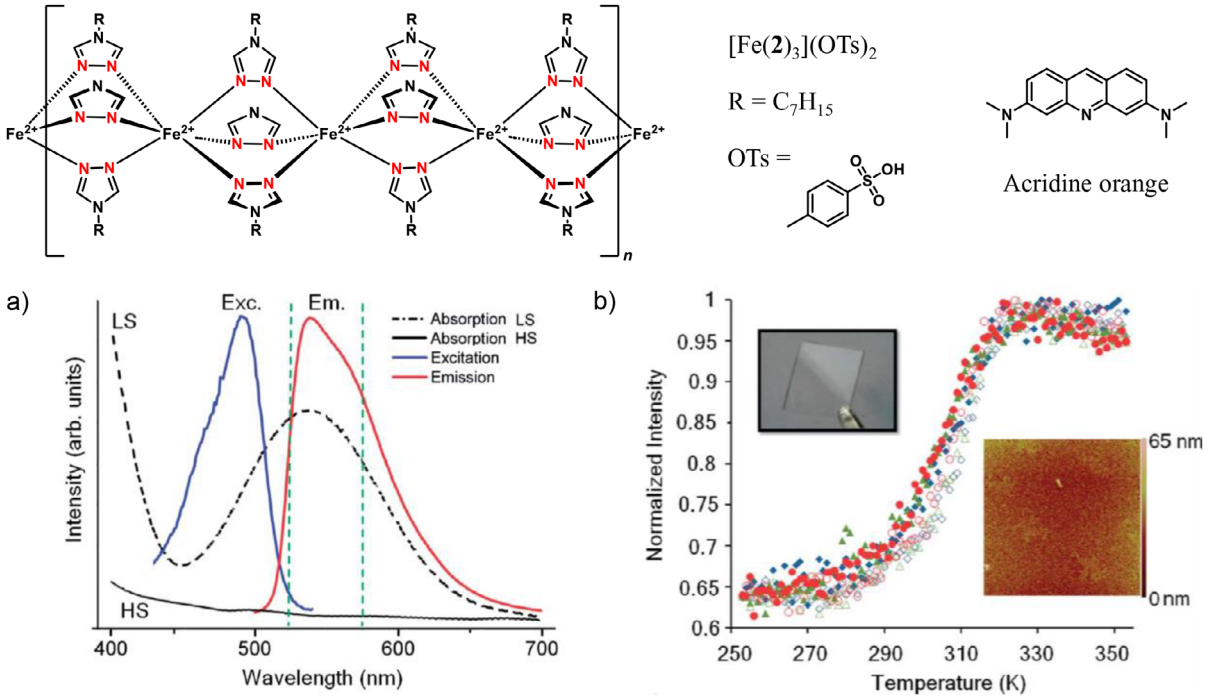

FIGURE 7 | Top panel: chemical structures of the $[Fe(\mathbf{2})_3](OTs)_2$ complex, the tosylate counter anion and the acridine orange chromophore; bottom panel: (a) comparison of the solid state normalized excitation (blue trace) and emission (red trace) spectra of $[Fe(\mathbf{2})_3](OTs)_2$ doped with acridine orange at R*T* with the absorption spectra of an undoped chloroform solution of $[Fe(\mathbf{2})_3](OTs)_2$ in the LS state (dashed black trace, R*T*) and in the HS state (solid black line, 320 K), and (b) temperature-dependence of the normalized luminescence intensity at 550 nm (450 nm) in the spin-coated thin film of $[Fe(\mathbf{2})_3](OTs)_2$ doped with acridine orange during three consecutive thermal cycles. Reprinted from ref [48] with permission from the Royal Society of Chemistry.

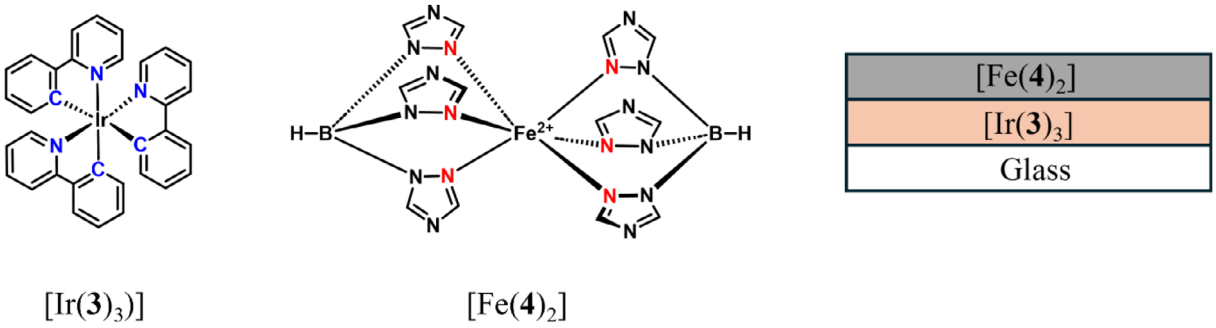

FIGURE 8 | Chemical structures of the $[Ir(\mathbf{3})_3]$ and $[Fe(\mathbf{4})_3]$ complexes and schematic representation of the bilayer stack.

In 2010, they prepared monodisperse nanoparticles of the SCO $[Fe(\mathbf{6a})_3](X)_2$ (X = OTs^-, NO_3^-) complex doped with either rhodamine-110 or alizarine-red (Figure 10) [46, 47]. Rhodamine-110 was selected based on (i) the large spectral overlap between its emission at 540 nm and the $^1A_1 \rightarrow {}^1T_1$ absorption of LS-$[Fe(\mathbf{6a})_3]^{2+}$ complex (Figure 11a), (ii) the negligible thermal quenching of its emission at R*T*, and (iii) its excellent photostability. Alizarine-red, on the other hand, was primarily chosen for its negative charge, as it could promote closer association with the positively charged SCO units, potentially enhancing energy-transfer efficiency. Temperature-dependent fluorescence measurements (λ_{exc} = 475 nm) revealed a 50% increase in the luminescence intensity of rhodamine-110 upon heating (Figure 11b), which was consistent with the absorbance changes observed at the excitation ($\Delta A_{540\,nm}$ = 0.25) and emission (ΔA_{475nm} = 0.1) wavelengths during the spin-transition. For the alizarine-red system, a three-fold increase in the emission intensity was observed upon thermal spin-transition, which was rationalized by the improved efficiency of the non-radiative energy transfer enabled by the reduced spatial separation between the anionic chromophore and the SCO centers [46, 47].

In 2014, they functionalized cellulose sheets with $[Fe(\mathbf{6b})_3](OT)_2$ nanoparticles and acridine orange chromophores with the aim of developing a luminescent platform for potential anti-counterfeiting applications (Figure 10) [51]. The adsorption of the nanoparticles onto the linter fibers was driven by favorable electrostatic interactions between the electron-rich hydroxyl groups of cellulose and the electropositive Fe(II) centers. The resulting biopolymer/SCO nanocomposites exhibited a pronounced ther-

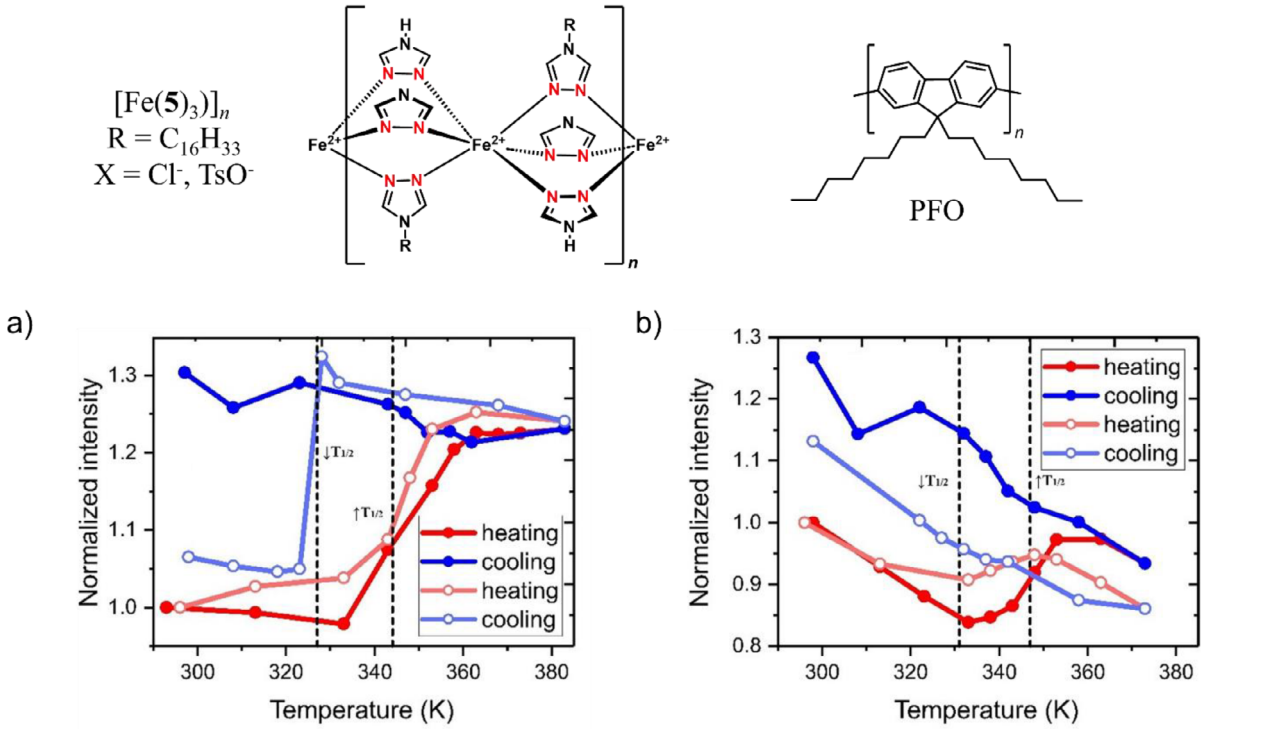

FIGURE 9 | Chemical structures of the $[Fe(\mathbf{5})]_n \bullet nX$ and PFO polymers (top panel), and temperature-dependent evolution of the maximum fluorescence intensity of (a) the $[Fe(\mathbf{5})]_n \bullet n$Cl and (b) the $[Fe(\mathbf{5})]_n \bullet n$OTs blends with 80:20 SCO:PFO ratios. Reprinted with permission from ref [50]. Copyright 2021 American Chemical Society.

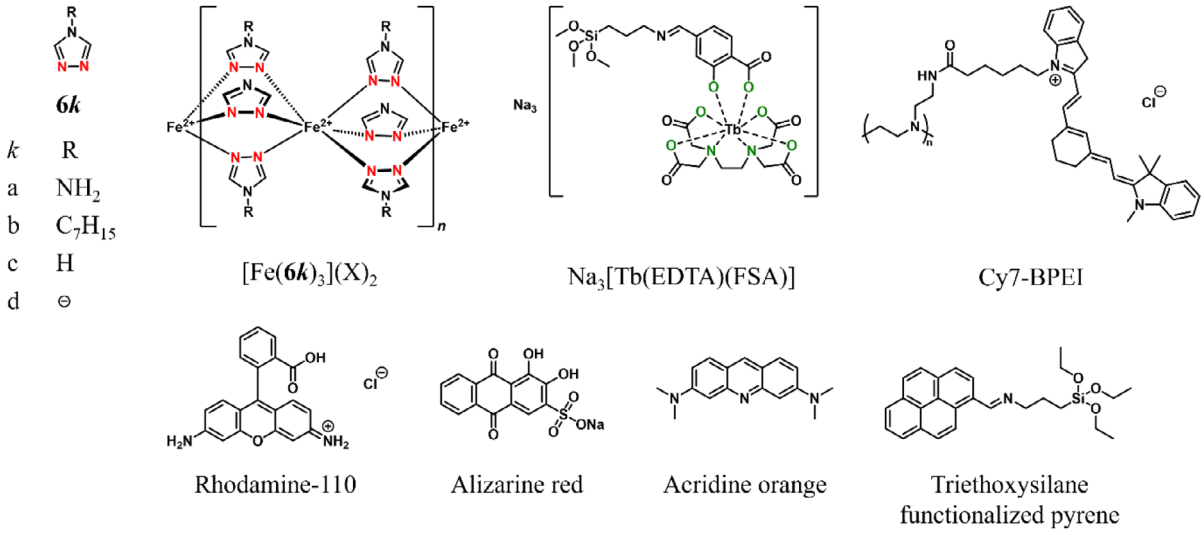

FIGURE 10 | Chemical structures of the 1,2,4-triazole ligands **6*k*** with the donor atoms highlighted and of various chromophores.

mochromic behavior, characterized by abrupt changes in the diffuse reflectance spectra around 327 K upon heating and around 324 K upon cooling, closely matching the thermal hysteresis of the spin-transition. Variable-temperature fluorescence spectra showed corresponding variations in the emission intensity at 543 nm around 319 K (heating) and 313 K (cooling), with a 27% luminescence enhancement in the HS state attributed to the bleaching of the $^1A_1 \rightarrow {}^1T_1$ absorption band upon the spin-transition. Although prolonged exposure to light led to some photobleaching of acridine orange, the authors proposed to address this issue by substituting it with the more photostable rhodamine-110 [51].

The following year, they investigated the temperature-dependent excimer luminescence of pyrene-grafted $[Fe(\mathbf{6c})_2(\mathbf{6d})](BF_4)$ based SCO@SiO_2 nanoparticles with various fluorophore contents (37%, 11%, 4.2%, and 1.7% mass, Figure 12) [52]. Since the characteristic excimer emission at lower energy arises when ground- and excited-state pyrene moieties are in close proximity, the excimer-to-monomer fluorescence intensity ratio serves as

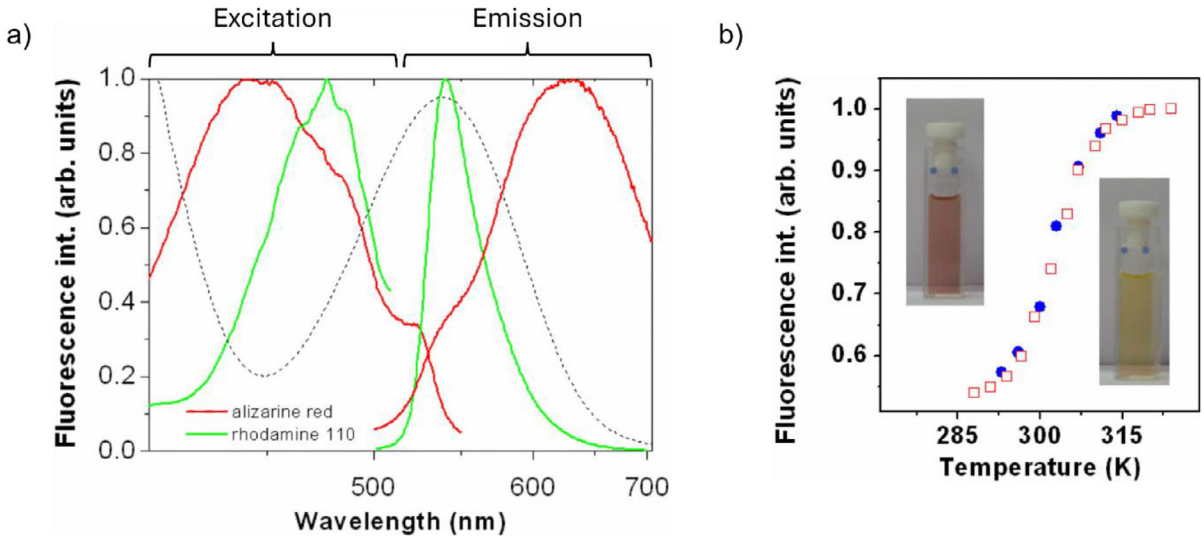

FIGURE 11 | (a) Comparison of the excitation and emission spectra of rhodamine-110 (green traces) and alizarine-red (red traces) doped $[Fe(\mathbf{6a})_3](OTs)_2$ nanoparticle suspensions with the $^1A_1 \rightarrow {}^1T_1$ absorption band of LS-$[Fe(\mathbf{6a})_3]^{2+}$ complex (doted black trace), and (b) temperature-dependent emission intensity at 540 nm of a of 0.01% rhodamine-110 doped $[Fe(\mathbf{6a})_3](OTs)_2$ suspension. Adapted from ref [47].

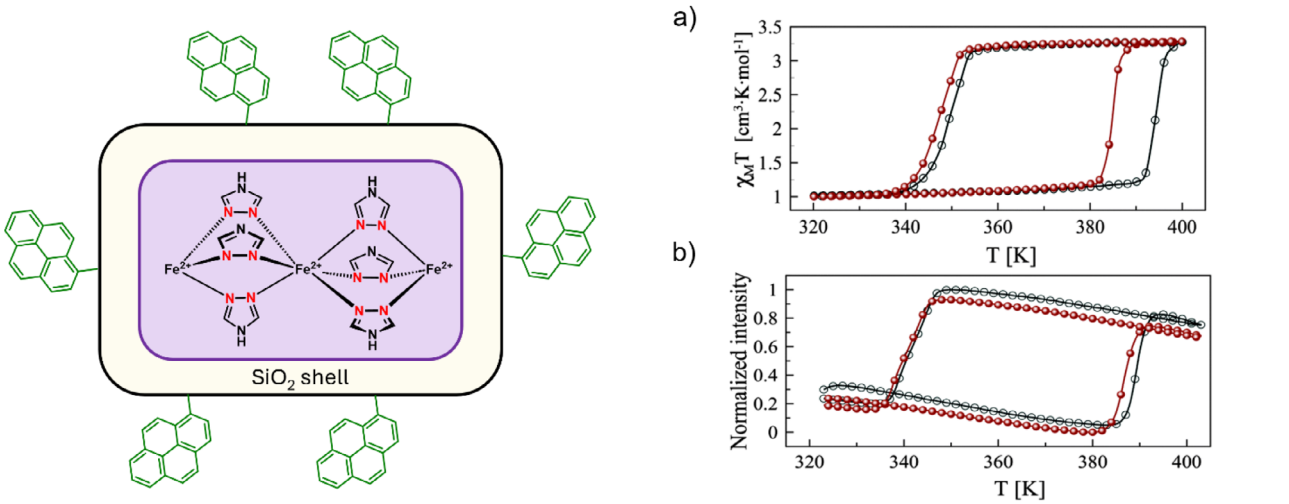

FIGURE 12 | Left panel: schematic representation of the pyrene-grafted $[Fe(\mathbf{6c})_2(\mathbf{6d})](BF_4)$ SCO@SiO_2 nanoparticles; right panel: temperature-dependence of (a) the $\chi_M T$ product and (b) the normalized luminescence intensity at 550 nm of the pyrene excimer over two thermal cycles. Reproduced from ref [52] with permission from the Royal Society of Chemistry.

a sensitive probe of their spatial arrangement and orientation. Given that the spin-transition is accompanied by a substantial volume change, this ratio may thus provide an effective optical readout of the spin-state equilibrium. The thermal evolution of the normalized excimer fluorescence intensity at 550 nm was in good agreement with that of the magnetic susceptibility, displaying a similar hysteresis loop with abrupt changes at 345 and 380 K upon heating and cooling, respectively (Figure 12b). While the initial decrease of the excimer luminescence lifetime upon heating was consistent with the promotion of non-radiative relaxation channels, longer lifetimes were observed upon the transition from the LS to the HS state. Considering the significant overlap between the $^1A_1 \rightarrow {}^1T_1$ absorption at 530 nm and the excimer emission, this observation could be diagnostic of a non-radiative energy transfer occurring in the LS state. However, the large separation between the donor and the acceptor and the low extinction coefficient associated with the transition challenged this hypothesis. Further investigation revealed that (i) the monomer emission was virtually unaffected by the SCO process despite having some overlap with the $^1A_1 \rightarrow {}^1T_1$ absorption, and (ii) the excimer emission was red-shifted in the HS state, definitely ruling out a FRET mechanism. With these considerations in mind, the authors suggested that the volume expansion associated with the spin-transition interfered with the pyrene-pyrene dimer formation, leading to the observed modulation of the excimer luminescent properties [52].

In another 2015 contribution, Bousseksou and co-workers [53] addressed the photobleaching issue commonly associated with organic dyes by grafting a $Na_3[Tb(EDTA)(FSA)]$ complex bearing trimethoxysilane groups onto their $[Fe(\mathbf{6c})_2(\mathbf{6d})](BF_4)$@$SiO_2$ SCO nanoparticles (Figure 10). The resulting Tb-SCO nanocom-

posite consisted of long, aggregated nanoparticles (nanorods) with 14% Tb(III) content relative to Fe(II). The emission spectrum featured four characteristic Tb(III) $^5D_4 \rightarrow {}^7F_J$ (J = 6–3) transitions at 489, 545, 585, and 620 nm, respectively, with the most intense transition ($^5D_4 \rightarrow {}^7F_5$) lying close to the absorption maximum of the LS $^1A_1 \rightarrow {}^1T_1$ band at 530 nm. As expected, the temperature-dependence of the Tb(III)-based luminescence closely mirrored that of the magnetic susceptibility, exhibiting drastic variations around $T_{1/2}$ = 395 K upon heating, and near $T_{1/2}$ = 361 K upon cooling. Notably, the emission intensity at 550 nm (λ_{exc} = 450 nm) showed a mere 1.4% decrease over five heating-cooling cycles, in stark contrast with the losses of several tens of percent typically observed with organic dyes, thereby confirming the exceptional photostability of the system. Temperature-dependent luminescence lifetime measurements yielded similar values in both spin-states (0.662 ms in the LS state and 0.668 ms in the HS state), suggesting that the underlying interaction mechanism involved a radiative emission-reabsorption process [53].

In 2016, the favorable spectral overlap between the CdTe quantum dot emission around 555 nm and the LS $^1A_1 \rightarrow {}^1T_1$ absorption band inspired Bousseksou and co-workers [54] to synthesize [Fe(**6c**)$_2$(**6d**)](BF$_4$) nanoparticles coated with either SiO_2 or branched polyethylenimine (BPEI) and decorated with fluorescent CdTe nanocrystals (1%–2% CdTe/Fe). While both nanocomposites exhibited a reversible modulation of their luminescence intensity upon the spin-transition, the magnitude of the variation was incredibly small, merely amounting to 0.03% in the SiO_2-coated material and to 5% in the BPEI-coated sample. In addition, an irreversible decrease in luminescence intensity was observed between each heating/cooling cycle, indicative of photobleaching. Variable-temperature luminescence lifetime measurements further revealed an incomplete recovery of the fluorescence lifetime after each thermal cycle, suggesting some photothermal degradation of the nanocrystal surface [54].

In 2017, the same group [14] combined their SCO nanoparticles with a near-infrared (NIR)-emitting cyanine dye, with the aim of creating a "reverse material" in which the luminescence would decrease in the HS state. In the pursuit of this design, the Cy7-NHS polymethine cyanine dye was grafted onto the amine groups of BPEI, then combined with [Fe(**6c**)$_2$(**6d**)](BF$_4$) nanoparticles to give the SCO-Cy7-BPEI nanocomposites (Figure 10). The solid emission spectrum of a reference Cy7-BPEI nanoparticle confirmed the spectral overlap between the broad emission of the cyanine at 752 nm (λ_{exc} = 700 nm) and the weak HS $^5T \rightarrow {}^5E$ d-d absorption of the [Fe(**6c**)$_2$(**6d**)](BF$_4$) complex centered around 800 nm (Figure 13a). Unexpectedly, an abrupt and reversible 350%–400% increase in luminescence intensity was observed upon the LS to HS transition, as opposed to the anticipated quenching effect from the enhanced HS $^5T \rightarrow {}^5E$ absorption (Figure 13b). The authors rationalized that the modulation of the luminescence intensity in the composite was related to changes in the properties of the crystal lattice rather than in the spectral overlap. Peculiarly, an irreversible intensity drop was observed in the 385–400 K range after the complex had switched to the HS state (Figure 13b). A plausible explanation for this phenomenon, previously proposed by Colacio and co-workers [55], involved an enhanced photobleaching of the luminophore in the HS state at elevated temperatures, although some irreversible structural changes in the SCO complex could also result in the promotion of non-radiative relaxation processes of the excited fluorophores. Another intriguing feature was that the transition temperatures extracted from the luminescence data were upshifted compared to those measured via SQUID magnetometry. This discrepancy could be explained by considering that the luminescence measurements primarily probed the sample surface, which may have different SCO properties than the bulk [14].

Following the pioneering work of Bousseksou and co-workers [56], Herrera and Colacio proposed an alternative strategy based on the use of silica nanoparticles (SiO_2NPs) as a matrix for the SCO system. Silica matrices (i) display high porosity compatible with the incorporation of SCO complexes, (ii) do not interfere with electromagnetic fields, and (iii) offer a surface that can be functionalized with active species such as fluorophores, making them ideally suited for the design of multifunctional SCO nanoparticles. Therefore, using [Fe(**6c**)$_2$(**6d**)](BF$_4$) as the SCO component, and 3-(dansylamido)propyltrimethoxysilane (dansyl) as the fluorophore, hybrid SiO_2NPs ⊃ Fe-Trz nanocomposites were prepared using the reverse micelle technique. Hybrid SiO_2NPs ⊃ Fe/Zn-Trz nanoparticles based on [Fe$_{1-x}$Zn$_x$(**6c**)$_2$(**6d**)](BF$_4$) complexes were also synthesized to test the effect of Zn(II) doping on the magnetic properties of the system. Magnetic measurements confirmed the preservation of the SCO process, with slight variations in the expected abrupt spin-transition and large thermal hysteresis attributed to the presence of Zn(II) dopants. The diffuse reflectance spectra recorded at 280 K displayed the two characteristic $^1A_{1g} \rightarrow {}^1T_{1g}$ and $^1A_{1g} \rightarrow {}^1T_{2g}$ d-d transitions at 538 and 382 nm, respectively, which completely disappeared at 400 K, resulting in a pronounced thermochromism (pink/violet to white). Remarkably, the thermal variation of the fluorescence intensity at 494 nm of the Zn(II)-doped nanoparticles in the 283–373 K range closely mirrored the thermal dependence of the $\chi_M T$ product, suggesting that the large increase in the fluorescence intensity was correlated to the SCO process. This enhancement was ascribed to the reduction of the quenching by the LS-Fe(II) $^1A_{1g} \rightarrow {}^1T_{1g}$ absorption at 538 nm upon heating [56]. In a subsequent study, Herrera and Colacio [55] reported the synthesis of bare and silica-wrapped [Fe(**6c**)$_2$(**6d**)](BF$_4$) nanoparticles, the size and shape of which could be precisely controlled by the concentrations of Fe(II) and **6c**. Compared to their uncoated counterparts, the core-shell Fe**6c**@SiO_2 nanoparticles enhanced cooperative interactions, providing wider hysteresis loops. Grafting a dansyl derivative onto the particle surface led to a broad emission band at 494 nm (λ_{exc} = 315 nm). Variable-temperature measurements revealed a fourfold increase in luminescence intensity upon heating. To confirm the synergy between the SCO and the luminescence, the emission intensity was measured over two thermal cycles. A clear hysteresis loop closely matching the one derived from the magnetic measurements was observed, with a sharp decrease at 336 K upon cooling, and a sharp increase at 395 K upon heating (Figure 14a). The small decrease in the emitted intensity between cycles was attributed to the thermal decomposition of the fluorophore at 400 K (Figure 14b). To determine whether the quenching process occurred through radiative or non-radiative pathways, the emission lifetime of the chromophore was measured in (i) the hybrid Fe**6c**@SiO_2 nanoparticles and in (ii) an analogous Ludox AS-40 SiO2 nanoparticle lacking SCO quenchers. The reduction in the emission lifetime from 12.0 to 7.4 ns pointed toward a non-radiative Förster-type energy transfer between the dansyl groups

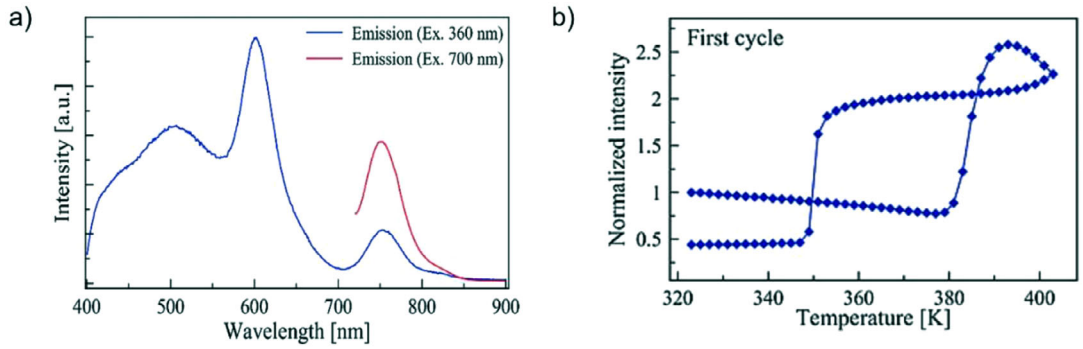

FIGURE 13 | (a) Solid-state emission spectra of the reference Cy7-BPEI@SiO_2 nanoparticles, and (b) thermal evolution of the normalized luminescence intensity of the SCO-Cy7-BPEI nanocomposite at 780 nm (λ_{exc} = 700 nm). Adapted with permission from ref [14]. Copyright 2017 Wiley-VCH.

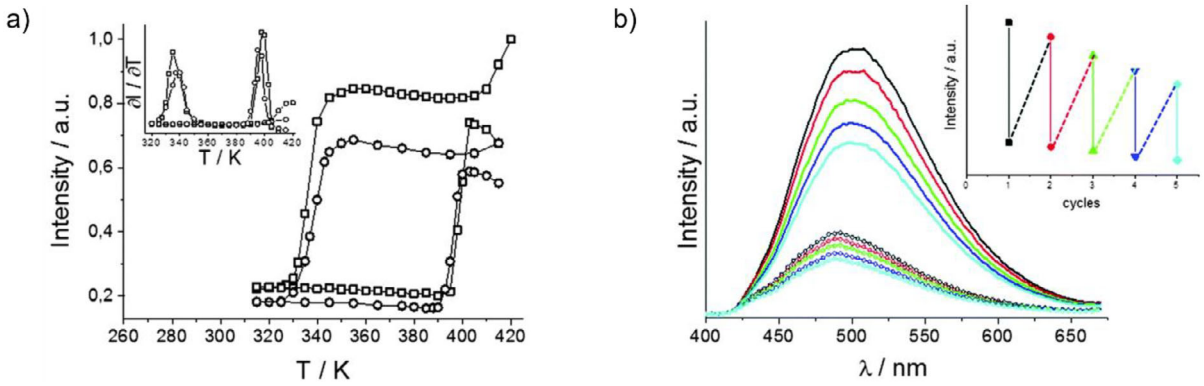

FIGURE 14 | (a) Thermal variation of the emission intensity at 494 nm (λ_{exc} = 315 nm) of the dansyl-grafted Fe**6c**@SiO_2 nanoparticles over two thermal cycles, (b) emission spectra (λ_{exc} = 315 nm) of the dansyl-grafted Fe**6c**@SiO_2 nanoparticles after successive heating (full traces) and cooling (dotted traces) cycles, highlighting the irreversible loss of signal. Reproduced from ref [55] with permission from the Royal Society of Chemistry.

located at the outer-shell and the Fe(II) centers located at the core with a rate of $5.3 \cdot 10^7$ s^{-1} [55].

4.3 | Coordination Polymers

The recent progress in the synthesis of 2D and 3D architectures has garnered growing interest in the development of coordination polymers incorporating both luminescent and SCO functionalities (Figure 15).

Having shown that crystalline $[Fe(\mathbf{1})_2](BF_4)_2$ and $[M(tpy)_2](BF_4)_2$ (M = Ni^{II}, Ru^{II}) complexes both adopted a similar "terpyridine embrace" lattice, Halcrow and co-workers [57] proposed to dope $[M(tpy)_2]$ into $[Fe(\mathbf{1})_2](BF_4)_2$ to incorporate functional centers with various redox and fluorescent properties into a solid SCO material (**1** is 2,6-di(1H-pyrazol-1-yl)pyridine depicted in Figure 6). This was the very first attempt at co-crystallizing an SCO complex with a different kinetically inert coordination complex. Five compositions of co-crystallized solid solutions of $[Fe(\mathbf{1})_2]_x[Ru(tpy)_2]_{1-x}[BF_4]_2$ were generated with x = 0.95, 0.75, 0.57, 0.47, 0.28. The thermal spin-transitions were complete and centered around 260 K in all solid mixtures, with some expected variations accurately predicted by the dilution theory [58]. Fluorescence measurements conducted at 77 K showed that $[Fe(\mathbf{1})_2]_{0.47}[Ru(tpy)_2]_{0.53}[BF_4]_2$ displayed only 7% of the fluorescence intensity of the otherwise strongly luminescent pure Ru(II) compound. Further increasing the concentration of Fe(II) centers resulted in an absence of unambiguous emission (i.e., above noise level) [59].

Tao and co-workers [60] synthesized two new hybrid SCO materials using post-synthetic methods involving the direct grafting of pyrene and rhodamine B (Rh B) fluorophores onto the 1D polymeric SCO complex $[Fe(\mathbf{6a})_3](ClO_4)_2$, ending up with 14.7% and 9.7% of ligands functionalized with pyrene to give $[Fe(\mathbf{7a})_3](ClO_4)_2$ and Rh B to give $[Fe(\mathbf{7b})_3](ClO_4)_2$ according to elemental analysis (Figure 15). Variable-temperature fluorescence spectra of the Fe-Pyr polymer displayed an initial gradual decrease in intensity upon heating, followed by a sharp increase in the 200-225 K range, and a subsequent decline (Figure 16a). The emission intensity of the Fe-Rh B system showed a similar trend, with a small shift of the inflection point toward 260 K (Figure 16b). In contrast, the emission intensity of both free grafted ligands decreased monotonously with increasing temperature. The transition temperatures extracted from the magnetic and the luminescence measurements were closely aligned ($T_{1/2}$ = 225 K instead of 230 K for Fe-pyrene and $T_{1/2}$ = 260 K instead of 263 K for Fe-Rh B), confirming the strong correlation between the fluorescence and SCO properties. The authors postulated that the luminescence enhancement originated from a reversible electron transfer from the thermally populated

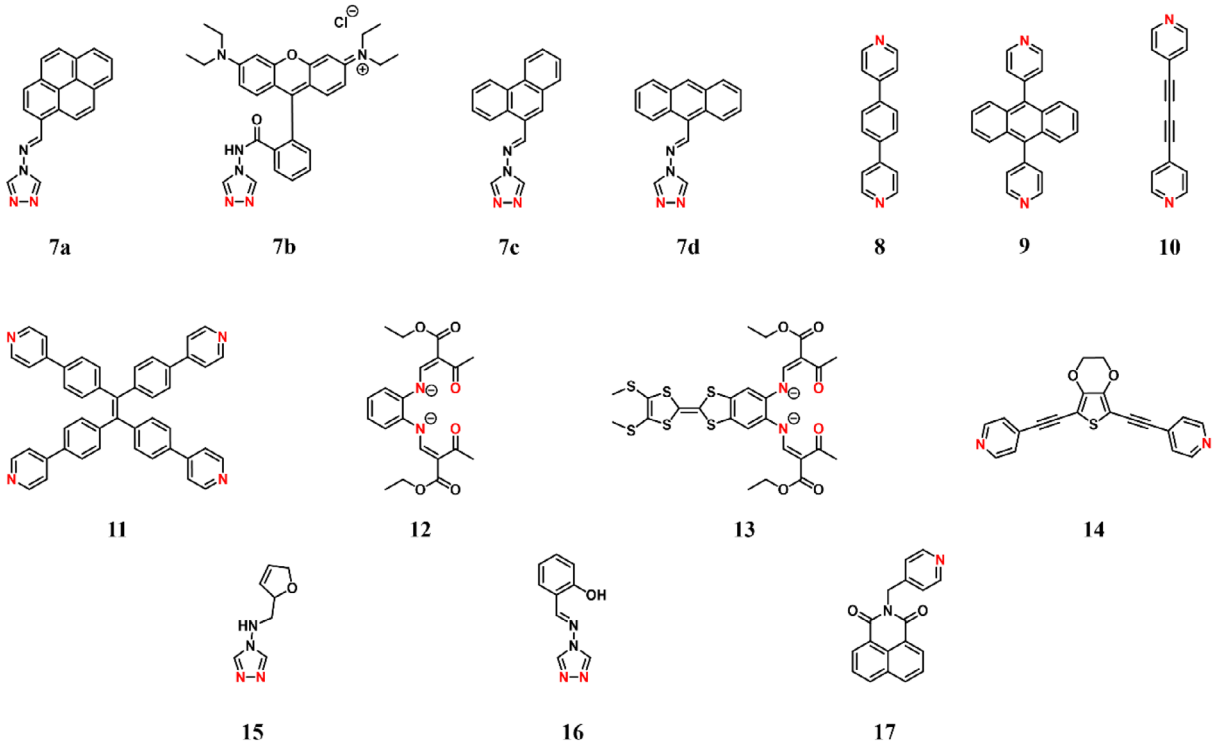

FIGURE 15 | Chemical structures of the ligands **7*k*** to **17** with the donor atoms highlighted in red.

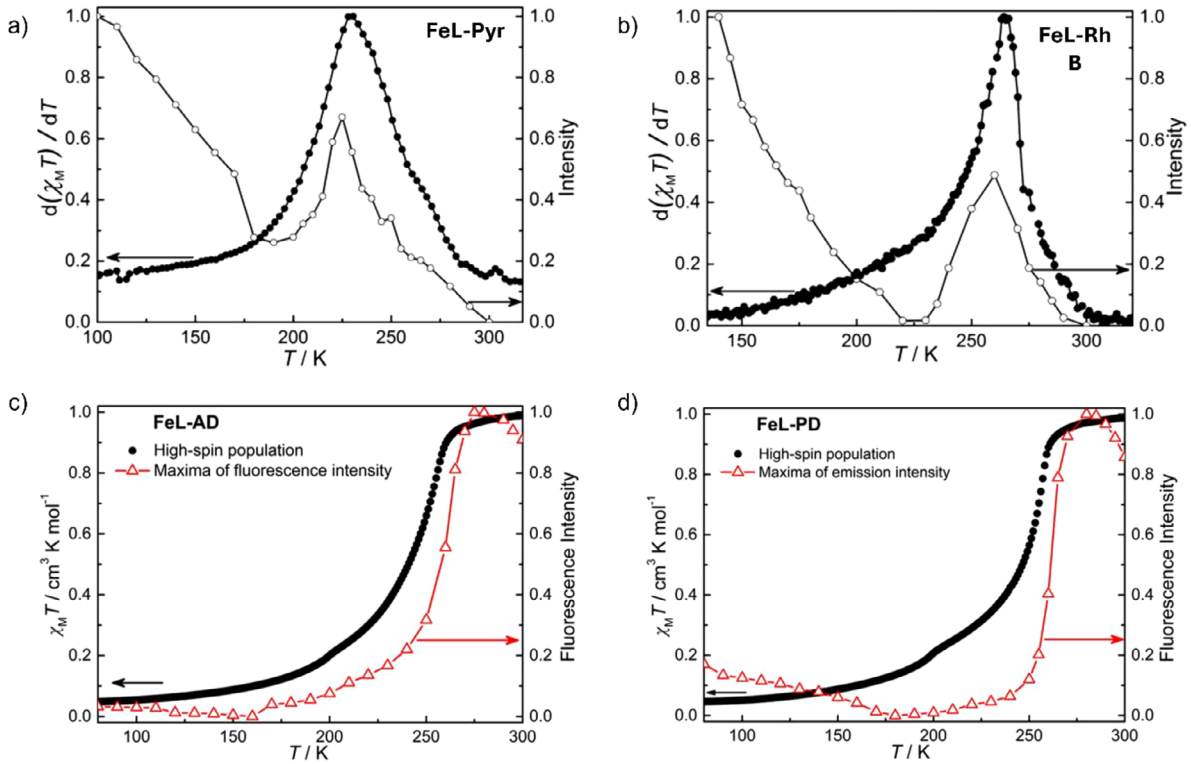

FIGURE 16 | Comparison of the fluorescence intensity of (a) Fe-Pyr in $[Fe(\mathbf{7a})_3)](ClO_4)_2$, (b) Fe-Rh B in $[Fe(\mathbf{7b})_3)](ClO_4)_2$, (c) Fe-AD in $[Fe(\mathbf{7d})_3)](ClO_4)_2$ and (d) Fe-PD in $[Fe(\mathbf{7c})_3)](ClO_4)_2$ with the normalized differential magnetic susceptibility (top panel) and with the normalized magnetic susceptibility (bottom panel). Adapted with permission from refs [60] and [61]. Copyright 2015 and 2018 Wiley-VCH.

antibonding orbitals of the Fe(II) center to the LUMO of the fluorophore [60].

A few years later, Tao and co-workers [61] grafted phenanthrene (PD) and anthracene (AD) fluorophores onto the $[Fe(\mathbf{6a})_3](ClO_4)$ complex, achieving 14.6% and 12.1% ligand functionalization in $[Fe(\mathbf{7c})_3](ClO_4)_2$ and $[Fe(\mathbf{7d})_3](ClO_4)_2$ respectively, according to elemental analysis (Figure 15). Compared to the ungrafted complex, the Fe-PD and Fe-AD polymers exhibited higher transition temperatures, with $T_{1/2}$ = 254 K upon cooling and $T_{1/2}$ = 256 K upon heating, suggesting that the substituents reinforced the ligand-field strength. The emission spectra at 80 K featured two bands at 502 and 630 nm for Fe-AD (λ_{exc} = 378 nm) and at 465 and 635 nm for Fe-PD (λ_{exc} = 390 nm), which merged into single broad bands at 300 K at 523 and 467 nm, respectively. In both systems, the fluorescence intensity initially decreased with increasing temperature, then rose sharply during the spin-transition, offering a different type of SCO–fluorescence synchronization than previously observed with the pyrene and Rh B grafted complexes (Figures 16c,d). The efficient energy transfer between the excited energy levels of the AD and PD fluorophores and the parent $[Fe(\mathbf{6a})_3](ClO_4)$ complex indeed completely quenched the fluorescence in the LS state, while the spin-transition led to a concomitant increase in the HS population and the fluorescence intensity. In contrast, the previous designs exhibited the strongest fluorescence intensity at the lowest temperature (i.e., in the LS state), with an inflection point at the transition temperature [61].

Real and co-workers [62] reported the first 3D Hofmann-type coordination polymer exhibiting synergetic SCO and luminescent properties. The SCO-MOF $\{Fe^{II}(\mathbf{8})[Au^{I}(CN)_2]\}$@pyr Fe(**8**)Au•Pyr was obtained by slow-diffusion of stoichiometric amounts of $Fe(BF_4)_2$•$6H_2O$, **8** and $K[Au^{I}(CN)_2]$ with an excess of pyrene dissolved in methanol (Figures 15 and 17). Magnetic measurements conducted between 10 and 300 K indicated a rare three-step spin-transition at 227, 195, and 180 K, with a small thermal hysteresis (5 K) in the second and third steps leading to an overall transition temperature of $T_{1/2}$ = 190 K. Variable-temperature emission showed a small increase in the intensity of the pyrene monomer and excimer fluorescence peaks at 392 and 478 nm (λ_{exc} = 332 nm) in the 300–190 K range. Upon further cooling, the intensity of the monomer signal increased significantly, whereas the excimer signal was quenched between 235 and 135 K (Figure 17a). In contrast, the Zn(II) analog displayed no significant change in intensity in the same interval, suggesting that the SCO properties strongly influenced the photoluminescence (Figure 17a). The different trends observed for the monomer and excimer signals were easily rationalized by the rise of the LS $^1A_1 \rightarrow {}^1T_1$ absorption band at 532 nm upon cooling, which quenched the excimer emission through a radiative energy transfer (emission-reabsorption), whereas the monomer band at 392 nm overlapped with the MLCT band at any temperature. Consequently, the thermal evolution of the HS molar fraction could be obtained from the ratio between the intensities at 392 and 478 nm and followed reasonably well the SCO profile obtained by absorption and magnetic measurements, providing the same $T_{1/2}$ = 189.5 K [62]. Two years later, Real and co-workers [63] investigated the modulation of the luminescence in two series of doubly-interpenetrated SCO Hofmann-type 3D coordination polymers based on (i) the anthracene-substituted bridging ligand **9** displaying intrinsic luminescence, and (ii) the pillar ligand **10** with pyrene guest molecules displaying extrinsic luminescence (Figure 15). Four clathrates of general formula $\{Fe^{II}(\mathbf{L})[M^{I}(CN)_2]_2\}$ with **L** = **9**, **10** and M = Ag, Au were investigated, with the Fe(**10**)Ag•Pyr/Fe(**10**)Au•Pyr series containing about one pyrene guest per Fe(II) ion (Figure 17). In Fe(**9**)Au, the pyridine moieties are nearly orthogonal with respect to the anthracene fragments to minimize the intra- and inter-network repulsion between the H atoms at 280 K, but no longer at 200 K. In Fe(**10**)Ag•Pyr, the pyrene guests are positioned face-to-face with the pyridine of the ligands **10**, which provides numerous π–π interactions.

The thermal evolution of the pyrene fluorescence (λ_{exc} = 345 nm) of Fe(**10**)Ag•Pyr was very similar to that of the Fe(**8**)Au•Pyr analog, with an increase in the intensity of the monomer signal between 350 and 450 nm while the excimer band around 450–700 nm was significantly quenched due to its overlap with the optical absorption of the LS species (Figure 17c). As for the pyrene-doped polymers, the excimer emission (λ_{exc} = 345 nm) around 490–700 nm of Fe(**9**)Ag progressively disappeared upon cooling (below 230 K) whereas the monomer signal between 350 and 490 nm increased into a well-structured band because of the high optical absorption of the LS species within the range of the excimer emission (Figure 17b). Overall, a greater synergy was observed in the extrinsic Fe(**10**)Ag•Pyr/Fe(**10**)Au•Pyr series. Potential reasons involve (i) the shorter pyrene-Fe distances facilitating non-radiative energy transfers, and (ii) weaker excimer fluorescence of the anthracene due to weaker π–π interactions. The geometry of the polymer, and more specifically the localization of the luminophore with respect to the SCO center seem to be the key parameter in the SCO-luminescence synergy, more so than the extrinsic or intrinsic nature of the luminescence, even though extrinsic luminescence allows a greater capacity to control the geometry due to the easy insertion of different guests, thus appearing as a more promising endeavor for future studies [63].

Zuo and co-workers [64] designed the 2D coordination polymer $\{[Fe(\mathbf{12})](\mathbf{11})_{0.5}\cdot 3CH_3OH\}_n$ combining the strongly luminescent ligand **11**, featuring four divergent pyridine rings ideally suited for constructing a square-grid architecture, with the planar SCO $[Fe(\mathbf{12})(CH_3OH)_2]$ complex based on the Schiff base ligand **12** (Figure 15). Magnetic susceptibility measurements revealed an incomplete spin-transition with $T_{1/2}$ = 202 K upon cooling and $T_{1/2}$ = 227 K upon heating. Temperature-dependent fluorescence spectra showed a notable increase in the intensity of the unique broad band at 460 nm (λ_{exc} = 365 nm) in the 120–200 K range, followed by a gradual decrease upon further heating. In contrast, the emission intensity of the free ligand **11** exhibited a continuous and monotonic decline throughout the whole temperature range. Based on extensive TD-density functional theory (DFT) calculations, the authors attributed the luminescence quenching in the LS state to an energy transfer from the ligand **11** to the Fe(II) centers, while the decline following the spin-transition was ascribed to enhanced intramolecular charge-transfer processes in the HS state. As such, this study marked the first example of a 2D coordination polymer exhibiting intrinsic modulation of luminescence by the SCO process [64]. A few years later, Su and co-workers [65] modified the Schiff-base ligand **12** to incorporate the redox-active tetrathiafulvalene (TTF) moiety in the planar $[Fe(\mathbf{13})(CH_3OH)_2]$ complex (Figure 15). The resulting coordination polymer $\{[Fe(\mathbf{13})](\mathbf{11})_{0.5}\}_n$ exhibited a redox activity

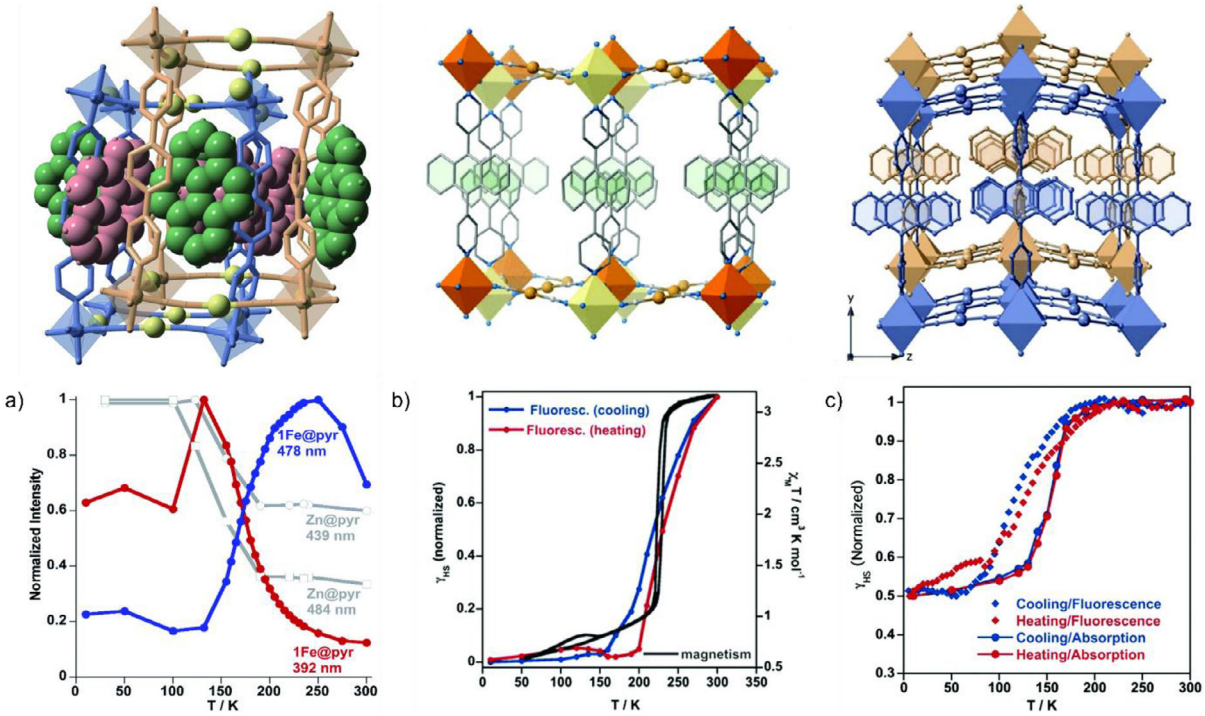

FIGURE 17 | Top panel: crystal structures and of the Fe(**8**)Au•Pyr (top left), Fe(**9**)Ag (top center), and Fe(**10**)Ag•Pyr (top right) coordination polymers; bottom panel: (a) thermal evolution of the normalized luminescence intensity (λ_{exc} = 332 nm) of the monomer (at 392 nm, red trace) and excimer (at 478 nm, blue trace) of Fe(**10**)Au•Pyr and Fe(**10**)Au•Pyr (at 439 and 484 nm, gray traces), and HS fraction obtained from the ratio of the monomer emission over the excimer emission in the heating and cooling modes for (b) Fe(**9**)Ag and (c) Fe(**10**)Ag•Pyr. Adapted from refs [62] and [63] with permission from the Royal Society of Chemistry.

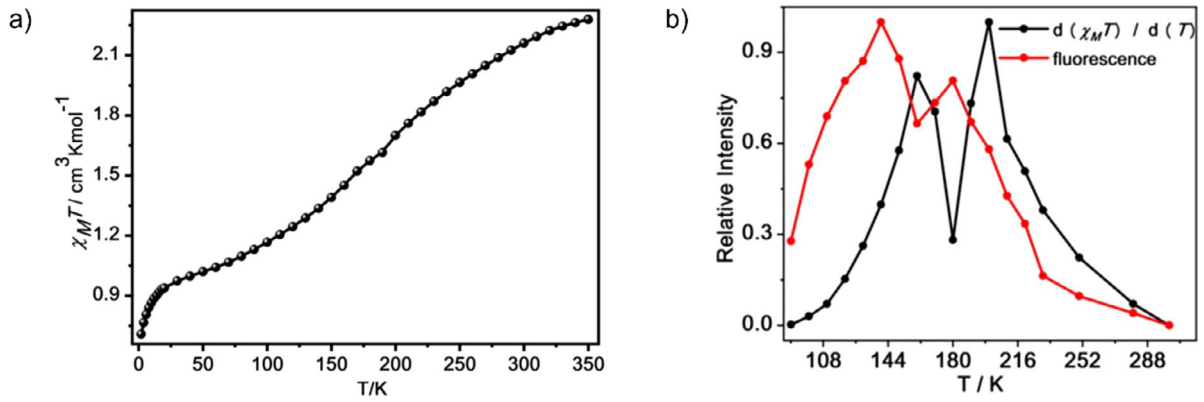

FIGURE 18 | (a) Thermal evolution of the $\chi_M T$ product of $\{[Fe(\mathbf{13})](\mathbf{11})_{0.5}\}_n$, and (b) comparison of the temperature-dependent normalized emission intensity at 442 nm (λ_{exc} = 360 nm) with the normalized differential magnetic susceptibility for $\{[Fe(\mathbf{13})](\mathbf{11})_{0.5}\}_n$. Adapted with permission from ref [65]. Copyright 2021 Qiu, Cui, Ge, Kurmoo, Ma, and Su.

akin to that of the isolated TTF unit, as well as a gradual spin transition. Variable-temperature fluorescence spectra revealed an initial increase in the ligand-centered emission at 442 nm (λ_{exc} = 360 nm) between 90 and 140 K, followed by a decrease until 160 K, another increase peaking at 180 K, and a final continuous decline upon further heating. Even though these unusual fluctuations in the fluorescence intensity occurred within the same temperature range as the thermal spin-transition (90–300 K), the normalized differential magnetic susceptibility of $\{[Fe(\mathbf{13})](\mathbf{11})_{0.5}\}_n$ was only loosely consistent with the modulation of the luminescence (Figure 18b). Nevertheless, the authors attributed these discrepancies to differences in the thermal sweep rates used in the magnetic and fluorescence measurements [65].

Mondal and co-workers [66] used another redox-active luminescent ligand **14** in their 2D coordination polymer $\{[Fe(\mathbf{14})_2(NCSe)_2]\cdot 6CH_3OH\cdot 14H_2O\}_n$ (Figure 15). Magnetic susceptibility measurements confirmed the SCO behavior, revealing a complete spin-transition with $T_{1/2}$ = 155(1) K and no thermal hysteresis. Upon irradiation with white light for 100 min at 10 K, the absolute reflectivity sharply increased to a level close to the one obtained at 270 K, indicating an

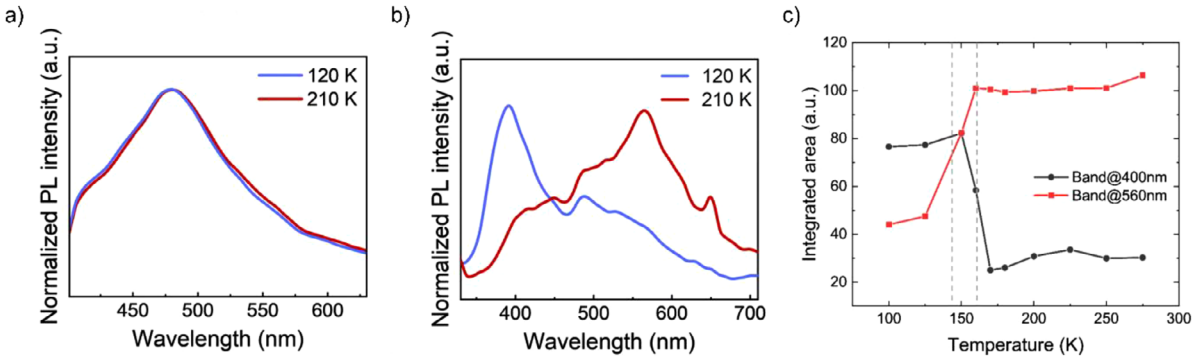

FIGURE 19 | Normalized emission spectra (λ_{exc} = 325 nm) in the LS (blue traces, 120 K) and HS states (red traces, 210 K) of bulk crystals of (a) Furtrz and (b) Saltrz, and c) thermal evolution of the normalized emission intensity of Saltrz at 400 (red trace) and 560 nm (black trace). Reproduced from ref [67] with permission from the Royal Society of Chemistry.

almost complete recovery of the HS state through the LIESST effect. Further investigations revealed that the HS and LS states could be reversibly and efficiently switched by using 625 and 850 nm irradiation across multiple cycles. Variable-temperature fluorescence measurements carried out from 270 to 70 K showed an initial decrease in the intensity of the broad emission band at 524 nm, reaching a minimum around 150 K, followed by an increase upon further cooling. Although these results suggested a correlation between the luminescent properties and the SCO process, no attempt was made to rationalize the mechanism of interaction [66].

While exploring the miniaturization by mechanical exfoliation of the newly synthesized $\{Fe(\mathbf{15})_2[Pt(CN)_4]\}\bullet 4\ H_2O$ (Furtrz) and the previously reported $\{Fe_3(\mathbf{16})_6[Pt(CN)_4]_3\}\bullet 8\ H_2O$ (Saltrz) 2D Hofmann-like coordination polymers (Figure 15), Clemente-Leon and co-workers [67] recognized that the ligand used in the latter compound had previously been shown by Garcia and co-workers [68] to exhibit synergistic luminescence-SCO properties, which prompted them to investigate its optical behavior. Remarkably, the emission spectra (λ_{exc} = 325 nm) of Saltrz recorded at 120 K (LS state) and 210 K (HS state) exhibited completely different profiles: at 120 K, a band centered around 400 nm with a broad shoulder tailing up to *ca*. 650 nm dominated the spectrum, while at 210 K, the latter band was quenched and replaced by a broad structured band centered around 560 nm (Figure 19b). The temperature-dependent evolution of the integrated luminescence intensities at 400 and 560 showed abrupt changes around 150 K, coinciding with the temperature range of the main spin-transition ($T_{1/2}$ = 156 K, Figure 19c) [69]. This striking red-shift of the emission maximum from 400 to 560 nm upon the spin-transition mirrored the behavior previously reported by Garcia and co-workers [68] and confirmed that the correlation between the two functionalities also applied to Saltrz. In contrast, the emission spectra of Furtrz and the isostructural Zn(II) references remained unaltered throughout the whole temperature range (Figure 19a) [67].

Lastly, Kou and Tao [70] conjointly reported the new 2D Hofmann-type SCO-MOF $\{Fe^{II}(\mathbf{17})_2[Ag^{I}(CN)_2]_2\}\cdot CHCl_3$ ($\mathbf{17}$Ag·$CHCl_3$) using the monodentate ligand **17**, known for generating stable excimer excited states (Figure 15) [71]. Temperature-dependent magnetic measurements exhibited significant solvent-dependence of the SCO properties, a well-documented phenomenon [72, 73], switching from a three-step hysteretic spin-transition in $\mathbf{17}$Ag·$CHCl_3$ (with $T_{1/2}$ = 212, 156, and 131 K upon cooling and 212, 151, and 136 K upon heating) to an abrupt one-step process upon removal of the solvent guests in **17**Ag (with $T_{1/2}$ = 194 K upon cooling and 233 K upon heating). The evolution of the normalized emission intensities of the monomer and excimer bands (centered around 494 and 601 nm, respectively, λ_{exc} = 365 nm) in both **17**Ag and $\mathbf{17}$Ag·$CHCl_3$ exhibited a complex temperature-dependence that loosely followed the thermal evolution of the $\chi_M T$ product (Figures 20a,b). Notably, the desolvated polymer displayed luminescence hysteresis loops, which clearly supported a synergistic relationship between the SCO behavior and the luminescence properties (Figure 20a). Furthermore, the isostructural Zn(II) analog displayed the expected thermal quenching of emission upon heating, providing additional evidence for the coupling of the two functionalities. Mechanistic studies based on variable-temperature diffuse reflectance spectra and TD-DFT calculations attributed the fluorescence enhancement observed upon the spin-transition to a reduction in absorption in the HS state [70].

5 | Materials Combining the Luminescent and SCO Units Into A Single Molecular Assembly

A conceptually contrasting yet equally prevalent strategy for designing luminescent SCO materials consists of incorporating the SCO unit and the light-emitting moiety within the same chemical entity. This approach enables a clear elucidation of the structural relationship between the SCO center and the fluorophore, hence providing the opportunity to rationalize their interactions [12]. In addition, these systems benefit from a concentration-independent response, which makes them particularly attractive for (bio)sensing applications [74]. However, this strategy comes with its own set of challenges, the most notable being (i) the potential loss of one or both functionalities, and (ii) the inability to determine beforehand whether the two properties will be coupled or merely coexist. The stoichiometric ratio of the two components in the final assembly may also lead to undesirable self-quenching effects, reducing the luminescence intensity and, in turn, the efficiency of the material [11, 12, 75].

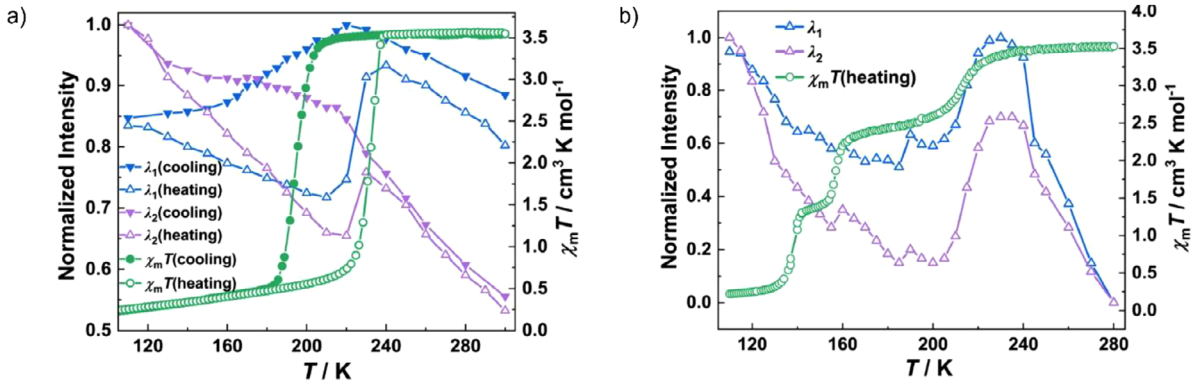

FIGURE 20 | Comparison of the temperature-dependent normalized maximum emission intensity at $\lambda_1 = 494$ nm and $\lambda_2 = 601$ nm ($\lambda_{exc} = 365$ nm) for (a) $\{Fe^{II}(\mathbf{17})_2[Ag^I(CN)_2]_2\}$ (= **17**Ag) over consecutive cooling and heating cycles, and for (b) **17**Ag·$CHCl_3$ upon heating with their corresponding $\chi_M T$ products. Reprinted with permission from ref [70]. Copyright 2024 Springer Nature.

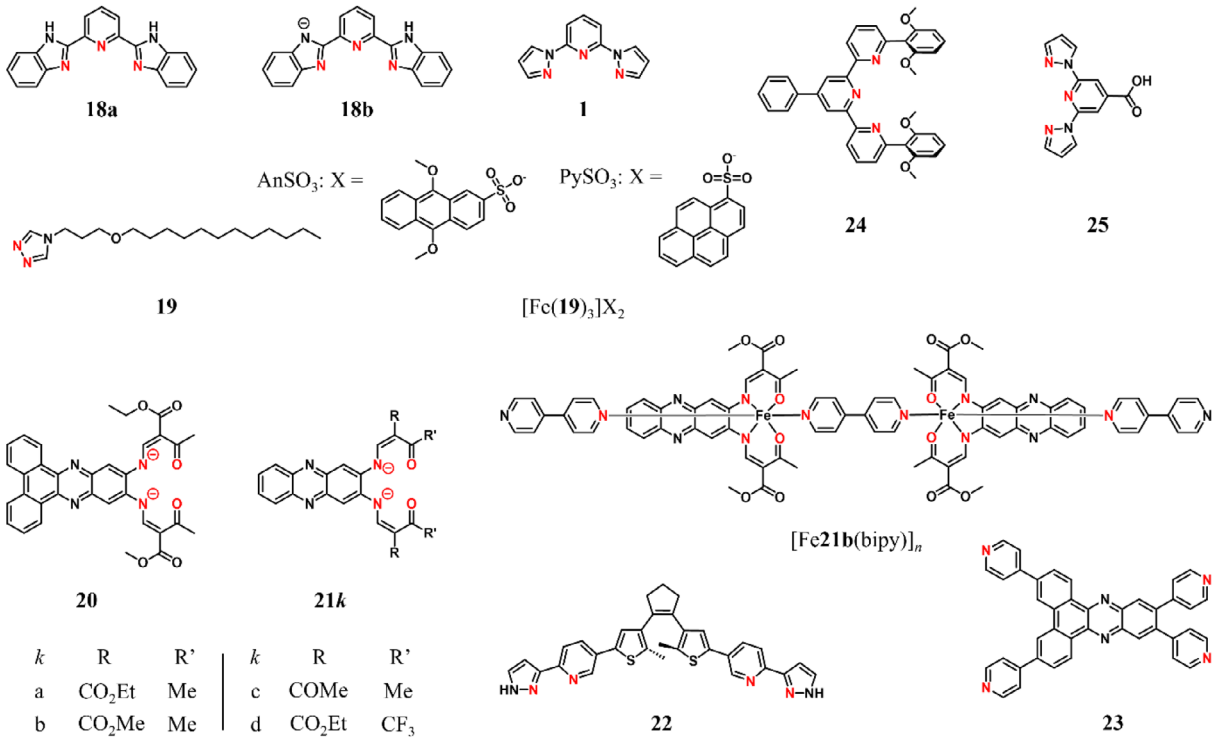

FIGURE 21 | Chemical structures of the ligands **18**–**23** with the donor atoms highlighted in red.

5.1 | p-Block Luminophores: Luminescent Ligands and Counter Anions

The simplest, and arguably most elegant, way of integrating the chromophore and SCO unit within a single molecular structure is to use an intrinsically luminescent ligand. However, given that the ligand-field splitting energy must remain within the narrow range compatible with the emergence of SCO properties, the tunability of these systems is severely restricted. As a result, the ligands examined in this section (Figure 21) primarily consist of well-established SCO-inducing motifs, the temperature-dependent luminescent properties of which were studied to gain mechanistic insights into the interplay between luminescence and SCO (Figure 6).

In a pioneering study, Hasegawa and co-workers [76] conducted a detailed investigation of the temperature-dependence of the emission and excitation spectra of two mononuclear Fe(II) SCO complexes based on the fluorescent 2,6-bis(benzimidazole-2'-yl)pyridine ligand **18a**, and its mono-deprotonated counterpart **18b** (Figure 21). By meticulously assigning the absorption and fluorescence spectra of $[Fe(\mathbf{18a})_2](ClO_4)_2$ and $[Fe(\mathbf{18b})_2]$ in 1:1 methanol/ethanol solutions, they were able to show that (i) both complexes were fluorescent in both spin-states, and (ii) the changes observed in the excitation and the fluorescence spectra upon cooling were related to the changing ratio of HS and LS species. From the position of the fluorescence bands assigned to each spin-state, they deduced the energy difference ΔE between the two configurations and applied the Boltzmann equation (Equation 15) to calculate their relative populations at different

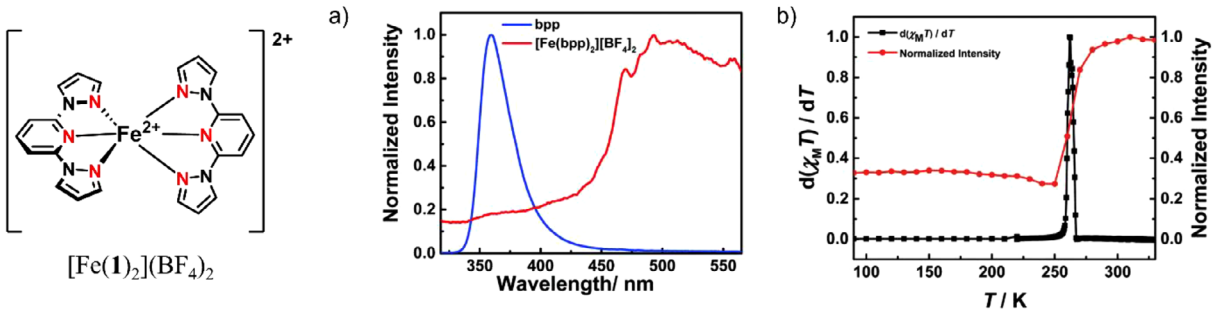

FIGURE 22 | (a) Solid-state emission spectra of the free ligand **1** (blue line), and $[Fe(\mathbf{1})_2](BF_4)_2$ complex (red line) at room temperature (λ_{exc} = 298 nm), and (b) comparison of the temperature-dependent evolution of the normalized luminescence intensity of $[Fe(\mathbf{1})_2](BF_4)_2$ at 493 nm (red line) with the differential magnetic susceptibility (black line). Reprinted from ref [77] with permission from the Royal Society of Chemistry.

temperatures (N_{HS} and N_{LS} are the populations of HS and LS species, respectively, k_B is the Boltzmann constant, and T is the temperature).

$$\frac{N_{HS}}{N_{LS}} = e^{-\Delta E/k_B T} \tag{15}$$

The resulting ratios were in excellent agreement with those previously obtained with other techniques, hence demonstrating for the first time that the temperature-dependent fluorescence of a SCO complex could be used as a quantitative measure of the proportion of each spin-state [12]. Following up on this work, Guo and co-workers [77] investigated the luminescent properties of the related $[Fe(\mathbf{1})_2](BF_4)_2$ complex, in which the benzimidazole substituents were replaced with pyrazole rings (Figure 21). In solution, the emission spectrum of the complex closely resembled that of the free ligand, exhibiting a unique signal centered around 359 nm. However, in the solid state, a much broader emission band, attributed to the radiative decay of the MLCT state, was observed between 450 and 565 nm, with minimal residual ligand-centered emission (Figure 22a). Variable-temperature fluorescence measurements performed in the solid state revealed an abrupt enhancement in the emission intensity between 250 and 280 K, coinciding with the temperature range of the spin-transition ($T_{1/2}$ = 260(1) K, Figure 22b) [78]. Given the negligible contribution of ligand-centered emission and the concomitance of the luminescence enhancement with the spin transition, this effect was ascribed to a synergistic interplay between SCO and luminescence. An extensive computational study suggested that the pairing of the electrons in the t_{2g} orbitals in the LS state made the intramolecular electron transfer from the metal to the ligand less favorable, thereby hindering the population of the lowest excited state. Based on these conclusions, the authors rationalized that the enhanced MLCT luminescence in the HS state stemmed from a greater excitation efficiency [77]. It should be noted that despite the promising correlation observed between their SCO and luminescent properties, neither $[Fe(\mathbf{18a})_2](ClO_4)_2$, $[Fe(\mathbf{18b})_2]$ nor $[Fe(\mathbf{1})_2](BF_4)_2$ exhibited strong enough luminescence to be considered for practical applications.

As part of their work on lipophilic one-dimensional coordination systems, Kimizuka and co-workers [79] investigated the self-assembly of linear SCO tris(4-(3-dodecyloxypropyl)-1,2,4-triazole) Fe(II) $[Fe(\mathbf{19})_3]^{2+}$ complexes (Figure 21), and their potential application in the regulation of photorelaxation processes. However, instead of monitoring the intrinsic luminescence of the ligand **19**, they introduced aromatic chromophores (namely 9,10-dimethoxyanthracene-2-sulfonate, $AnSO_3$, and 1-pyrenesulfonate $PySO_3$, Figure 21) as counter-ions. This conceptually related strategy, which relies on electrostatic interactions rather than covalent bonding to couple the luminophore to the SCO unit, provides greater flexibility for tuning the properties of the system by tailoring individual components [12]. Dispersions of $[Fe(\mathbf{19})_3](AnSO_3)_2$ and $[Fe(\mathbf{19})_3](PySO_3)_2$ in toluene experienced an abrupt spin-transition near room temperature (RT), as evidenced by their temperature-dependent absorption spectra, which revealed a sharp decrease in the intensity of the $\pi^*\leftarrow$LS-Fe^{II} MLCT band and the $^1T_1\leftarrow{}^1A_1$ d-d transition. The significant spectral overlap between the MLCT band and the fluorescence of $PySO_3$ resulted in pronounced fluorescence quenching in the LS state, whereas the emission of $AnSO_3$ remained largely unaffected (Figure 23a). As the thermal spin transition progressed, the fluorescence of the pyrene counterion increased three-fold, reaching a maximum at 303 K before decreasing due to the thermal disintegration of the fibrous nanostructures. Interestingly, performing several cycles of heating and cooling shows that the fluorescence and absorbance intensity changes were reversible, which suggested that the fragmentation of the labile HS complex was a dynamic process that occurred synergistically with the spin-transition [79].

In 2015, Weber and co-workers [80] reported two new Schiff base-like ligands **20** and **21a**, each possessing a fluorophore embedded in the structure, and the corresponding Ni(II), Cu(II), and Zn(II) square-planar complexes (Figure 21). The progressive addition of pyridine to chloroform solutions of [Ni**20**] and [Ni**21a**] induced a change in the geometry of the complexes, which in turn triggered a change in the spin state of the Ni(II) center (Figure 23b). This so-called "Coordination Induced Spin-State Switching" (CISSS) dramatically affected the luminescent properties of [Ni**20**] and [Ni**21a**], albeit in different ways. The diamagnetic square-planar complexes [Ni**20**] and [Ni**21a**] both displayed fluorescent bands at 478 (λ_{exc} = 448 nm) and 491 nm (λ_{exc} = 465 nm), respectively. Upon addition of pyridine, the emission of $[Ni\mathbf{21a}(C_5H_5N)_n]$ (n = 1, 2) was progressively red-shifted and decreased in intensity with increasing equivalents of pyridine, whereas that of $[Ni\mathbf{20}(C_5H_5N)_n]$ (n = 1, 2) was abruptly shifted to 538 nm, then increased in intensity until around 400 equivalents of pyridine were added, before going down upon further addition. While the quenching of the luminescence and the reduced lifetime of $[Ni\mathbf{21a}(C_5H_5N)_n]$ (n = 1, 2) were both consistent with the

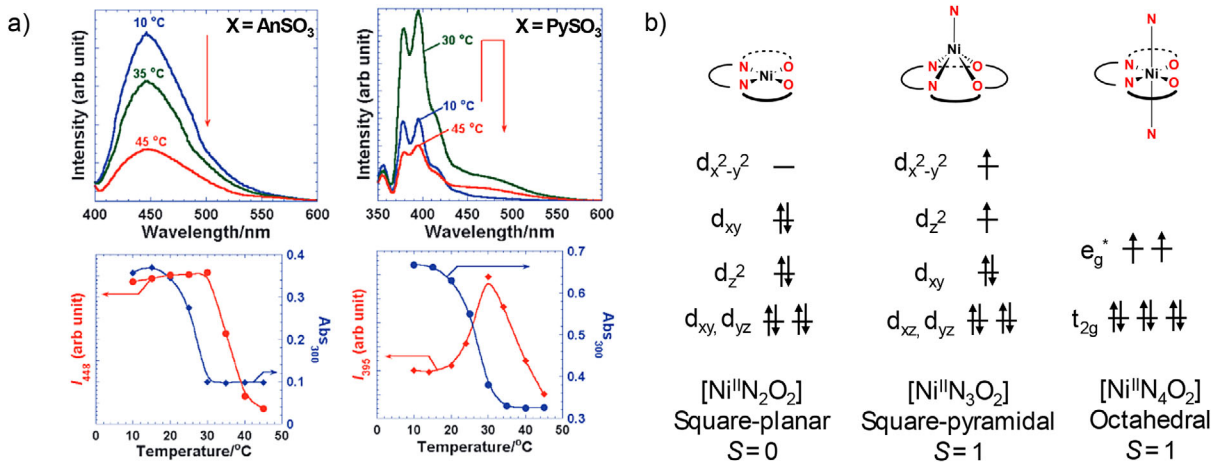

FIGURE 23 | (a) Temperature-dependence of the fluorescence spectra (top panels) and of the fluorescence and absorbance intensities (bottom panels, red and blue lines respectively) of [Fe(**19**)$_3$](AnSO$_3$)$_2$ (λ_{exc} = 348 nm, left side) and [Fe(**19**)$_3$](PySO$_3$)$_2$ (λ_{exc} = 380 nm, right side) upon heating (used with permission of Oxford University Press and the Chemical Society of Japan, from ref [79]; permission conveyed through Copyright Clearance Center, Inc.), and (b) electronic configurations associated with the geometries of the [Ni**20**] and [Ni**21a**] complexes in equilibrium following the addition of pyridine.

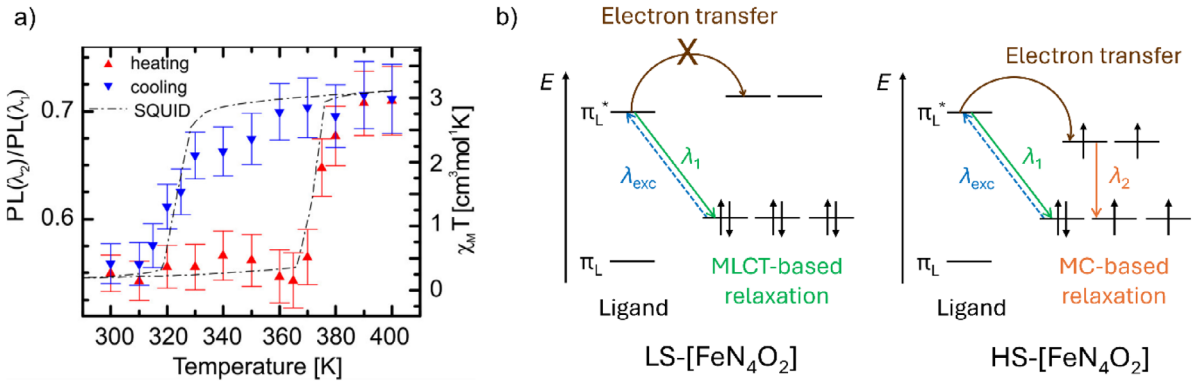

FIGURE 24 | (a) Comparison of the temperature-dependent photoluminescence ratio I_{550}/I_{686} with the magnetic susceptibility temperature product ($\chi_M T$) for [Fe(**21b**)(bipy)]$_n$. (Reprinted with permission from ref [81]; Copyright 2018 American Chemical Society), and (b) schematic representation of the competing relaxation processes occurring in the LS and HS states of the [Fe(**21b**)(bipy)]$_n$ polymer.

emergence a non-radiative energy transfer, the appearance of a second contribution with a longer lifetime once a certain amount of pyridine equivalents was reached in [Ni**20**(C$_5$H$_5$N)$_n$] (n = 1, 2) could not be rationalized [80]. Three years later, Weber and co-workers [81] synthesized a one-dimensional Fe(II) SCO coordination polymer based on the luminescent polyaromatic Schiff-base ligand **21** to investigate whether the coupling between luminescence and CISSS previously observed in [Ni**21a**] could also be achieved in the case of a thermally induced spin transition (Figure 21). The solid-state emission spectrum of [Fe(**21b**)(bipy)]$_n$ exhibited two bands centered around 550 and 673 nm (λ_{exc} = 337 nm), the relative intensities of which varied in accordance with the spin-transition. A comparison of the temperature-dependent luminescence intensity ratio (I_{550}/I_{686}) with the evolution of magnetic susceptibility unambiguously confirmed the correlation between the SCO process and the fluorescence (Figure 24a). The distinct trends followed by each emission band suggested that they had different electronic origins. The lower-energy emission was assigned to a metal-centered (MC) e_g*→t_{2g} transition, possibly mixed with ligand-based π orbitals, whereas the higher-energy band was ascribed to a MLCT-based π*→t_{2g} relaxation. The unusual presence of a dual emission in the HS state indicated that the MLCT and MC-based processes occurred competitively, with the former dominating in the LS state, and the latter becoming more efficient in the HS state (Figure 24b) [81].

In 2021, Weber and co-workers [74] extended their investigation on the switchable luminescence of [Ni**21a**] and examined the impact of lateral substitution of the ligand backbone on the fluorescence properties of a new series of [Ni**21*k***] (k = a, b, c, d) complexes (Figure 21). Among these, [Ni**21b**] and [Ni**21c**] were both found to be luminescent in non-coordinating solvents, displaying a unique emission band centered around 477/478 nm (λ_{exc} = 385 nm). Upon pyridine addition, the intensity of the fluorescence decreased significantly, to the point of being practically extinguished in pure pyridine. The addition of electron-withdrawing substituents in [Ni**21d**] seemed to enhance its sensitivity to CISSS, as the increased acidity of the metal favored the coordination of Lewis bases. Nevertheless, [Ni**21d**] was the

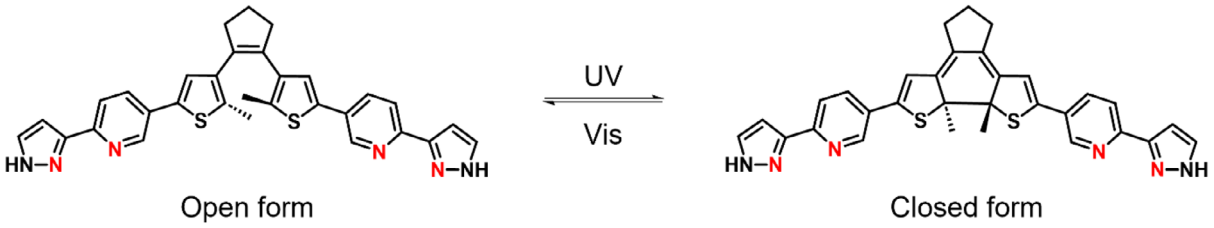

FIGURE 25 | Reversible photocyclization of the ligand **22**.

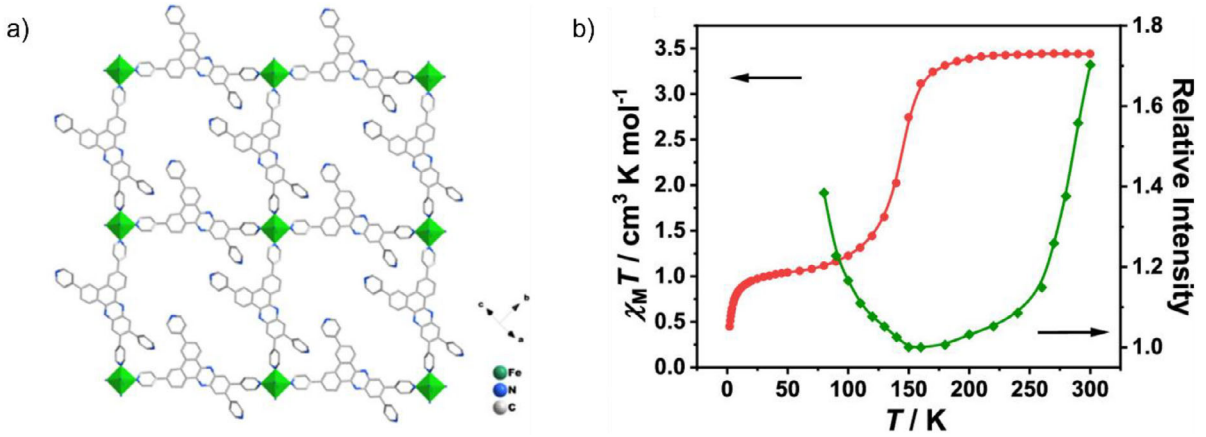

FIGURE 26 | (a) Chemical structure of the 2D [4x4] network SG2, highlighting the connection of the polypyridine ligand **23** and the $Fe(NCSe)_2$ units, and (b) comparison of the normalized emission intensity at 450 nm with the magnetic susceptibility temperature product ($\chi_M T$) for desolvated SG2. Reprinted with permission from ref [83]. Copyright 2022 American Chemical Society.

only non-emissive complex of the series. Overall, these findings highlighted how fluorescence-detected CISSS (FD-CISSS) provided greater sensitivity than steady-state UV−vis measurements to monitor changes in the geometries of the complexes [74].

Aromí and co-workers [82] explored another facet of luminescent SCO materials, in which the irradiation of the photochromic unit induced structural changes that affected the magnetic response of the complex. This approach contrasts with the more conventional strategy, in which the fluorophore is used as an optical readout of the spin-state equilibrium. They designed ligand **22** by connecting two pyrazolylpyridine moieties with a dithienylethene photochromic switch, which undergoes reversible ring-closing/opening reactions upon irradiation with UV/visible light, respectively (Figure 25). In solution, the full and reversible photoisomerization of the dinuclear triple-stranded helicate $[Fe_2\mathbf{22}_3](ClO_4)_2$ switched on and off the emission band around 440 nm and reversibly shifted the transition temperature. However, no direct correlation between the thermal spin-transition and the fluorescence response could be evidenced [82].

In their search for stable multidimensional coordination polymers showing a correlation between SCO and luminescence, Song and co-workers [83] designed the tetradentate ligand **23** by grafting pyridine rings onto a dibenzo[*a*,*c*]phenazine fluorescent dye (Figure 21). Upon complexation with $Fe(NCX)_2$ (X = S, Se), two 2D [4x4] square-grid complexes $[Fe^{II}(\mathbf{23})_2(SCN)_2{\cdot}CHCl_3{\cdot}4CH_3OH]_n$ (SG1) and $[Fe^{II}(\mathbf{23})_4(SeCN)_2{\cdot}CH_2Cl_2{\cdot}4CH_3OH]_n$ (SG2) were obtained (Figure 26a). Magnetic susceptibility measurements conducted in the 1.8–300 K range showed a gradual and incomplete spin-transition in SG1 with $T_{1/2}$ = 110 K, whereas SG2 exhibited a one-step, almost complete spin-transition with $T_{1/2}$ = 144 K and no thermal hysteresis. Variable-temperature fluorescence measurements conducted on partially desolvated SG2 revealed that the normalized fluorescence emission intensity at 450 nm (λ_{exc} = 330 nm) initially decreased upon heating (between 80 and 150 K) before increasing steadily in the 150–300 K range. In contrast, the emitted intensity of the free ligand **23** decreased monotonously with rising temperatures. Considering that the inflection point in the emission intensity of desolvated SG2 coincided with the transition temperature and that the fluorescence intensity was greater at elevated temperature (as opposed to the expected thermal quenching), the fluorescent behavior of SG2 thus appeared to be modulated by the SCO process (Figure 26b). The significant increase in fluorescence intensity upon the spin-transition was tentatively rationalized by (i) reduced intermolecular contact interactions between **23** and the NCSe unit after the spin-transition, which would decrease the efficiency of intermolecular non-radiative energy transfers in the HS state, and (ii) a reduction in the spectral overlap between the MLCT absorption band and the emission of the complex upon spin-state switching [83].

Liu and co-workers [84] reported the heteroleptic SCO complex $[Fe(\mathbf{24})(\mathbf{25})](BF_4)_2{\bullet}H_2O$ based on the complementary terpyridine ligand pair strategy developed by Chan's group (Figure 21) [85]. The complex displayed a gradual albeit complete spin-transition between 150 and 350 K without thermal hysteresis. Temperature-

dependent fluorescence spectra recorded from 80 to 300 K (heating mode) showed a gradual decrease in the emitted intensity of the main fluorescence band at 438 nm (λ_{exc} = 360 nm) until 225 K, while a sharp enhancement of the luminescence was observed upon further heating. In comparison, the variable-temperature emission of analogous [Co(**24**)(**25**)]$(BF_4)_2$ and [Zn(**24**)(**25**)]$(BF_4)_2$ complexes exhibited the expected thermal quenching of luminescence, thereby confirming the strong coupling between the spin-transition and the fluorescence in [Fe(**24**)(**25**)]$(BF_4)_2$•H_2O. Despite extensive DFT calculations, no definitive conclusion has yet been reached regarding the exact nature of the interaction mechanism [84].

Real and co-workers recently designed an ionogenic ligand based on an asymmetrically substituted (1*H*-1,2,4-triazol-5-yl)-6-(1*H*-pyrazol-1-yl)pyridine tridentate core that yielded mononuclear Fe(II) complexes with remarkably large hysteresis loops centered around R*T* [86]. Introducing a 4-chlorophenyl substituent on the 3-position of the pyrazol ring provided the related neutral complex [Fe(**26**)$_2$] (Figure 21), which displayed a 60 K wide hysteresis ($T_{1/2}$ = 308 K upon heating and $T_{1/2}$ = 248 K upon cooling) as well as temperature-dependent fluorescent properties [87]. Variable-temperature emission measurements (λ_{exc} = 275 nm) conducted in the heating mode revealed a good correlation between the sudden increase in the emission intensity of the three bands at 396, 530, and 610 nm in the 300-350 K range and the HS mole fraction derived from magnetic measurements. However, the corresponding decrease in emitted intensity observed in the 200-100 K range in the cooling mode could not be satisfactorily related to the magnetic data. This mismatch was tentatively ascribed to a combination of (i) changes in the absorption properties and (ii) the so-called light-induced perturbation of thermal hysteresis (LiPTH), a phenomenon whereby the continuous absorption of light by the compound locally generates heat, which alters the actual temperature of the sample and shifts the transition temperature toward lower values [88, 89]. A reversible bathochromic/hypsochromic shift of the emission maximum of the high-energy band (390–440 nm) upon heating/cooling, respectively, was also measured, thereby leading to a distinct change in the color of the emitted light observable with the naked eye [87].

5.2 | p-Block Luminophores: Covalently Bound Organic Dyes

An alternative to the design of intrinsically luminescent ligands capable of inducing SCO consists of covalently bonding an organic chromophore to a SCO complex through a chemical bridge of adjustable length. The strong emission of most organic fluorophores allows for substantial intensity modulation by spin-state switching, a feature that is particularly attractive for practical applications. Nevertheless, these systems often suffer from photobleaching, leading to notable decreases in signal intensity over time.

More than a decade before Weber and co-workers [80] started working on the luminescent properties of CISSS Ni(II) complexes, Fabbrizzi and co-workers [90] designed a fluorescent molecular thermometer based on a Ni(II) complex with the naphthalene-substituted cyclam **27** (Figure 27). Depending on the nature of the counter anions, the complex could be isolated either as the yellow diamagnetic square-planar LS complex [Ni**27**]X_2 (X = ClO_4^-, $CF_3SO_3^-$), or as the blue-violet octahedral HS complex [Ni**27**X_2] (X = Cl^-, NCS^-, NO_3^-). In acetonitrile solution, the reversible coordination of two solvent molecules in the axial positions of the $[Ni\mathbf{27}]^{2+}$ complex followed the temperature-dependent equilibrium (Equation 16).

$$\left[Ni27(CH_3CN)_2\right]^{2+} \rightleftharpoons [Ni27]^{2+} + 2CH_3CN \qquad (16)$$

Upon heating, the formation of the LS species was favored due to the endothermic character of the HS (six-coordinated octahedral Ni(II)) to LS conversion (four-coordinate quadratic Ni(II)). The increase in the concentration of the LS $[Ni\mathbf{27}]^{2+}$ complex could be followed by the enhancement of the fluorescence intensity of the naphthalene moiety. The quenching of the luminescence in the HS octahedral complex was attributed to a non-radiative energy transfer involving a double electron exchange between the partially filled d orbitals of the Ni(II) center and the molecular orbitals of the photo-excited chromophore (Dexter mechanism) [90]. This pioneering study served as an important proof of concept that the spin-state of a material could be tracked by an appended fluorophore [12].

Garcia and co-workers [68] combined the reversible thermochromic and photochromic properties of the *N*-salicylideneaniline anion [91, 92] with the SCO inducing 1,2,4-triazole motif to make the strongly emitting ligand **28** and the corresponding dinuclear [Fe_2(**28**)$_5$$(NCS)_4$]•4MeOH complex (Figures 27 and 28a). In the crystalline state, a dense supramolecular network of H-bonds and π-π stacking interactions provided a steep cooperative one-step [HS-HS] to [LS-LS] transition with $T_{1/2}$ = 150(1) K. Interestingly, the authors proposed to examine the interplay between the SCO process and the luminescence by monitoring the temperature-dependent shift of the emission maximum of the enol band. Variable-temperature emission spectra revealed a 20 nm bathochromic shift of λ_{max} (from 395 to 415 nm) in the 135–179 K range, which perfectly mirrored the temperature-dependence of the HS mole fraction previously determined by SQUID magnetometry (Figure 28b). However, the evolution of the fluorescence intensity as a function of temperature was not as clear in showing a strong correlation between SCO and luminescence, displaying only a modest discontinuity in the temperature range of the spin transition [68].

As part of their efforts to integrate SCO compounds into functional sp^2-carbon architectures using π-π stacking interactions, Ruben and co-workers [93] designed the ligands **29** and **30**, in which a pyrene substituent is either directly coupled to the 4' position of a bis(pyrazolyl)pyridine ligand or connected through a flexible benzyl butyrate (Figure 27). The SCO behavior of the corresponding Fe(II) complexes differed significantly, with [Fe(**29**)$_2$]$(ClO_4)_2$ remaining trapped in a pure HS configuration while the [Fe(**30**)$_2$]$(X)_2$ complexes exhibited reversible spin-transitions at $T_{1/2}$ = 216 K (X = ClO_4^-) and $T_{1/2}$ = 218 K (X = BF_4^-) with no thermal hysteresis. The strong intermolecular π–π stacking in the crystal lattice of [Fe(**29**)$_2$]$(ClO_4)_2$ indeed led to substantial distortions of the $[Fe^{II}N_6]$ coordination sphere, thereby hindering the structural rearrangements required for the spin-transition to occur. In contrast, the presence of a flexible alkyl

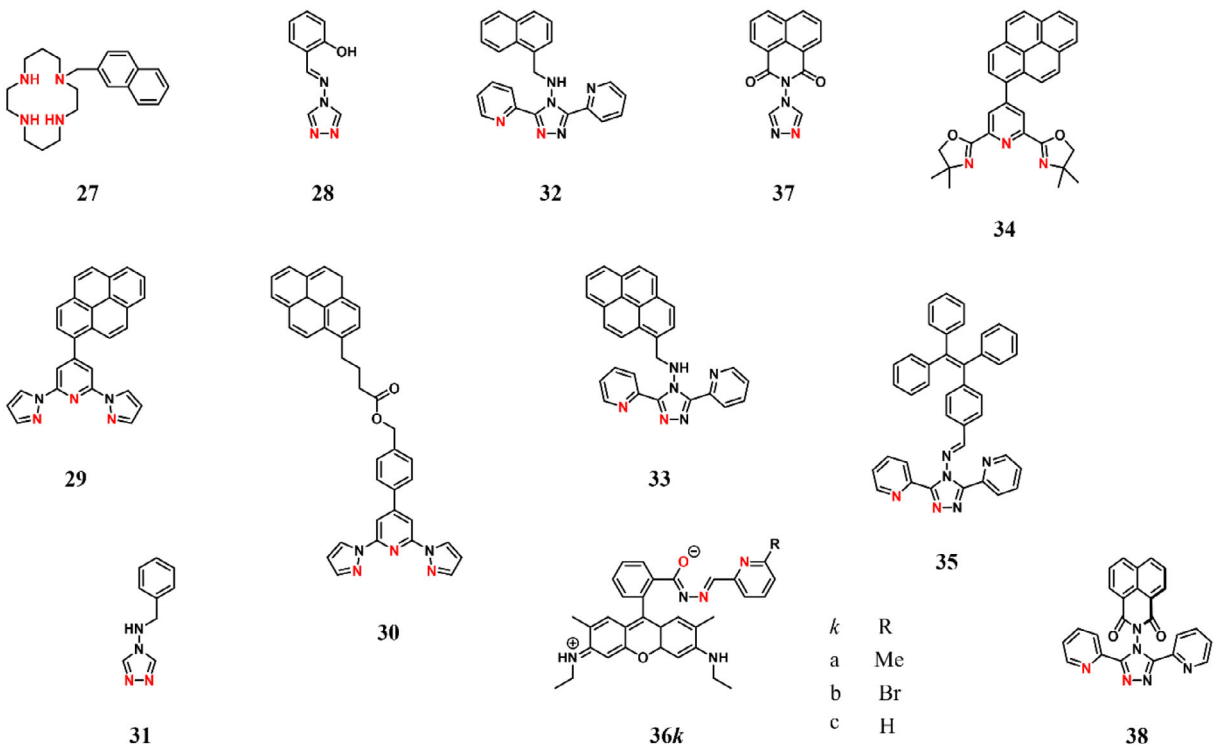

FIGURE 27 | Chemical structures of the ligands **27**–**38** with the donor atoms highlighted in red.

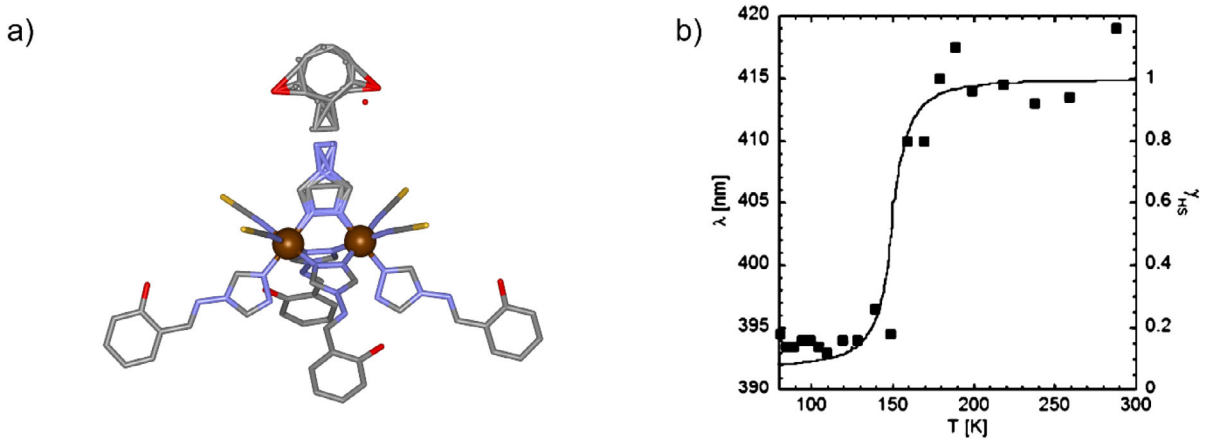

FIGURE 28 | (a) Crystal structure of the dinuclear $[Fe_2(\mathbf{28})_5(NCS)_4]$•4 MeOH complex, and (b) comparison of the temperature-dependence of λ_{max} (black squares) with the mole fractions of HS species derived from the SQUID data (solid line). Reprinted with permission from ref [68]. Copyright 2011 American Chemical Society.

linker in both $[Fe(\mathbf{30})_2](X)_2$ complexes appeared to alleviate this steric strain, enabling the spin-transition to proceed. Variable-temperature emission spectra of $[Fe(\mathbf{30})_2](BF_4)_2$ displayed both the monomer (structured band with vibronic peaks at 373 and 393 nm) and excimer (broad band centered around 460 nm) fluorescence of the pyrene moieties, with a sharp decrease in the excimer intensity upon heating. However, no correlation between the emission intensities and the spin-state of the complex could be evidenced, as the observed temperature-dependence turned out to be typical of pyrene-based fluorophores [93].

Following their report of a one-dimensional luminescent SCO coordination polymer featuring linear Fe(II) 1,2,4-triazole complexes functionalized with organic chromophores and displaying a clear correlation between spin crossover and fluorescence (see Section 4.3) [60], Tao and co-workers [94] investigated the SCO–fluorescence synergy in the structurally analogous model complex $[Fe(\mathbf{31})_2(NCS)_2]$•$4CH_3OH$ previously reported by Roubeau and co-workers [95] (Figure 27). Variable-temperature magnetic measurements revealed a gradual spin-transition, which the authors claimed occurs in a three-step process (Figure 29a). The temperature-dependent emission of the complex seemingly featured three maxima within the 80–95, 125–135, and 145–190 K temperature ranges, which were initially interpreted as directly corresponding to the three-step spin-transition (Figure 29b). However, in a subsequent correction, the authors acknowledged

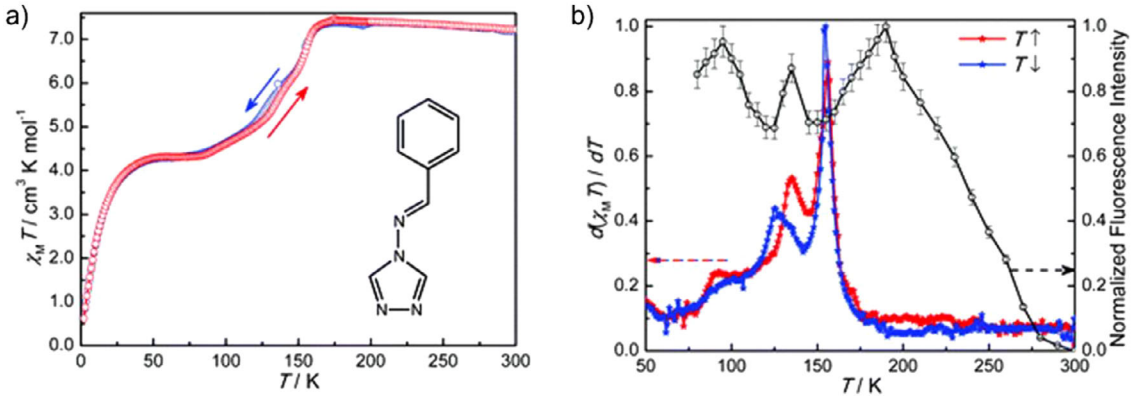

FIGURE 29 | (a) Temperature-dependence of the $\chi_M T$ product of [Fe(**31**)$_2$(NCS)$_2$]•4 CH_3OH, and (b) comparison of the normalized differential magnetic susceptibility with the normalized fluorescence intensity at 497 and 515 nm (l_{exc} = 374 nm) upon heating. Reproduced from ref [96] with permission from the Royal Society of Chemistry.

that the presumed "strong correlation" between SCO and fluorescence was in fact only weakly supported by both experimental and theoretical data [96].

In 2016, Liu and co-workers [97] connected a fluorescent naphthalene moiety to the didentate 4-amino-3,5-bis(pyridin-2-yl)-1,2,4-triazole ligand in an attempt to achieve SCO-luminescence bifunctionality in the corresponding mononuclear [Fe(**32**)$_2$(NCX)$_2$] (X = S, Se) complexes (Figure 27). The nature of the co-ligand had a significant impact on the SCO properties: magnetic susceptibility measurements showed an incomplete spin-transition with $T_{1/2}$ = 74 K for [Fe(**32**)$_2$(NCS)$_2$], while [Fe(**32**)$_2$(NCSe)$_2$] exhibited a complete spin-transition with $T_{1/2}$ = 130 K upon cooling and $T_{1/2}$ = 135 K upon heating. These findings were consistent with (i) the greater ligand-field strength of $NCSe^-$ compared to NCS^-, and (ii) stronger π-π interactions in the crystal lattice of [Fe(**32**)$_2$(NCSe)$_2$], enhancing cooperative effects. Both complexes were emissive and displayed fluorescence bands around 404 (X = S) and 412 nm (X = Se). However, variable-temperature emission spectra showed an unremarkable variation of the luminescence intensity across the whole temperature range, indicating that even though SCO and luminescent properties coexisted in these systems, there was no synergy between the two [97]. Two years later, Liu and co-workers [98] reported the analogous ligand **33,** in which the naphthalene unit was replaced with a pyrene moiety (Figure 27). This modification was intended to enhance the spectral overlap between the emission of the chromophore and the MLCT absorption band of the LS complex, thereby promoting the quenching of the luminescence in the LS state and its recovery in the HS state. Magnetic susceptibility measurements confirmed the SCO behavior of the new [Fe(**33**)$_2$(NCS)$_2$] complex, which exhibited a complete and rather abrupt spin-transition at $T_{1/2}$ = 267 K. The temperature-dependent emission of the complex recorded upon cooling showed (i) an initial drop in the fluorescence intensity between 300 and 250 K followed by a gradual increase down to 10 K, and (ii) a large hypsochromic shift of the emission maximum from λ_{max} = 513 nm at 300 K to λ_{max} = 498 nm at 10 K (Figure 30a). As the fluorescence spectra of the free ligand showed neither discontinuity around the transition temperature nor any spectral shift, the observed modulation was attributed to the interplay between SCO and luminescence (Figure 30b). Another aspect of the SCO-luminescence synergy explored in this study was the modulation of fluorescence intensity by photoinduced spin-transition. Upon irradiation at λ_{exc} = 671 nm, the $\chi_M T$ product of [Fe(**33**)$_2$(NCS)$_2$] increased because of the LIESST effect (a photoinduced spin-transition from the LS to a metastable HS state), generating about 21% of metastable HS-Fe(II). A comparison of the fluorescence intensities recorded at 10 K before and after irradiation at 498 nm returned a 20% increase, which was consistent with the increase in magnetic susceptibility before and after irradiation. Upon subsequent heating, the fluorescent intensity decreased rapidly, reaching its original level at 40 K. This proved that the fluorescence intensity of [Fe(**33**)$_2$(NCS)$_2$] could be increased by light-irradiation and decreased by thermal treatment [98].

In 2021, Liu and co-workers [99] designed the new ligand **34** (Figure 27) based on a pyrene-substituted 2,6-pyridinedioxazole (pybox) motif, which was shown to (i) induce SCO behavior in mononuclear Fe(II) complexes [100, 101], and to (ii) yield highly luminescent metal complexes [102, 103]. Magnetic susceptibility measurements performed on a fresh sample of the [Fe(**34**)$_2$]$(ClO_4)_2$ complex revealed a pure HS configuration, but a gradual and incomplete spin-transition with $T_{1/2}$ = 173 K was observed in the desolvated analog. The solid-state emission spectrum displayed the pyrene fluorescence at 430 nm, as well as a broad band spanning from 450 to 700 nm corresponding to the excimer fluorescence (λ_{exc} = 350 nm). However, variable-temperature emission measurements showed no correlation between luminescence and the SCO process. Instead, a steady increase in emission intensity was observed upon cooling, which was attributed to a reduction in non-radiative relaxation efficiency [99]. The following year, Liu and co-workers [104] pursued a new strategy aimed at (i) enhancing the efficiency of the interaction mechanism to maximize changes in emission intensity, and (ii) addressing self-quenching issues arising from the high concentration of chromophores in the solid state. To achieve these goals, they turned into a family of luminophores known as "Aggregation-Induced Emission luminogens" (AIEgens), which exhibit increased fluorescence intensity in the solid state due to the restriction of molecular motions that deactivate non-radiative relaxation pathways [105–107]. In the context of hybrid luminescent SCO materials, the lengthening of the Fe-N bonds,

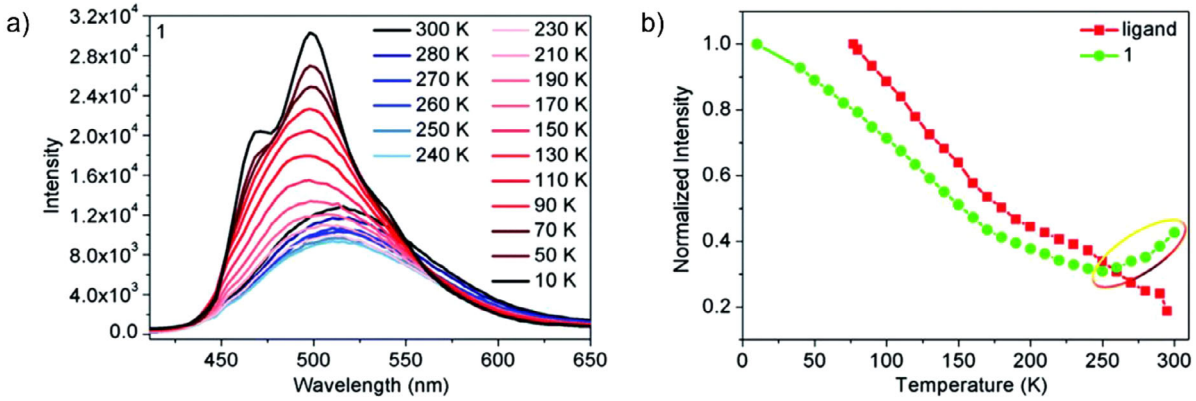

FIGURE 30 | (a) Temperature-dependent emission spectra of $[Fe(\mathbf{33})_2(NCS)_2]$ (λ_{exc} = 380 nm), and (b) normalized fluorescence intensity as a function of temperature for the free ligand **33** (λ_{em} = 516 nm) and the $[Fe(\mathbf{33})_2(NCS)_2]$ complex (λ_{em} = 513 nm between 300 and 170 K and λ_{em} = 498 nm between 160 and 10 K). Reproduced from ref [98] with permission from the Royal Society of Chemistry.

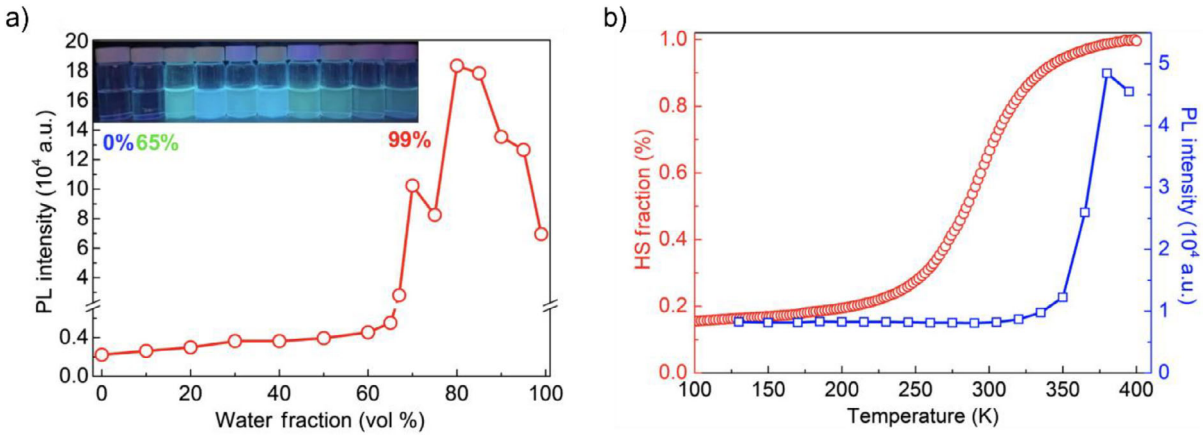

FIGURE 31 | (a) Evolution of the photoluminescence intensity at 484 nm (λ_{exc} = 365 nm) as a function of the water fraction for $[Fe(\mathbf{35})_2(NCSe)_2]$•4DMF, and (b) comparison of the temperature-dependent photoluminescence intensity at 483 nm (λ_{exc} = 365 nm, blue squares) with the HS mole fraction (red circles) of $[Fe(\mathbf{35})_2(NCSe)_2]$•4DMF. Reprinted with permission from ref [104]. Copyright 2022 Chinese Chemical Society.

along with other changes in intermolecular interactions upon the spin-transition, are expected to have a significant impact on the AIEgen emission. They designed the ligand **35** by connecting the tetraphenylethylene AIEgen to the 4-amino-3,5-bis(pyridin-2-yl)-1,2,4-triazole motif (Figure 27). The AIE properties of the corresponding $[Fe(\mathbf{35})_2(NCSe)_2]$•4DMF complex could be confirmed by the striking increase measured in the emission quantum yield, going from 0.3% in pure DMF solutions to 30.9% in 20:80 DMF/H_2O mixtures (Figure 31a). Solid-state magnetic measurements revealed an incomplete spin-transition with $T_{1/2}$ = 295 K. The temperature-dependent emission of the solid complex showed an initial decrease in intensity reaching a minimum at 290 K, followed by an abrupt increase above 330 K, reaching five times the intensity at 380 K compared to 290 K (Figure 31b). Although the decrease in the intensity of the broad $^1A_1 \rightarrow {}^1T_1$ d-d transition (450–600 nm) in the 290–380 K range pointed at a FRET mechanism, the observed emission enhancement appeared to exceed what could be explained by absorption changes alone. Further investigations suggested that weakened intermolecular interactions following the spin-transition also contributed by limiting the non-radiative deactivation of the AIEgens [104].

Kou and co-workers [108] designed the ligand **36a** by combining the pyridyl(aroylhydrazone) motif, the iron(II) complex of which displayed abrupt spin-transition around R*T* [109], with a fluorescent rhodamine 6G derivative characterized by (i) high quantum yield and photostability, (ii) visible light excitation, (iii) long wavelength emission, and (iv) switchable fluorescence modulated by the pH of the solution or by the coordination of a Lewis-base metal ion (Figure 27) [110]. Magnetic susceptibility measurements performed on the $[Fe(\mathbf{36a})_2](ClO_4)_2$ complex revealed a peculiar three-step spin-transition with inflection points at 240, 160, and 100 K, corresponding to HS-Fe(II) populations of 93%, 71%, and 25% respectively. In contrast, the desolvated complex exhibited an abrupt one-step spin-transition, with a wide hysteresis loop of 40 K ($T_{1/2}$ = 303 K upon cooling and 343 K upon warming). Even though the overall luminescence response was weak, variable-temperature emission spectra of the desolvated complex displayed the expected thermal quenching of the rhodamine emission band at 560 nm from 250 to 300 K, followed by an increase in fluorescence intensity in the spin-transition region (300–350 K), and a return to the initial quenching trend above 350 K (Figure 32a,b). The synergy between the SCO process and the luminescent properties was supported

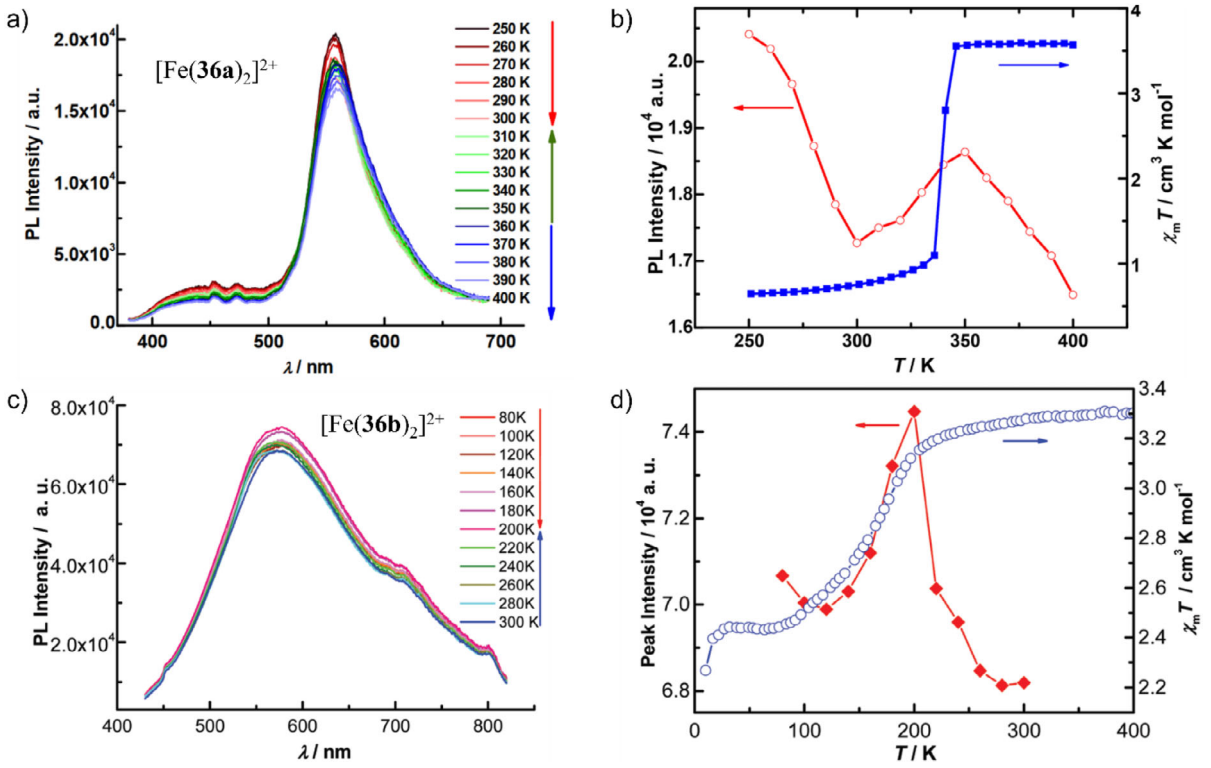

FIGURE 32 | Temperature-dependent emission spectra (λ_{exc} = 355 nm) of (a) [Fe(**36a**)$_2$](ClO$_4$)$_2$ and (c) [Fe(**36b**)$_2$](ClO$_4$)$_2$, and comparison of the temperature-dependent fluorescence intensity with the $\chi_M T$ product of (b) [Fe(**36a**)$_2$](ClO$_4$)$_2$ (λ_{em} = 560 nm), and (d) [Fe(**36b**)$_2$](ClO$_4$)$_2$ (λ_{em} = 570 nm). The top panel was adapted with permission from ref [108]; Copyright 2018 American Chemical Society, while the bottom panel was adapted from ref [111] with permission from the Royal Society of Chemistry.

by the reproducibility of this behavior upon both cooling and warming, as well as by the absence of such discontinuity in the temperature-dependent emission of the analogous Zn(II) complex. DFT calculations attributed the enhanced fluorescence in the HS state to a reduced spectral overlap between the fluorophore emission and the absorption bands of the HS complex [108].

In a subsequent study, Kou and co-workers [111] further investigated the effect of substituents on both the SCO behavior and the SCO-luminescence synergy by synthesizing the 6-bromo and 6-hydro derivatives of their previous ligand (**36b** and **36c,** respectively, Figure 27). However, the corresponding [Fe(**36b**)$_2$](ClO$_4$)$_2$ and [Fe(**36c**)$_2$](ClO$_4$)$_2$ complexes exhibited pure HS and pure LS configurations, respectively. Upon desolvation, the [Fe(**36b**)$_2$](ClO$_4$)$_2$ complex underwent an incomplete spin-transition over the 230–70 K temperature range. The temperature-dependent emission of the desolvated [Fe(**36b**)$_2$](ClO$_4$)$_2$ complex mirrored that of [Fe(**36a**)$_2$](ClO$_4$)$_2$, showing a discontinuity in the thermal quenching of the luminescence between 120 and 200 K (Figures 32c,d) [111].

As opposed to all the previous examples of mononuclear luminescent SCO complexes, which mostly consisted of bis-tridentate ML$_2$ coordination systems, Boukheddaden and co-workers [112] reported the first SCO Fe(II) complex featuring six monodentate phosphorescent ligands **37** (Figure 27). The thermal variation of the magnetic susceptibility of [Fe(**37**)$_6$]X$_2$•4CH$_3$CN (where X = 1,1,3,3-tetracyano-2-thiomethylpropenide) showed a gradual and nearly complete spin-transition with $T_{1/2}$ = 114 K. Compared to the emission of the free ligand **37**, which displayed two bands centered around 486 and 412 nm, the [Fe(**37**)$_6$]X$_2$•4CH$_3$CN complex exhibited two additional bands at 600 and 445 nm (λ_{exc} = 325 nm). Using a similar approach as Garcia et al. [68], the authors were able to correlate the thermal evolution of the HS mole fraction, derived from magnetic measurements, with the temperature-dependent shift of the low-energy band (600 nm). However, in line with the findings of Garcia and co-workers [68], the temperature-dependence of the total integrated emission did not show a clear correlation between the SCO process and the luminescence, as no abrupt change was observed in the range of the spin-transition [112].

Finally, Xue and co-workers [113] reported ligand **38** combining the well-known naphthalimide fluorophore with the classical 4-amino-3,5-bis(pyridin-2-yl)-1,2,4-triazole motif (Figure 27). Solid-state magnetic susceptibility measurements performed on the associated [Fe(**38**)$_2$(NCS)$_2$]•2DMF complex displayed an abrupt one-step spin-transition with $T_{1/2}$ = 189(1) K. Interestingly, the two emission bands of the complex (390 and 408 nm) exhibited distinct temperature-dependent behaviors: the band at 390 nm was unaffected by the spin transition and showed a typical monotonous decrease, whereas the band at 408 nm increased around the transition temperature (Figures 33a,b). Consequently, [Fe(**38**)$_2$(NCS)$_2$]·2DMF functioned as a ratiometric fluorescence thermometer, in which the intensity of the higher-energy band (I_{390nm}) served as an internal reference, and that of the lower-energy band (I_{408nm}) followed the SCO process (Figure 33c). This

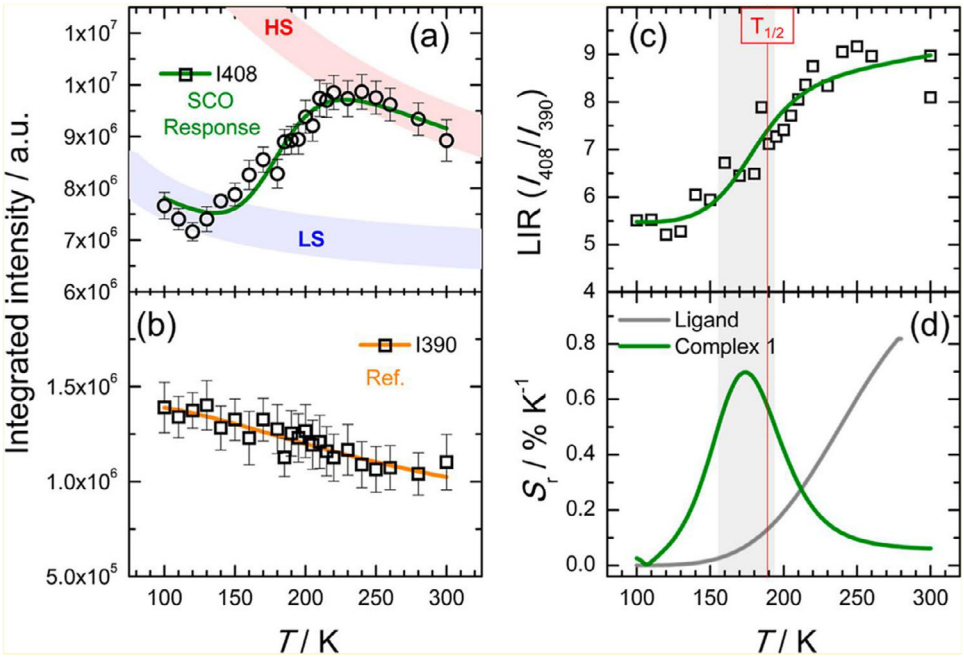

FIGURE 33 | Temperature-dependent evolution of (a) the integrated intensity of the low-energy band (I_{408nm}), (b) the integrated intensity of the high-energy band (I_{390nm}), (c) the luminescence intensity ratio LIR = I_{408nm}/ I_{390nm}, and (d) the acquired relative temperature sensitivity S_r = dln(LIR)/dT. Reprinted with permission from ref [113]. Copyright 2023 American Chemical Society.

system thus represents the first SCO-based thermometer employing ratiometric fluorescence with high sensitivity performance (Figure 33d) [113].

5.3 | d-Block Luminophores

Luminescent transition metal complexes are far less commonly employed than organic chromophores for monitoring spin-state equilibria. A key limitation lies in the poor emissive properties of first-row metal ions due to the primogenic effect: [114] the absence of radial nodes away from the nucleus for the $n - l = 1$ wave functions (where n and l are the principal and azimuthal quantum numbers, respectively) leads to an inefficient shielding of the nuclear charge by the core electrons, causing the electronic distribution of 3d valence shells to remain relatively compact [22, 115]. This results in limited spatial overlaps with the orbitals of the donor atoms, which generates considerably weaker ligand fields than those observed with 4d or 5d metal ions. Consequently, 3d metal complexes typically display a dense manifold of MC excited states that lie close in energy to one another and to the electronic ground state, which greatly favors non-radiative relaxation processes. In contrast, the stronger ligand fields associated with 4d and 5d metal complexes lead to larger energy separations between individual MC states and between the lowest MC state and the ground state. This enhances the rate of radiative relaxation and promotes interactions with the molecular orbitals of the ligands, giving rise to metal-to-ligand (MLCT) and ligand-to-metal (LMCT) charge-transfer states with desirable photophysical properties [116]. As a result, efficient radiative processes are mostly restricted to complexes of rare and precious third-row transition metals, making them a less appealing alternative to cost-effective organic luminophores, which offer greater synthetic versatility. Nevertheless, two examples of heterometallic d–d′ complexes combining SCO behavior with luminescence have been reported.

As part of their work on Ni(II) complexes, Weber and co-workers [117] designed the two back-to-back ligands **39** and **40**, capable of binding a phosphorescent [Ru(bipy)$_2$Cl$_2$] (bipy = 2,2'-bipyridine) unit and a switchable Ni(II) center at varying lengths, to examine the potential photoluminescence quenching of the associated complexes upon CISSS (Figure 34). The occurrence of CISSS in the [Ni(**39**)Ru(bipy)$_2$](PF$_6$)$_2$ and [Ni(**40**)Ru(bipy)$_2$](PF$_6$)$_2$ complexes was confirmed by the significant changes observed in their absorption spectra upon addition of pyridine. The emission spectra of both complexes in acetonitrile featured single, broad emission bands consistent with the radiative decay of Ru-to-ligand MLCT excited states. However, fluorescence measurements performed on pyridine solutions revealed vastly different photophysical properties: both the fluorescence intensity and luminescence lifetime of [Ni(**39**)Ru(bipy)$_2$](PF$_6$)$_2$ were enhanced, while a pronounced quenching of the emission intensity of [Ni(**40**)Ru(bipy)$_2$](PF$_6$)$_2$ was observed. As a comparable twofold increase in emission intensity was also measured for the analogous mononuclear [Ru(**39**)(bipy)$_2$](PF$_6$)$_2$ complex in pyridine, the enhancement in [Ni(**39**)Ru(bipy)$_2$](PF$_6$)$_2$ was tentatively assigned to the larger dielectric constant of pyridine relative to acetonitrile. Conversely, the 20-fold reduction in the emission intensity of [Ni(**40**)Ru(bipy)$_2$](PF$_6$)$_2$ clearly pointed toward CISSS-induced luminescence quenching. Structural analyses revealed that in [Ni(**39**)Ru(bipy)$_2$](PF$_6$)$_2$, where the Ru-Ni distance is shorter, steric hindrance between protons prevents the conjugation of the Ni(II) center with the emissive unit. In contrast, in the extended [Ni(**40**)Ru(bipy)$_2$](PF$_6$)$_2$ complex, the bridging phenazine moiety enables the electronic coupling of the two metal centers within the same π-conjugated system. With these considerations in mind, and taking the limited spectral

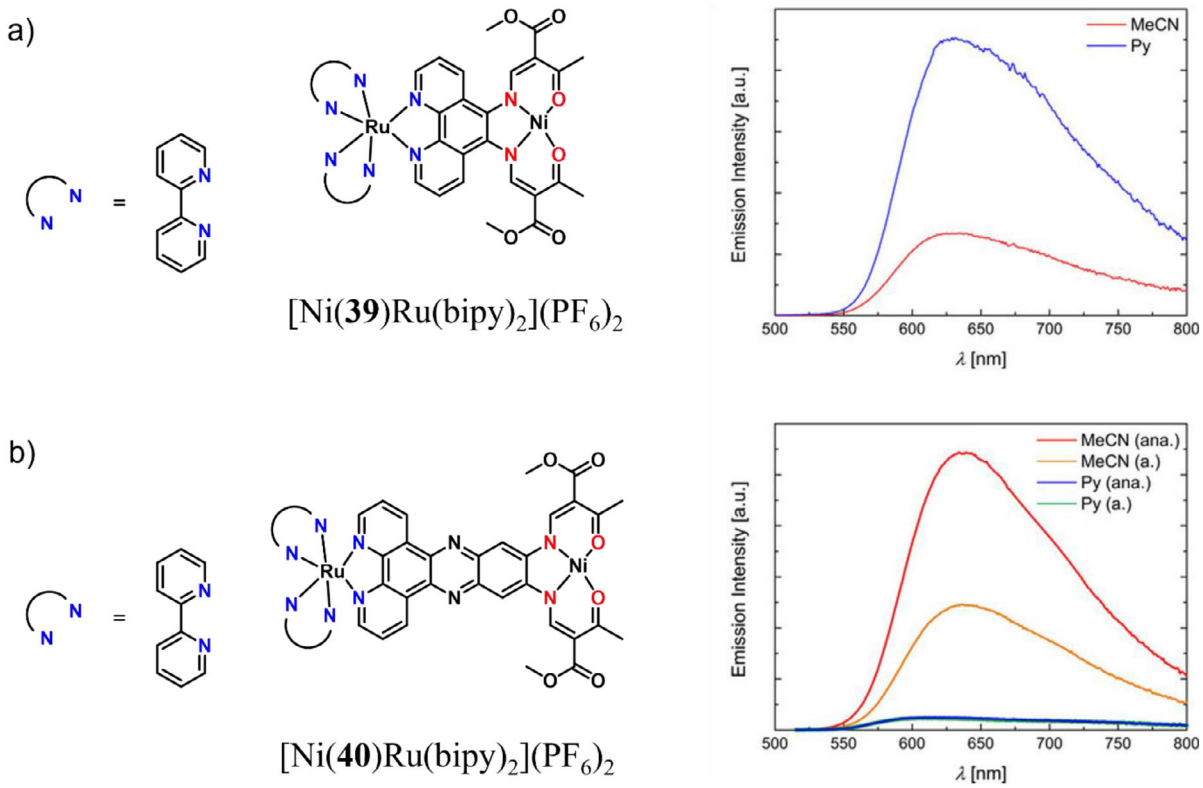

FIGURE 34 | Chemical structure and corresponding emission spectra in acetonitrile and in pyridine of (a) [Ni(**38**)Ru(bipy)$_2$](PF$_6$)$_2$, and (b) [Ni(**39**)Ru(bipy)$_2$](PF$_6$)$_2$. a = aerobic and ana = anaerobic atmospheres. Reprinted with permission from ref [117]. Copyright 2018 Wiley-VCH.

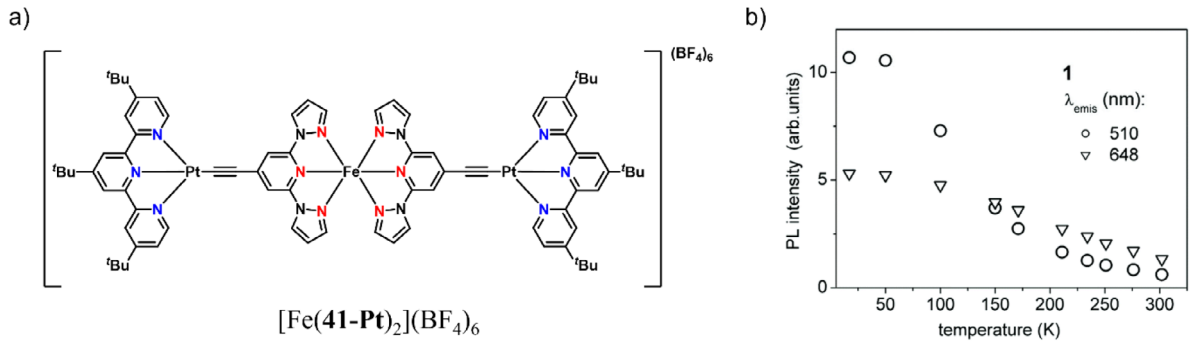

FIGURE 35 | (a) Chemical structure of the heterotrimetallic [Fe(**41**-Pt)$_2$](BF$_4$)$_6$ complex, and (b) temperature-dependence of the normalized photoluminescence intensities at 510 (circles) and 648 nm (triangles). Reproduced from ref [118] with permission from the Royal Society of Chemistry.

overlap between emission and absorption bands into account, the authors proposed that the luminescence quenching observed in [Ni(**40**)Ru(bipy)$_2$](PF$_6$)$_2$ proceeded via a Dexter mechanism [117].

Ruben and co-workers [118] designed the back-to-back ditopic bridging ligand **41** by substituting the 4-position of the SCO-inducing 2,6-bis(pyrazolyl-1-yl)pyridine backbone with an ethynyl-coordinated [Pt(tbtpy)$_2$](BF$_4$) (tbtpy = 4,4,4-tri-tert-butyl-2,2:6,2-terpyridine) unit known for its luminescent properties (Figure 35a). Intriguingly, slow-evaporation of a dichloromethane solution of the resulting trimetallic complex provided two types of crystals, which differed by the number of solvent molecules in the lattice and the spin-state of the Fe(II). Although the two types of crystal could not be separated and studied individually, ^{57}Fe Mössbauer spectroscopy revealed that the two [Fe(**41**-Pt)$_2$](BF$_4$)$_2$·3.5CH$_2$Cl$_2$ and [Fe(**41**-Pt)$_2$](BF$_4$)$_2$·10CH$_2$Cl$_2$ species were present in a 1:1 ratio, with the former being trapped in the HS state whereas the latter underwent reversible thermal SCO with $T_{1/2}$ = 268 K. The solid-state emission spectra of the free ligand and the complex were relatively similar, with a vibronically-resolved band between 500 and 600 nm and a broader feature around 650 nm attributed to the monomer and excimer phosphorescence of the Pt(II) units, respectively. Both the intensity and lifetime were temperature-dependent, with no apparent correlation with the SCO behavior (Figure 35b). Femtosecond-transient absorption spectroscopy suggested that an energy transfer from the excited Pt(II) to the Fe(II) did occur and might contribute to the quenching of the Pt-centered luminescence in solution, ideally modulated by the spin-state of Fe(II). However, the data previously collected in

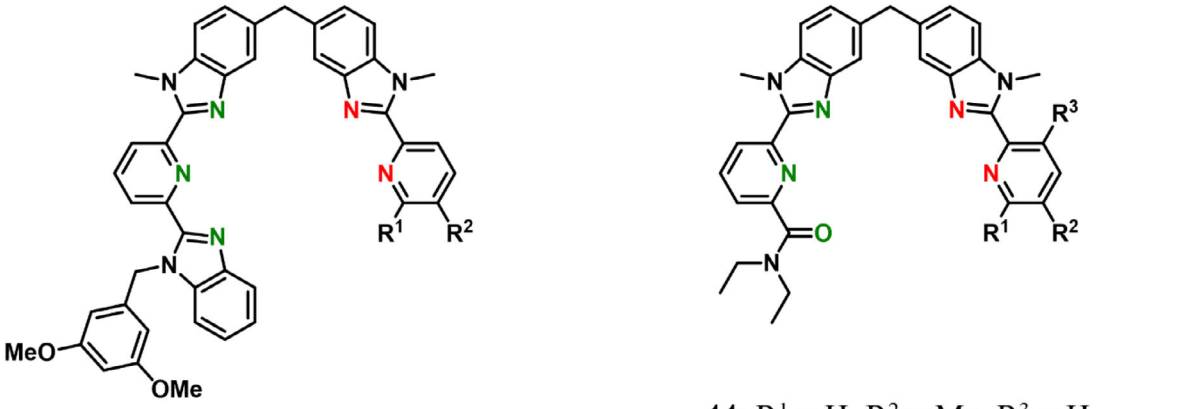

42: $R^1 = Me$, $R^2 = H$

43: $R^1 = H$, $R^2 = Me$

44: $R^1 = H$, $R^2 = Me$, $R^3 = H$

45: $R^1 = H$, $R^2 = SO_2(NEt_2)$, $R^3 = H$

46: $R^1 = Me$, $R^2 = H$, $R^3 = H$

47: $R^1 = H$, $R^2 = H$, $R^3 = Me$

FIGURE 36 | Chemical structures of the ligands **42**–**47**, highlighting the donor atoms of the didentate binding sites in red and of the tridentate binding sites in green.

both solution and solid states showed that this process, if present, was small and became negligible compared to the thermal quenching of the phosphorescence [118].

5.4 | f-Block Luminophores

The remarkable luminescent properties of trivalent lanthanide ions Ln(III), which have found widespread use across various fields [119–121], appear well-suited for monitoring spin-state changes in SCO complexes. The origin of their distinctive atom-like properties can also be traced back to the primogenic effect—ironically the same effect that turned 3d metal ions into notorious "luminescence killers" [12]. The higher charge of lanthanide nuclei significantly restricts the radial expansion of the $4f^n$ valence shells, effectively shielding them from external perturbations by the filled 5s2 and $5p^6$ orbitals. This shielding results in negligible ligand-field effects, allowing lanthanide ions to preserve their atomic-like electronic structure in coordination complexes [22]. As a result, they exhibit advantageous optical features such as line-like emission, long-lived excited states, small Stokes shifts, and excellent photostability [53]. The latter is particularly appealing for luminescent SCO materials, given that photobleaching and the associated irreversible signal loss are one of the main drawbacks of organic chromophores [53]. However, the parity-forbidden character of the intra-configurational f-f transitions may become a concern if the interaction goes through a radiative energy transfer, as the inefficient reabsorption process would yield a very small modulation of the luminescence intensity. To the best of our knowledge, the only reported attempts at designing molecular heterometallic d–f assemblies combining a SCO center with a luminescent trivalent lanthanide ion have been made by Piguet and co-workers [22, 34, 122–128]. Throughout the years, they have designed a series of heteroleptic ligands containing various didentate and tridentate binding sites coded for the simultaneous recognition of 3d and 4f metal ions (Figure 36) [34, 122, 124–126]. Upon complexation with a 1:1 mixture of $Fe(X)_2$ and $Eu(X)_3$ ($X = ClO_4^-$, $CF_3SO_3^-$), these segmental ligands readily self-assemble into the corresponding C_3-symmetrical heterodimetallic triple-stranded helicates $[FeEu(\boldsymbol{k})_3](X)_5$ (***k*** **= 42–47**). In these complexes, the SCO Fe(II) functions as a versatile energy acceptor for the variable quenching of the Eu(III)-centered emission in the non-radiative Eu(III)→Fe(II) energy transfer. Owing to the distinct absorption profiles associated with each spin-state, and their respective spectral overlap with the Eu(III) emission bands, the efficiency of intermetallic communication is expected to be strongly dependent on the spin-state of the Fe(II). As a result, the Eu(III) ion may serve as an optical readout of the magnetic state of the complex [12, 126].

In 1995, Piguet and co-workers [122] investigated the temperature-dependent magnetic properties of a series of $[FeLn(\mathbf{43})_3](ClO_4)_5$ (Ln = La, Ce, Pr, Nd, Sm, Eu) complexes in acetonitrile, which all displayed gradual spin-transitions with critical temperatures comprised between 350 and 369 K ($T_{1/2}$ = 359 K for Ln = Eu). Upon UV excitation, the emission spectrum of the $[FeLa(\mathbf{43})_3](ClO_4)_5$ helicate only showed very weak luminescence from the ligand, suggesting a possible mixing of the MLCT state with the triplet state of the ligand. Replacing La(III) with Eu(III) further diminished the ligand-centered emission, yet no emission from the Eu($^5D_0$) state could be detected. This implied that the sensitization of the Eu(III) did occur, but the resulting luminescence was quantitatively quenched by the Fe(II)-based MLCT state [122]. In the same year, they reported the new ligand **44**, in which the terminal benzimidazole group was replaced by an *N*,*N*'-diethylcarboxamido moiety, resulting in strongly luminescent heterodimetallic d-f helicates (Figure 36) [123]. Variable-temperature magnetic measurements performed on a similar series of $[FeLn(\mathbf{44})_3](ClO_4)_5$ complexes (Ln = La, Nd, Eu, Y, Yb, Lu) confirmed the SCO behavior, with slightly smaller transition temperatures comprised between 331 and 349 K ($T_{1/2}$ = 336 K for Ln = Eu). Despite the increased luminescence of **44**

compared to **43**, the emission spectra of $[FeLa(\mathbf{44})_3](ClO_4)_5$ and $[FeEu(\mathbf{44})_3](ClO_4)_5$ displayed a similar quenching of the ligand-centered emission by the MLCT state, as well as no detectable Eu(III)-centered emission [124].

Considering that the efficient quenching of the Eu(III)-centered luminescence by the MLCT state of the LS species, even at high temperature where the mole fraction of HS-Fe(II) was the highest possible ($x_{HS} > 0.5$), prevented the investigation of the intramolecular Eu(III)→Fe(II) energy transfer, Piguet and co-workers sought to prepare a pure HS complex in hopes of restoring sufficient Eu(III)-centered emission to study the intermetallic communication [126]. With this new goal in mind, they designed ligand **45** by connecting an electron-withdrawing sulfonamide group at the 5-position of the pyridine ring of the didentate binding unit in order to reduce the ligand-field strength of the $[Fe^{II}N_6]$ unit (Figure 36) [125]. However, the decreased σ-donating ability of the pyridine lone pair was compensated by an increase in the π-accepting properties of the didentate binding unit in the corresponding $[FeLn(\mathbf{45})_3](ClO_4)_5$ (Ln = La, Y, Lu) complexes. Consequently, the transition temperature decreased by only 20 K, hence maintaining the SCO behavior of the heterodimetallic helicates [125]. In a subsequent study, Piguet and co-workers [126] followed an alternative approach whereby the transfer of the methyl group from the 5 to the 6-position of the pyridine ring in **46** sterically hindered the contraction of the Fe-N bonds required for the formation of the LS species. Temperature-dependent magnetic measurements performed on the $[FeLa(\mathbf{46})_3](ClO_4)_5{\bullet}2H_2O{\bullet}1.5CH_3CN$ complex confirmed the pure HS configuration in the solid state and in acetonitrile solutions. Subsequent excitation of the $\pi^*{\leftarrow}\pi$ band of $[FeEu(\mathbf{46})_3](ClO_4)_5$ yielded weak, but detectable Eu-centered luminescence (Figure 37b). Despite the weaker and broader appearance of the $^5D_0{\rightarrow}^7F_J$ (J = 1–4) transitions in comparison with the analogous $[ZnEu(\mathbf{46})_3](ClO_4)_5$ helicate, the splitting of the ^7F_J levels and the relative integrated intensity ratios remained comparable, suggesting that the Eu(III) coordination spheres remained similar in both complexes (Figure 37b). Lifetime measurements revealed a 9.5 fold reduction from 2.63(1) ms in $[ZnEu(\mathbf{46})_3](ClO_4)_5$ to 0.277(7) ms in $[FeEu(\mathbf{46})_3](ClO_4)_5$, which was attributed to the non-radiative Eu(III)→HS-Fe(II) energy transfer. Given that (i) no orbitally mediated communication could be evidenced between the two metal centers, and (ii) the concomitant blue-shift of the MLCT band and red-shift of the d-d transitions in the absorption spectrum of $[FeEu(\mathbf{46})_3](ClO_4)_5$ significantly reduced the spectral overlap with the Eu(III)-centered emission (Figures 37c,d), the authors concluded that the energy transfer relied on a Förster mechanism [126].

In 2020, Piguet and co-workers [34] reported a detailed kinetic analysis aimed at deciphering the intramolecular Eu(III)→Fe(II) communication operating in $[FeEu(\boldsymbol{k})_3](CF_3SO_3)_5$ (**k** = **44**, **46**, **47**) triple-stranded helicates in a quantitative manner. Taking full advantage of the self-assembly process, which enabled the incorporation of various M(II)/Ln(III) pairs within the different (supra)molecular $[MLn(\boldsymbol{k})_3](CF_3SO_3)_5$ (**k** = **44**, **46**, **47**) complexes without altering their structures, they were able to estimate the various rate constants associated with the spin-state equilibrium (k_{LH} and k_{HL}), the radiative and non-radiative relaxations (k_{Eu}^{relax}), and ultimately the intramolecular Eu(III)-to-Fe(II) quenching processes (k_{LS}^{q} and k_{HS}^{q}, Figure 38a). With quenching efficiencies approaching 100% for the LS configuration and exceeding 95% for the HS state, this study demonstrated that the spectral overlap integral for the LS-Fe(II)/Eu(III) pair was so large that trace amounts of the former were sufficient to drastically quench the emission of the latter (Figure 38b) [34].

To overcome this limitation and restore detectable lanthanide-based luminescence, three strategies were investigated. The first one aimed at maximizing the mole fraction of weakly absorbing HS species at temperatures accessible in solution by shifting the transition temperature $T_{1/2}$ toward lower values via a judicious modification of the didentate chelating unit bound to Fe(II). Due to the current lack of methodology for reliably fine-tuning the SCO properties of a $[Fe^{II}N_6]$ unit [129], Piguet and co-workers resorted to the systematic exploration of the magnetic properties of a series of structurally related mononuclear $[Fe(\boldsymbol{k})_3]^{2+}$ (**k** = **48–54**) complexes modeling the didentate binding site of the corresponding d-f $[FeLn(\boldsymbol{k})_3]^{5+}$ (**k** = **44**, **46**, **47**, **55**) triple-stranded helicates with various σ-donating/π-accepting abilities and specific steric constraints (Table 1) [21, 23, 130].

As previously evidenced in the $[FeLn(\mathbf{46})_3]^{5+}$ helicate [126], moving the methyl group from the 5-position in **48** to the 6-position in **50** and to the 3-position in **49** and **52** greatly reduced the ligand-field strength in the associated $[Fe(\boldsymbol{k})_3]^{2+}$ (**k** = **48**, **49**, **52**) complexes because the increased inter- and intra-strand interactions sterically hindered the contraction of the Fe-N bonds, and thus favored pure HS configurations at RT (Table 1) [23, 130]. Replacing the pyridine ring in **48** by a strong π-accepting pyrazine unit in **51** increased the strength of the Fe-N bonds, which logically stabilized the LS state and resulted in a 40 K shift of the transition temperature toward higher values (Table 1) [23]. In contrast, the pyrimidine-containing ligands **53** and **54** displayed the weakest enthalpic changes accompanying the spin transition of the series (Table 1) [21]. Due to the partial positive enthalpy/entropy compensation established for SCO processes [131], the reduction of ΔH_{SCO} was coupled to a reduction of ΔS_{SCO}, and the lowest transition temperature was therefore found in $[Fe(\mathbf{53})_3]^{2+}$, which displayed the smallest SCO entropy changes. It should be noted here that the thermodynamic parameters recorded for $[Fe(\boldsymbol{k})_3]^{2+}$ (**k** = **48–54**) complexes correspond to average values characterizing a mixture of temperature-dependent *mer*/*fac* isomers [23], whereas the three didentate units in each heterodimetallic $[FeLn(\boldsymbol{k})_3]^{5+}$ (**k** = **44**, **46**, **47**, **55**, **56**) helicate adopt a pure facial coordination around the d-metal [132]. Combining the thermodynamic data associated with the *mer*↔*fac* isomerization process and the magnetic susceptibilities recorded for standard solution mixtures provided the specific contributions of the co-existing *fac*-$[Fe(\mathbf{53})_3]^{2+}$ and *mer*-$[Fe(\mathbf{53})_3]^{2+}$ isomers, with $T_{1/2}$ = 309(23) K for the former and $T_{1/2}$ = 258(21) K for the latter [21]. The difference between the two was attributed to a rare example of H/S anti-compensation whereby (i) the stabilizing *trans*-influence, known to strengthen Fe-N bonds in facial isomers, increased the enthalpic cost, while (ii) the greater dipolar contribution to the solvation energy in *fac*-$[Fe(\mathbf{53})_3]^{2+}$ reduced the entropic gain [21]. With this promising candidate at hand, Piguet and co-workers proceeded to replace the terminal pyridine ring in **44** with a 2-pyrimidine analog [127]. Despite considerable difficulties that required shifting the connection of the hydrolysis-sensitive pyrimidine to the diphenylmethane spacer to the last synthetic steps, the desired heteroleptic ligand **55** (Figure 39)

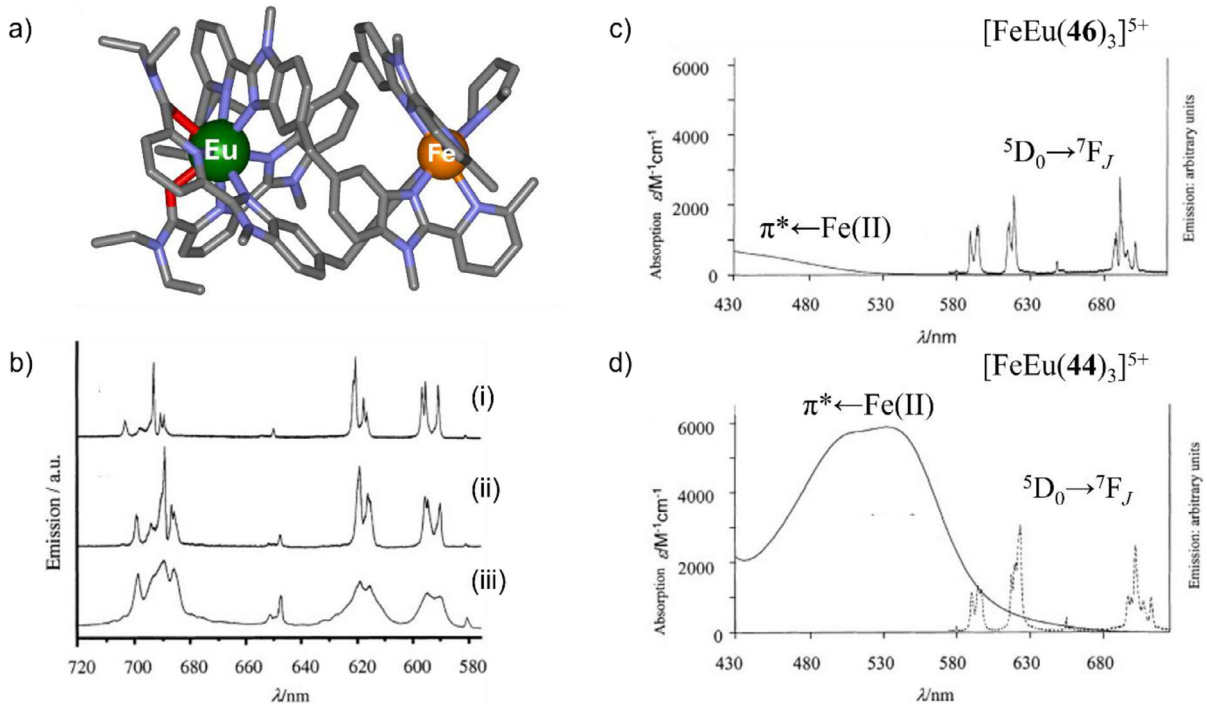

FIGURE 37 | Left panel: (a) crystal structure of $[FeEu(\mathbf{46})_3](CF_3SO_3)_5{\bullet}2CH_3CN{\bullet}1.5C_5H_{12}O$, and (b) solid-state emission spectra of (i) $[ZnEu(\mathbf{46})_3](ClO_4)_5{\bullet}H_2O$ at 13 K (λ_{exc} = 378 nm) and $[FeEu(\mathbf{46})_3](ClO_4)_5{\bullet}H_2O$ (λ_{exc} = 308 nm) at (ii) 13 K and (iii) 295 K; right panel: comparison between the absorption (acetonitrile, 298 K) and emission spectra (solid state, 13 K) of (c) the pure HS $[FeEu(\mathbf{46})_3]^{5+}$ complex, and (d) the SCO $[FeEu(\mathbf{44})_3]^{5+}$ helicate (as no emission could be detected for the latter, the dashed lines represent the $^5D_0 \rightarrow {}^7F_J$ transitions of the Zn(II) analog). Adapted with permission from ref [126]. Copyright 2001 Wiley-VCH.

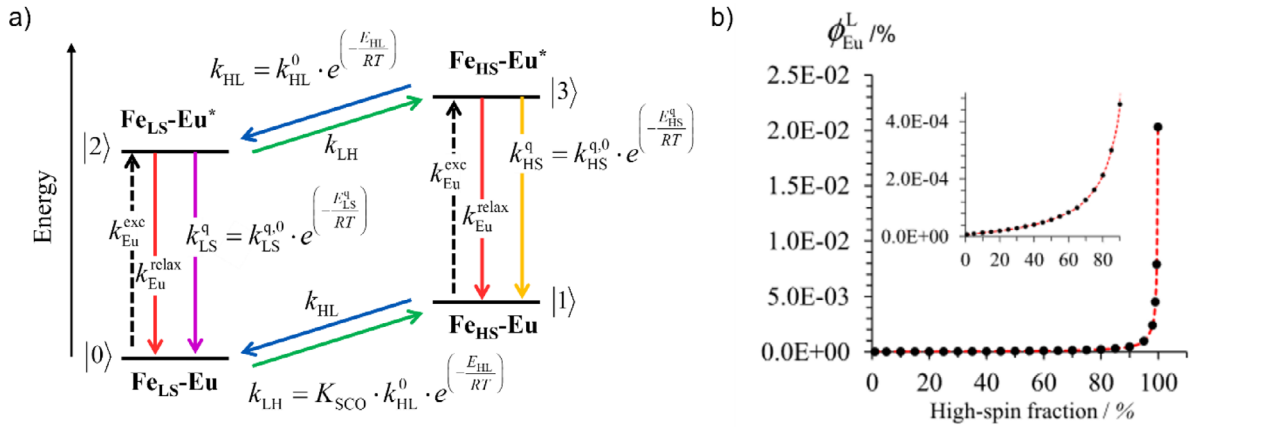

FIGURE 38 | (a) Kinetic scheme for the Eu(III)-based luminescence monitoring of the Fe(II) spin-state equilibrium the dinuclear $[FeEu(\mathbf{44})_3](CF_3SO_3)_5$ complex, and (b) global quantum yields computed for $[FeEu(\mathbf{44})_3]^{5+}$ in acetonitrile as a function of the mole fraction of HS-Fe(II). Reprinted with permission from ref [34]. Copyright 2020 American Chemical Society.

and the corresponding dimetallic $[MLn(\mathbf{55})_3](CF_3SO_3)_5$ complexes (M = Zn, Fe; Ln = La, Eu, Nd) could be eventually obtained [127]. Variable-temperature magnetic measurements subsequently confirmed the expected downward trend of the transition temperature in the $[FeLn(\mathbf{55})_3](CF_3SO_3)_5$ helicates, with $T_{1/2}$ = 317(1) K for $[FeEu(\mathbf{55})_3]^{5+}$ < $T_{1/2}$ = 344 K for $[FeEu(\mathbf{44})_3]^{5+}$ (Figure 39a). Another consequence of the introduction of the 2-pyrimidine in **55** was the unforeseen yet favorable reduction in the intensity of the MLCT absorption band observed in both LS-$[FeLa(\mathbf{55})_3]^{5+}$ and HS-$[FeLa(\mathbf{55})_3]^{5+}$ (Figure 39b). The combination of these two elements was sufficient to restore detectable red Eu($^5D_0 \rightarrow {}^7F_J$) emission in the 233–333 K range (λ_{exc} = 333 nm), thereby providing the first experimental demonstration of SCO-modulated Ln(III)→Fe(II) communication operating in single molecules in solution (Figure 39c) [127].

Using the kinetic model shown in Figure 38a, Piguet and coworkers were able to decipher the contributions of the various rate constants to the temperature-dependent evolution of the

TABLE 1 | Chemical structures of didentate ligands **48**–**54** and associated thermodynamic SCO properties of the corresponding pseudo-octahedral $[Fe(\boldsymbol{k})_3]^{2+}$ complexes (*mer* + *fac* mixtures) in CD_3CN solutions.

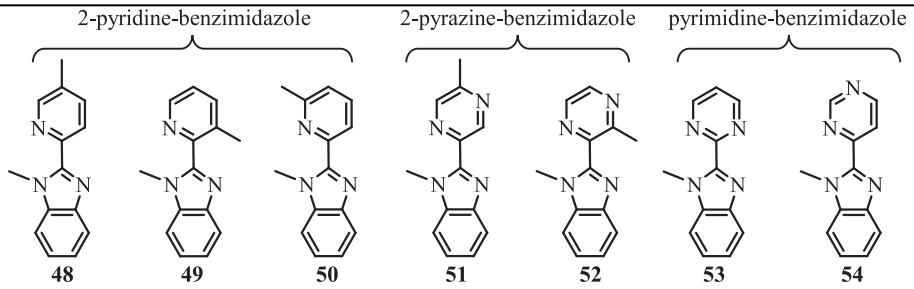

Complex	$[Fe(\mathbf{48})_3]^{2+}$	$[Fe(\mathbf{49})_3]^{2+}$	$[Fe(\mathbf{50})_3]^{2+}$	$[Fe(\mathbf{51})_3]^{2+}$	$[Fe(\mathbf{52})_3]^{2+}$	$[Fe(\mathbf{53})_3]^{2+}$	$[Fe(\mathbf{54})_3]^{2+}$
ΔH_{SCO} / kJ·mol^{-1}	28.3(4)	High-spin	High-spin	35.0(3)	High-spin	19.5(2)	23.0(2)
ΔS_{SCO} / J·mol^{-1}·K^{-1}	91(1)	High-spin	High-spin	100(1)	High-spin	71.3(6)	82.5(8)
$T_{1/2}$ /K	309(6)	High-spin	High-spin	349(5)	High-spin	273(3)	279(1)
Reference	[23]	[23]	[23]	[23]	[]	[21]	[21]

Adapted from ref [21] with permission from the Royal Society of Chemistry.

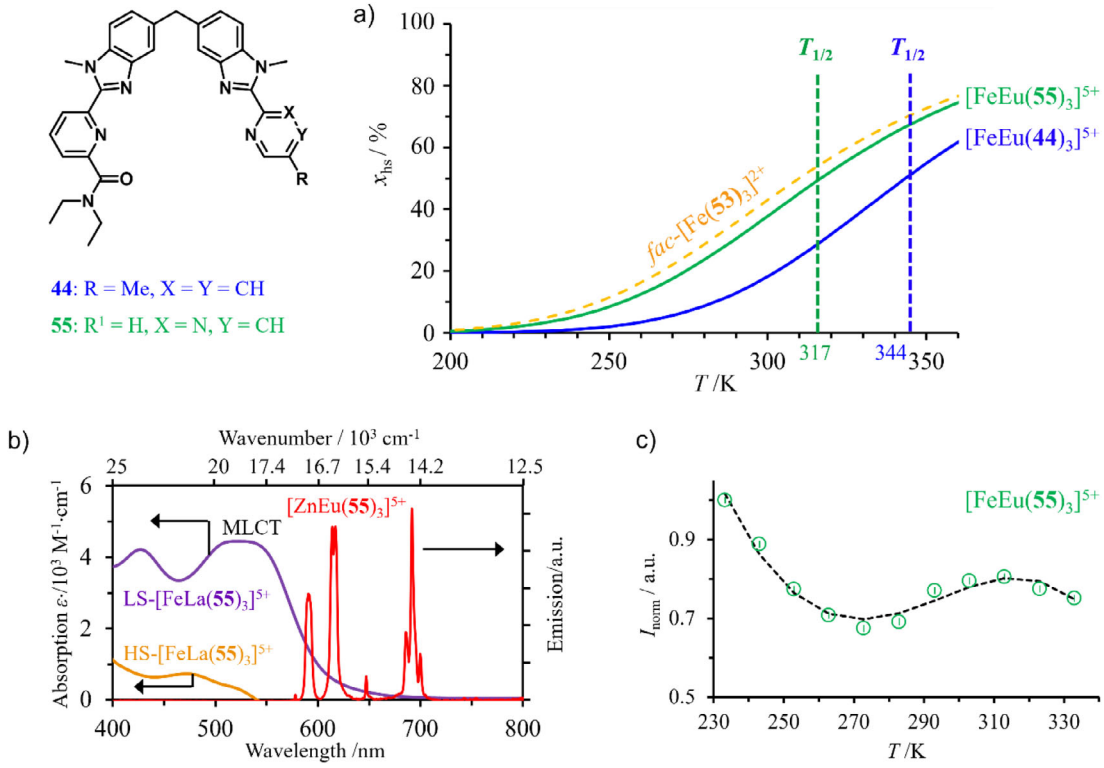

FIGURE 39 | Chemical structure of the ligands **44** and **55**, and (a) HS mole fraction as a function of temperature of the associated $[FeLn(\boldsymbol{k})_3]^{5+}$ ($\boldsymbol{k}$ = **44**, **55**) triple-stranded helicates (adapted from ref [22] with permission from the Royal Society of Chemistry), (b) room temperature electronic absorption spectra (purple trace: LS configuration, yellow trace: HS configuration) and visible Eu(III)-centered emission spectrum (red trace, λ_{exc} = 331 nm) of the $[FeLa(\mathbf{55})_3]^{5+}$ and $[ZnEu(\mathbf{55})_3]^{5+}$ helicates in acetonitrile respectively, and (c) experimental (green disks) and fitted (black dashed traces) normalized total integrated intensity ($I/I_{max} = I_T/I_{233\,K}$) of the Eu(III)-centered emission in $[FeEu(\mathbf{55})_3]^{5+}$ (λ_{exc} = 333 nm). Adapted with permission from ref [127]. Copyright 2024 American Chemical Society.

normalized steady-state Eu(III)-based intensities [127]. At first, the increasingly effective vibrational deactivation ($k_{Eu}^{non-rad}$) of the Eu(III)-centered luminescence dominates the overall response, resulting in an initial decline of the total emitted intensity in the 233–273 K range. Then, the progressive conversion of highly absorbing LS-$[FeEu(\mathbf{55})_3]^{5+}$ into weakly absorbing HS-$[FeEu(\mathbf{55})_3]^{5+}$ considerably reduces the efficiency of the Fe(II)-based quenching via energy transfer processes ($k_{LS}^{q} >> k_{HS}^{q}$,), to the point of overcoming the thermal quenching in the 273–313 K range. Finally, beyond 313 K, $k_{Eu}^{non-rad}$ becomes the dominant

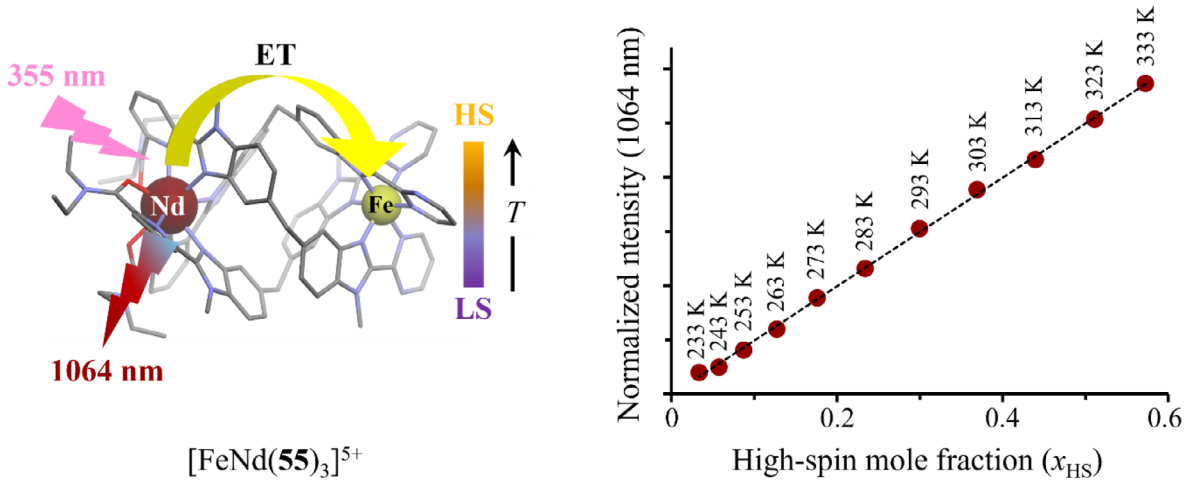

FIGURE 40 | Molecular structure of the $[FeNd(\mathbf{55})_3]^{5+}$ helicate in which the $Nd(^4F_{3/2}\rightarrow{}^4I_J)$ NIR emission intensity is linearly correlated to the mole fraction of HS-Fe(II). Adapted with permission from ref [128]. Copyright 2024 American Chemical Society.

factor in the temperature-dependence once again, leading to a decrease of the overall emitted intensity (Figure 39c) [127].

The second strategy focused on reducing the spectral overlap integral $\Omega_{D,A}$ for the Ln(III)/Fe(II) pair by shifting the emission spectrum of the donor toward lower energies. Thanks to the tunability of the self-assembly process, this was readily accomplished by substituting the Eu(III) in $[FeLn(\mathbf{55})_3](CF_3SO_3)_5$ with the NIR Nd(III) emitter. The resulting $[FeNd(\mathbf{55})_3]^{5+}$ triple-stranded helicate displayed very similar SCO properties to its $[FeEu(\mathbf{55})_3]^{5+}$ analog, with a marginally higher transition temperature $T_{1/2} = 322(2)$ K [128]. As expected, the shift from the visible $Eu(^5D_0\rightarrow{}^7F_J)$ to the NIR $Nd(^4F_{3/2}\rightarrow{}^4I_J)$ emission substantially increased the efficiency of the non-radiative vibration/photon relaxation processes ($k_{Nd}^{non-rad}$) to the extent that they became essentially constant over the temperature range accessible in acetonitrile. Piguet and co-workers also found that the efficiency of the Förster-based Ln(III)→Fe(II) energy transfer processes improved when going from $[FeEu(\mathbf{55})_3]^{5+}$ to $[FeNd(\mathbf{55})_3]^{5+}$ owing to (i) the increased spectral overlap between the low energy $Fe^{II}(^5E\leftarrow{}^5T_2)$ d-d absorption of HS-$[FeNd(\mathbf{55})_3]^{5+}$ and the Nd(III)-based $Nd(^4F_{3/2}\rightarrow{}^4I_J)$ emission bands, and (ii) the enhanced Nd(III) radiative rate constant arising from the spin-allowed character of the latter $Nd(^4F_{3/2}\rightarrow{}^4I_J)$ transitions [128]. The combination of all these elements eventually led to the observation of an unprecedented linear correlation between the increase of the NIR $Nd(^4F_{3/2}\rightarrow{}^4I_J)$ emission intensity and the mole fraction of HS-$[FeNd(\mathbf{55})_3]^{5+}$ complexes (Figure 40).

Concentrating on the d_{DA}^{-6} dependence of the Förster energy transfer rate constant (Equation 13), the third strategy pursued the ambitious objective of increasing the intramolecular Fe(II)•••Eu(III) intermetallic distance by elongating the triple helix through the incorporation of an additional tridentate binding site. Building on previous synthetic efforts [133], the segmental didentate-tridentate-tridentate ligand **56** was prepared in thirteen overall steps using a convergent approach [134]. The subsequent reaction of **56** (3 eq.) with stoichiometric amounts of $M(CF_3SO_3)_3$ (1 eq., $M = Zn^{II}$, Fe^{II}) and $Ln(CF_3SO_3)_3$ (1 eq., $Ln = La^{III}$, Eu^{III}) quantitatively afforded the extended macrotetracyclic trinuclear dimetallic $[MLn_2(\mathbf{56})_3]^{8+}$ helicates (Figure 41a). In these structures, the three successive coordination sites $[MN_6]$-$[LnN_9]$-$[LnN_6O_3]$ are separated by approximately 9 Å, giving a total distance of 18 Å between the Fe(II) and the terminal Eu(III) binding site. It is worth mentioning here that no competing energy transfer process between the two Eu(III) cations is expected since the narrow and non-degenerate character of the $Eu(^5D_0\leftrightarrow{}^7F_0)$ transition precludes significant spectral overlap, and the geometry of the complex enforces sufficient separation to prevent Eu(III)↔Eu(III) communication [135]. Moreover, Piguet and co-workers [136, 137] previously demonstrated that the presence of strongly quenching low-lying LMCT excited states in $[EuN_9]$ chromophores led to differences in quantum yield of several orders of magnitude between the central and terminal sites in related trimetallic $[EuN_6O_3]$-$[EuN_9]$-$[EuN_6O_3]$ helicates. Considerable efforts were devoted to the preparation of heterotrimetallic $[Zn(Ln^A)_x(Ln^B)_{2-x}(\mathbf{56})_3]^{8+}$ helicates in which deviations from the expected statistical distribution in solution could be programmed [134]. However, given the maximum formation of 63(5)% of $[ZnLaEu(\mathbf{56})_3]^{8+}$ under thermodynamic equilibrium at a 1:1:1:3 stoichiometric ratio, the project of preparing the ideal $[FeLaEu(\mathbf{56})_3]^{8+}$ heterotrimetallic assembly, in which a non-emissive and diamagnetic La(III) ion would be selectively bound in the central binding site, was ultimately abandoned in favor of pure $[FeEu_2(\mathbf{56})_3]^{8+}$ complexes [138]. Variable-temperature magnetic measurements performed on the latter showed that the extension of the triple-helical structure had only minor impact on the SCO process in solution, with both dinuclear $[FeEu(\mathbf{44})_3]^{8+}$ and trinuclear $[FeEu_2(\mathbf{56})_3]^{8+}$ complexes displaying nearly identical transitions temperatures $343(3) \leq T_{1/2} \leq 347(2)$ K. Subsequent excitation of the $^1\pi_{2^*}\leftarrow{}^1\pi_1$ band of $[FeEu_2(\mathbf{56})_3]^{8+}$ yielded detectable $Eu(^5D_0\rightarrow{}^7F_J)$ emission originating almost exclusively from the terminal $[EuN_6O_3]$ site [138]. This restoration of Eu(III)-based luminescence demonstrated effective control over the intermetallic communication between the SCO center and the f-block luminophore, and provided long-sought confirmation that residual Eu(III)-centered emission could be exploited to probe the Fe(II) spin-state equilibrium in solution in a straightforward and unambiguous manner. However, the gradual decline of the normalized integrated steady-state intensities of the $Eu(^5D_0\rightarrow{}^7F_J)$ transitions along a convex curve contrasted with the wavy modulation of the emission

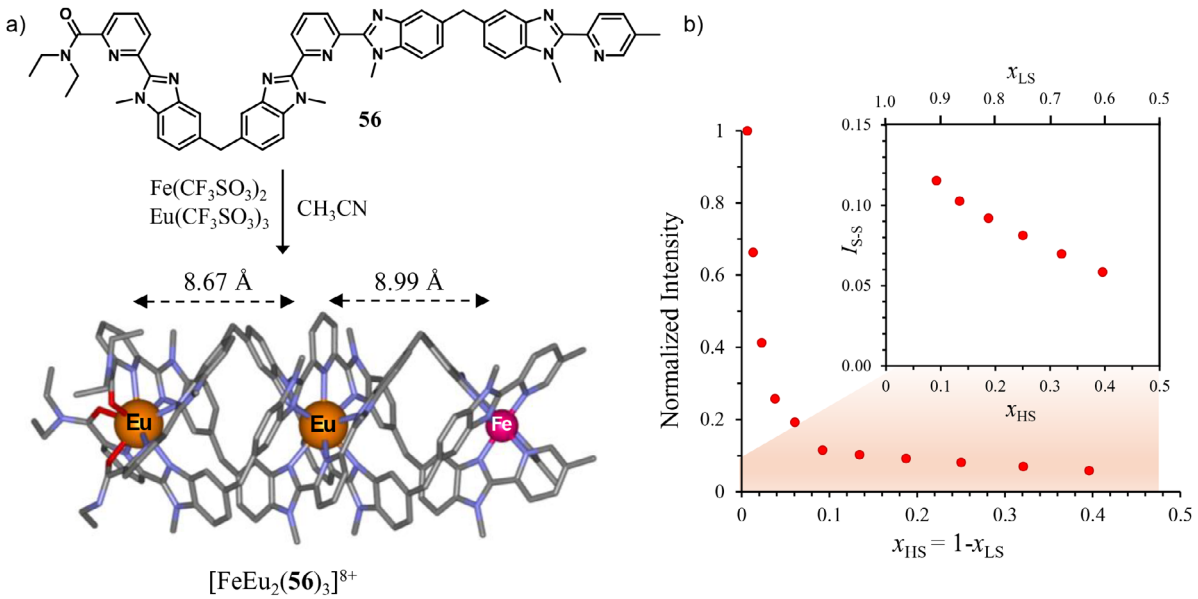

FIGURE 41 | (a) Self-assembly of the macrotetracyclic trinuclear dimetallic $[FeEu_2(\mathbf{56})_3]^{8+}$ triple-stranded helicate in acetonitrile, and (b) plots of the normalized total integrated intensity I_{S-S} of the $Eu(^5D_0 \rightarrow {}^7F_J)$ emission under continuous excitation of the $[FeEu_2(\mathbf{56})_3]^{8+}$ complex (~1 mM in CH_3CN) as a function of the HS-Fe(II) mole fraction. Adapted with permission from ref [138]. Copyright 2024 American Chemical Society.

intensity previously observed in $[FeEu(\mathbf{55})_3]^{5+}$ [127]. A challenging fitting process based on the kinetic model (Figure 38a) but involving the simultaneous treatment of both steady-state and time-dependent luminescence data eventually attributed the close-to-linear decrease of the Eu(III)-based emitted intensity with HS-Fe(II) mole fraction ($0.1 \leq x_{HS} \leq 0.4$) to two factors: (i) a relatively high transition temperature $T_{1/2} = 347(1)$ K, and (ii) the increase of non-radiative vibrational relaxation with temperature, which partially offsets the reduction in quenching efficiency upon the replacement of LS-Fe(II) with HS-Fe(II) [138].

6 | Conclusions and Perspectives

The growing emphasis on multifunctionality in molecular materials has intensified efforts to design SCO systems that exhibit synergistic properties. In this context, the integration of SCO and luminescence within a common framework has garnered significant attention, owing to the appealing dual opportunity to modulate the luminescence response with external stimuli and to monitor the spin-state equilibrium through changes in emission intensity. The high spatial and temporal resolution inherent to luminescence is also extremely attractive at the nanoscale, as it provides superior sensitivity compared to other detection techniques.

Over the past 30 years, the numerous reports of luminescent SCO materials have generally followed one of two main design strategies that consist either of (i) physically doping existing SCO materials with a suitable luminescent moiety, or of (ii) combining the SCO and luminescent entities within a single molecular assembly. One of the main advantages of the first approach is that the relatively low concentration of luminophore found in doped materials minimizes the risk of losing one or both functionalities due to negative interactions between the SCO and luminescent components. Moreover, both properties can be easily and independently tuned, which is highly appealing for application-oriented research. However, the structural characterization of these materials can be challenging, which can hinder detailed mechanistic studies. In addition, the difficulty in controlling the distribution of the luminophore within the material limits the reproducibility and can lead to non-homogeneous dispersions, thereby restricting the sensitivity of the probe to localized regions. In this context, the second strategy paves the way toward a more rational design, in which the controlled structural relationship between the luminescent and SCO moieties enables the elucidation of the interaction mechanism between the two functionalities. Nevertheless, the structural modifications required to covalently bind the two components or aimed at tuning their properties come at the risk of unpredictably losing one or both properties.

Luminescent doping of SCO materials has been investigated in three main classes of materials. Promising developments have been reported in ultra-thin films, with several examples leading to real-world applications. Nanoparticles have also shown great promise, as the transition temperature, the abruptness of the spin-transition, and the size of the hysteresis loop can be precisely controlled by (i) changing their size, (ii) embedding them in rigid matrices, or (iii) adding surfactant molecules. Furthermore, nanoparticles are easy to implement in a variety of environments, making them well-suited for a wide range of potential applications. Lastly, coordination polymers incorporating both luminescent and SCO functionalities have seen an increasing number of reports in the last decade. Their main advantage lies in the presence of multiple intermolecular interactions (H-bonds, van der Waals forces, π–π stacking) that promote cooperative effects, leading to attractive hysteretic behaviors. Their tunable composition and inherent porosity also make them ideal for the incorporation of additional functionalities. However, despite recent progress in the design of 2D and 3D architectures, their

exploration remains impeded by the difficulties associated with their synthesis and reproducibility.

Molecular systems can be distinguished by the nature of the luminescent component. By far, the greatest number of examples involve organic p-block chromophores, either directly used as ligand, or covalently bound to a well-known SCO complex. Their processability, synthetic versatility, not to mention their low cost and ready availability, make them privileged partners, particularly in the context of practical applications. However, these systems often suffer from photobleaching under prolonged light exposure. Fewer studies have explored the use of d-block metal complexes, mostly because desirable luminescent properties are typically limited to rare and expensive third-row transition metals, whereas the more abundant first-row metal ions are well-known luminescence quenchers [139]. Even fewer examples have employed f-block luminophores despite their exceptional optical properties, perhaps because of the complex ligand design required to incorporate both SCO and luminescent Ln(III) ions within a single molecular assembly. Nevertheless, successful lanthanide-based optical detection of Fe(II) spin-state equilibrium was recently achieved, thereby demonstrating the potential of hybrid d-f systems in the development of synergistic luminescent SCO multifunctional materials.

Overall, the field of luminescent SCO materials holds great promise for future research, whether in deciphering the interaction mechanism between the luminophore and the SCO unit, devising new strategies to ensure greater control over their synergetic relationship, or developing new materials for practical applications. One, however, notes that the physical challenges provided by the detection and characterization of spin-crossover processes, with or without photophysical coupling, are currently realized at a (very) high level of performance, and the main remaining limitations concern the rational design of reproducible (supra)molecular entities with innovative, programmed and controlled outreach, a major issue relying on (supra)molecular chemistry. In this context, the coupling of the photophysical response modulated by the spin-crossover process, when realized in (doped) solid materials, requires a delicate treatment in term of error function because one has to replace the microscopic probability pertinent to isolated molecular systems (first-order rate constant) with its macroscopically significant statistical average (second-order rate constant) [40, 140, 141]. Photophysical responses can thus be programmed almost exclusively for isolated (i.e., molecular) D_m/A_n assemblies, where D stands for the luminescent activator (donor) and A for the spin-crossover modulator (acceptor), which pushes heterometallic d-f molecular systems to the forefront of future perspectives in luminescence/spin crossover coupling. If molecular-based systems represent a valuable perspective for these modulable luminescent materials, a second, and complementary challenge remains to be addressed in the ability to program cooperativity in polymetallic SCO architectures at the (supra)molecular level [22, 142].

Authors Contribution

Charlotte Egger wrote the first draft of the review, which was completed, revised, and finalized by both authors through several iterations.

Acknowledgements

The study is financially supported by the Swiss National Science Foundation over three decades and is gratefully acknowledged.

Open access publishing facilitated by Universite de Geneve, as part of the Wiley - Universite de Geneve agreement via the Consortium Of Swiss Academic Libraries.

Conflicts of Interest

The authors declare no conflicts of interest.

Data Availability Statement

Data sharing is not applicable to this article as no new data were created or analyzed in this study.

References

1. L. C. Cambi and A. Cagnasso, "Iron Dithiocarbamates and Nitrosodithiocarbamates," *Atti della Accademia Nazionale dei Lincei, Classe Di Scienze Fisiche, Matematiche e Naturali, Rendiconti* 13 (1931): 809–813.

2. L. S. Cambi, L. Szego, and A. Cagnasso, "The Magnetic Susceptibility of Complexes. V. Iron Dibutyldithiocarbamates," *Atti Della Accademia Nazionale Dei Lincei, Classe Di Scienze Fisiche, Matematiche e Naturali, Rendiconti* 15 (1932): 329–335.

3. L. S. Cambi, L. Szego, and A. Cagnasso, "The Magnetic Susceptibility of Complexes. IV. Ferric *N,N*-dipropyldithiocarbamates," *Atti Della Accademia Nazionale Dei Lincei, Classe Di Scienze Fisiche, Matematiche e Naturali, Rendiconti* 15 (1932): 266–271.

4. H. Toftlund, "Spin Equilibria in Iron(II) Complexes," *Coordination Chemistry Reviews* 94 (1989): 67–108, https://doi.org/10.1016/0010-8545(89)80045-1.

5. P. Gütlich and H. A. Goodwin, *Spin Crossover in Transition Metal Compounds I* (Springer, 2004), 1–47.

6. A. Bousseksou, G. Molnar, L. Salmon, and W. Nicolazzi, "Molecular Spin Crossover Phenomenon: Recent Achievements and Prospects," *Chemical Society Reviews* 40 (2011): 3313–3335, https://doi.org/10.1039/c1cs15042a.

7. K. S. Murray, *Spin-Crossover Materials*, ed. M. A. Halcrow (John Wiley & Sons Ltd, 2013), 1–54.

8. J. S. Griffith and L. E. Orgel, "Ligand-Field Theory," *Quarterly Reviews, Chemical Society* 11 (1957): 381–393, https://doi.org/10.1039/qr9571100381.

9. K. S. Kumar and M. Ruben, "Emerging Trends in Spin Crossover (SCO) Based Functional Materials and Devices," *Coordination Chemistry Reviews* 346 (2017): 176–205, https://doi.org/10.1016/j.ccr.2017.03.024.

10. G. Molnar, S. Rat, L. Salmon, W. Nicolazzi, and A. Bousseksou, "Spin Crossover Nanomaterials: From Fundamental Concepts to Devices," *Advanced Materials* 30 (2018): 17003862, https://doi.org/10.1002/adma.201703862.

11. A.-C. Bas, X. Thompson, L. Salmon, et al., "Bilayer Thin Films That Combine Luminescent and Spin Crossover Properties for an Efficient and Reversible Fluorescence Switching," *Magnetochemistry* 5 (2019): 28, https://doi.org/10.3390/magnetochemistry5020028.

12. H. J. Shepherd, C. M. Quintero, G. Molnár, L. Salmon, and A. Bousseksou, *Spin-Crossover Materials*, ed. M. A. Halcrow (John Wiley & Sons Ltd, 2013), 347–373, https://doi.org/10.1002/9781118519301.

13. W. E. Moerner and D. P. Fromm, "Methods of Single-Molecule Fluorescence Spectroscopy and Microscopy," *Review of Scientific Instruments* 74 (2003): 3597–3619, https://doi.org/10.1063/1.1589587.

14. I. Suleimanov, G. Molnár, L. Salmon, and A. Bousseksou, "Near-Infrared Luminescence Switching in a Spin-Crossover Polymer Nanocomposite," *European Journal of Inorganic Chemistry* 2017 (2017): 3446–3451, https://doi.org/10.1002/ejic.201700426.

15. C. D. Brites, P. P. Lima, N. J. Silva, et al., "Thermometry at the Nanoscale," *Nanoscale* 4 (2012): 4799–4829, https://doi.org/10.1039/c2nr30663h.

16. Y. S. Meng and T. Liu, "Manipulating Spin Transition to Achieve Switchable Multifunctions," *Accounts of Chemical Research* 52 (2019): 1369–1379, https://doi.org/10.1021/acs.accounts.9b00049.

17. L. Pauling, "The Nature of the Chemical Bond. Iii. The Transition From One Extreme Bond Type to Another," *Journal of the American Chemical Society* 54 (1932): 988–1003, https://doi.org/10.1021/ja01342a022.

18. C. D. Coryell, F. Stitt, and L. Pauling, "The Magnetic Properties and Structure of Ferrihemoglobin (Methemoglobin) and Some of Its Compounds," *Journal of the American Chemical Society* 59 (1937): 633–642, https://doi.org/10.1021/ja01283a012.

19. A. Hauser, *Spin Crossover in Transition Metal Compounds I* (Springer, 2004), 49–58.

20. P. Gütlich, A. Hauser, and H. Spiering, "Thermal and Optical Switching of Iron(II) Complexes," *Angewandte Chemie International Edition in English* 33 (1994): 2024–2054.

21. N. Deorukhkar, C. Besnard, L. Guenee, and C. Piguet, "Tuning Spin-Crossover Transition Temperatures in Non-Symmetrical Homoleptic Meridional/Facial [Fe(Didentate) 3] 2+ Complexes: What for and Who Cares About It?," *Dalton Transactions* 50 (2021): 1206–1223, https://doi.org/10.1039/D0DT03828H.

22. T. Lathion, N. Deorukhkar, C. Egger, H. Nozary, and C. Piguet, "Molecular Fe(ii)–Ln(iii) Dyads for Luminescence Reading of Spin-State Equilibria at the Molecular Level," *Dalton Transactions* 53 (2024): 17756–17765, https://doi.org/10.1039/D4DT01868K.

23. T. Lathion, L. Guénée, C. Besnard, A. Bousseksou, and C. Piguet, "Deciphering the Influence of Meridional Versus Facial Isomers in Spin Crossover Complexes," *Chemistry—A European Journal* 24 (2018): 16873–16888, https://doi.org/10.1002/chem.201804161.

24. S. Brooker, "Spin Crossover With Thermal Hysteresis: Practicalities and Lessons Learnt," *Chemical Society Reviews* 44 (2015): 2880–2892, https://doi.org/10.1039/C4CS00376D.

25. Y. Fang, Y.-S. Meng, H. Oshio, and T. Liu, "Understanding of Cooperative Effects in Molecule-Based Spin Transition Materials," *Coordination Chemistry Reviews* 500 (2024): 215483, https://doi.org/10.1016/j.ccr.2023.215483.

26. G. Molnár, I. A. Gural'skyi, L. Salmon, et al., "Bistable Photonic Nanostructures Based on Molecular Spin Crossover Complexes," *Photonic Crystal Materials and Devices X* (2012), paper presented at SPIE Photonics Europe.

27. K. Ridier, A. Hoblos, S. Calvez, et al., "Optical Properties and Photonic Applications of Molecular Spin-Crossover Materials," *Coordination Chemistry Reviews* 535 (2025): 216628, https://doi.org/10.1016/j.ccr.2025.216628.

28. J. H. Gladstone and T. P. Dale, "XIV. Researches on the Refraction, Dispersion, and Sensitiveness of Liquids," *Philosophical Transactions of the Royal Society of London* 153 (1863): 317–343.

29. P. Guionneau, "Crystallography and Spin-Crossover. A View of Breathing Materials," *Dalton Transactions* 43 (2014): 382–393, https://doi.org/10.1039/C3DT52520A.

30. E. Collet and P. Guionneau, "Structural Analysis of Spin-Crossover Materials: From Molecules to Materials," *Comptes Rendus Chimie* 21 (2018): 1133–1151, https://doi.org/10.1016/j.crci.2018.02.003.

31. S. Pillet, "Spin-Crossover Materials: Getting the Most From X-Ray Crystallography," *Journal of Applied Physics* 129 (2021): 181101, https://doi.org/10.1063/5.0047681.

32. C. Andraud and O. Maury, "Lanthanide Complexes for Nonlinear Optics: From Fundamental Aspects to Applications," *European Journal of Inorganic Chemistry* 2009 (2009): 4357–4371, https://doi.org/10.1002/ejic.200900534.

33. R. L. Kronig, "On the Theory of Dispersion of X-Rays," *Journal of the Optical Society of America* 12 (1926): 547–557.

34. T. Lathion, A. Fürstenberg, C. Besnard, A. Hauser, A. Bousseksou, and C. Piguet, "Monitoring Fe(II) Spin-State Equilibria via Eu(III) Luminescence in Molecular Complexes: Dream or Reality?," *Inorganic Chemistry* 59 (2020): 1091–1103, https://doi.org/10.1021/acs.inorgchem.9b02713.

35. M. D. Ward, "Mechanisms of Sensitization of Lanthanide(III)-Based Luminescence in Transition Metal/Lanthanide and Anthracene/Lanthanide Dyads," *Coordination Chemistry Reviews* 254 (2010): 2634–2642, https://doi.org/10.1016/j.ccr.2009.12.001.

36. J. Chong, C. Besnard, C. M. Cruz, C. Piguet, and J. R. Jimenez, "Heteroleptic Mer -[Cr(N ∩ N ∩ N)(CN) 3] Complexes: Synthetic Challenge, Structural Characterization and Photophysical Properties," *Dalton Transactions* 51 (2022): 4297–4309, https://doi.org/10.1039/D2DT00126H.

37. T. Förster, "Zwischenmolekulare Energiewanderung Und Fluoreszenz," *Annalen der Physik* 437 (1948): 55–75.

38. A. Ito and T. J. Meyer, "The Golden Rule. Application for Fun and Profit in Electron Transfer, Energy Transfer, and Excited-State Decay," *Physical Chemistry Chemical Physics* 14 (2012): 13731, https://doi.org/10.1039/c2cp41658a.

39. D. L. Dexter, "A Theory of Sensitized Luminescence in Solids," *Journal of Chemical Physics* 21 (1953): 836–850, https://doi.org/10.1063/1.1699044.

40. M. Inokuti and F. Hirayama, "Influence of Energy Transfer by the Exchange Mechanism on Donor Luminescence," *The Journal of Chemical Physics* 43 (1965): 1978–1989, https://doi.org/10.1063/1.1697063.

41. A. N. Carneiro Neto, E. E. S. Teotonio, G. F. de Sá, et al., "Modeling Intramolecular Energy Transfer in lanthanide Chelates: A Critical Review and Recent Advances", in *Handbook on the Physics and Chemistry of Rare Earths*, Eds. J.-C. G. Bünzli, V. K. Pecharsky (Amsterdam: Elsevier, 2019), Vol. 56, 55162, https://doi.org/10.1016/bs.hpcre.2019.08.001.

42. M. Matsuda and H. Tajima, "Thin Film of a Spin Crossover Complex [Fe(dpp)2](BF4)2," *Chemistry Letters* 36 (2007): 700–701, https://doi.org/10.1246/cl.2007.700.

43. M. Matsuda, H. Isozaki, and H. Tajima, "Reproducible on–off Switching of the Light Emission From the Electroluminescent Device Containing a Spin Crossover Complex," *Thin Solid Films* 517 (2008): 1465–1467, https://doi.org/10.1016/j.tsf.2008.09.034.

44. M. Matsuda, H. Isozaki, and H. Tajima, "Electroluminescence Quenching Caused by a Spin-Crossover Transition," *Chemistry Letters* 37 (2008): 374–375, https://doi.org/10.1246/cl.2008.374.

45. M. Matsuda, K. Kiyoshima, R. Uchida, N. Kinoshita, and H. Tajima, "Characteristics of Organic Light-Emitting Devices Consisting of Dye-Doped Spin Crossover Complex Films," *Thin Solid Films* 531 (2013): 451–453, https://doi.org/10.1016/j.tsf.2013.01.094.

46. L. Salmon, G. Molnár, D. Zitouni, et al., "A Novel Approach for Fluorescent Thermometry and Thermal Imaging Purposes Using Spin Crossover Nanoparticles," *Journal of Materials Chemistry* 20 (2010): 5499–5503, https://doi.org/10.1039/c0jm00631a.

47. C. Quintero, G. Molnár, L. Salmon, A. Tokarev, C. Bergaud, and A. Bousseksou, "Design of Fluorescent Spin-Crossover Nanoparticles for Thermometry Applications," *16th International Workshop on Thermal Investigations of ICs and Systems (THERMINIC)* (IEEE, 2010), 6.

48. C. M. Quintero, I. A. Gural'skiy, L. Salmon, G. Molnár, C. Bergaud, and A. Bousseksou, "Soft Lithographic Patterning of Spin Crossover Complexes. Part 1: Fluorescent Detection of the Spin Transition in Single Nano-Objects," *Journal of Materials Chemistry* 22 (2012): 3745–3751, https://doi.org/10.1039/c2jm15662h.

49. I. A. Gural'skiy, C. M. Quintero, K. Abdul-Kader, et al., "Detection of Molecular Spin-State Changes in Ultrathin Films by Photonic Methods," *Journal of Nanophotonics* 6 (2012): 0563517, https://doi.org/10.1117/1.jnp.6.063517.

50. I. Sanchez-Molina, D. Nieto-Castro, A. Moneo-Corcuera, E. Martinez-Ferrero, and J. R. Galan-Mascaros, "Synergic Bistability Between Spin

Transition and Fluorescence in Polyfluorene Composites With Spin Crossover Polymers," *Journal of Physical Chemistry Letters* 12 (2021): 10479–10485, https://doi.org/10.1021/acs.jpclett.1c02811.

51. V. Nagy, K. Halász, M.-T. Carayon, et al., "Cellulose Fiber Nanocomposites Displaying Spin-Crossover Properties," *Colloids and Surfaces A: Physicochemical and Engineering Aspects* 456 (2014): 35–40, https://doi.org/10.1016/j.colsurfa.2014.05.007.

52. I. Suleimanov, O. Kraieva, J. Sánchez Costa, et al., "Electronic Communication Between Fluorescent Pyrene Excimers and Spin Crossover Complexes in Nanocomposite Particles," *Journal of Materials Chemistry C* 3 (2015): 5026–5032, https://doi.org/10.1039/C5TC00667H.

53. I. Suleimanov, O. Kraieva, G. Molnar, L. Salmon, and A. Bousseksou, "Enhanced Luminescence Stability With a Tb–Spin Crossover Nanocomposite for Spin State Monitoring," *Chemical Communications* 51 (2015): 15098–15101, https://doi.org/10.1039/C5CC06426K.

54. O. Kraieva, I. Suleimanov, G. Molnár, L. Salmon, and A. Bousseksou, "CdTe Quantum Dot Fluorescence Modulation by Spin Crossover," *Magnetochemistry* 2 (2016): 11, https://doi.org/10.3390/magnetochemistry2010011.

55. J. M. Herrera, S. Titos-Padilla, S. J. A. Pope, et al., "Studies on Bifunctional Fe(ii)-Triazole Spin Crossover Nanoparticles: Time-Dependent Luminescence, Surface Grafting and the Effect of a Silica Shell and Hydrostatic Pressure on the Magnetic Properties," *Journal of Materials Chemistry C* 3 (2015): 7819–7829, https://doi.org/10.1039/C5TC00685F.

56. S. Titos-Padilla, J. M. Herrera, X. W. Chen, J. J. Delgado, and E. Colacio, "Bifunctional Hybrid SiO2 Nanoparticles Showing Synergy Between Core Spin Crossover and Shell Luminescence Properties," *Angewandte Chemie* 123 (2011): 3348–3351, https://doi.org/10.1002/ange.201007847.

57. M. A. Halcrow, "The Spin-states and Spin-Transitions of Mononuclear Iron(II) Complexes of Nitrogen-Donor Ligands," *Polyhedron* 26 (2007): 3523–3576, https://doi.org/10.1016/j.poly.2007.03.033.

58. A. Hauser, J. Jeftić, H. Romstedt, R. Hinek, and H. Spiering, "Cooperative Phenomena and Light-Induced Bistability in Iron(II) Spin-Crossover Compounds," *Coordination Chemistry Reviews* 190-192 (1999): 471–491, https://doi.org/10.1016/S0010-8545(99)00111-3.

59. C. A. Tovee, C. A. Kilner, J. A. Thomas, and M. A. Halcrow, "Co-Crystallising Two Functional Complex Molecules in a Terpyridine Embrace Lattice," *CrystEngComm* 11 (2009): 2069–2077, https://doi.org/10.1039/b904528g.

60. C. F. Wang, R. F. Li, X. Y. Chen, R. J. Wei, L. S. Zheng, and J. Tao, "Synergetic Spin Crossover and Fluorescence in One-Dimensional Hybrid Complexes," *Angewandte Chemie International Edition* 54 (2014): 1574–1577, https://doi.org/10.1002/anie.201410454.

61. C. F. Wang, G. Y. Yang, Z. S. Yao, and J. Tao, "Monitoring the Spin States of Ferrous Ions by Fluorescence Spectroscopy in Spin-Crossover-Fluorescent Hybrid Materials," *Chemistry—A European Journal* 24 (2018): 3218–3224, https://doi.org/10.1002/chem.201704901.

62. T. Delgado, M. Meneses-Sanchez, L. Pineiro-Lopez, C. Bartual-Murgui, M. C. Munoz, and J. A. Real, "Thermo- and Photo-Modulation of Exciplex Fluorescence in a 3D Spin Crossover Hofmann-Type Coordination Polymer," *Chemical Science* 9 (2018): 8446–8452, https://doi.org/10.1039/C8SC02677G.

63. M. Meneses-Sánchez, L. Piñeiro-López, T. Delgado, et al., "Extrinsic vs. Intrinsic Luminescence and Their Interplay With Spin Crossover in 3D Hofmann-Type Coordination Polymers," *Journal of Materials Chemistry C* 8 (2020): 1623–1633, https://doi.org/10.1039/C9TC06422B.

64. J. Y. Ge, Z. Chen, L. Zhang, et al., "A Two-Dimensional Iron(II) Coordination Polymer With Synergetic Spin-Crossover and Luminescent Properties," *Angewandte Chemie International Edition* 58 (2019): 8789–8793, https://doi.org/10.1002/anie.201903281.

65. Y. R. Qiu, L. Cui, J. Y. Ge, M. Kurmoo, G. Ma, and J. Su, "Iron(II) Spin Crossover Coordination Polymers Derived From a Redox Active Equatorial Tetrathiafulvalene Schiff-Base Ligand," *Frontiers in Chemistry* 9 (2021): 692939, https://doi.org/10.3389/fchem.2021.692939.

66. S. Ghosh, S. Kamilya, T. Pramanik, et al., "ON/OFF Photoswitching and Thermoinduced Spin Crossover With Cooperative Luminescence in a 2D Iron(II) Coordination Polymer," *Inorganic Chemistry* 59 (2020): 13009–13013, https://doi.org/10.1021/acs.inorgchem.0c02136.

67. V. García-López, F. Marques-Moros, J. Troya, J. Canet-Ferrer, M. Clemente-Lóen, and E. Coronado, "Spin-Crossover Tuning of the Luminescence in 2D Hofmann-Type Compounds in Bulk and Exfoliated Flakes," *Journal of Materials Chemistry C* 12 (2023): 161–169, https://doi.org/10.1039/d3tc03693f.

68. Y. Garcia, F. Robert, A. D. Naik, et al., "Spin Transition Charted in a Fluorophore-Tagged Thermochromic Dinuclear Iron(II) Complex," *Journal of the American Chemical Society* 133 (2011): 15850–15853, https://doi.org/10.1021/ja205974q.

69. N. F. Sciortino, K. A. Zenere, M. E. Corrigan, et al., "Four-Step Iron(ii) Spin state Cascade Driven by Antagonistic Solid State Interactions," *Chemical Science* 8 (2017): 701–707, https://doi.org/10.1039/C6SC03114E.

70. X.-R. Wu, S.-Q. Wu, Z.-K. Liu, et al., "Manipulating Guest-Responsive Spin Transition to Achieve Switchable Fluorescence in a Hofmann-Type Framework," *Science China Chemistry* 67 (2024): 3339–3346, https://doi.org/10.1007/s11426-024-2222-3.

71. D. W. Cho and D. W. Cho, "Excimer and Exciplex Emissions of 1,8-Naphthalimides Caused by Aggregation in Extremely Polar or Nonpolar Solvents," *New Journal of Chemistry* 38 (2014): 2233–2236, https://doi.org/10.1039/C3NJ01473H.

72. W. Phonsri, P. Harding, L. Liu, et al., "Solvent Modified Spin Crossover in an Iron(iii) Complex: Phase Changes and an Exceptionally Wide Hysteresis," *Chemical Science* 8 (2017): 3949–3959, https://doi.org/10.1039/C6SC05317C.

73. X.-P. Sun, R.-J. Wei, Z.-S. Yao, and J. Tao, "Solvent Effects on the Structural Packing and Spin-Crossover Properties of a Mononuclear Iron(II) Complex," *Crystal Growth & Design* 18 (2018): 6853–6862, https://doi.org/10.1021/acs.cgd.8b01079.

74. H. Kurz, K. Schotz, I. Papadopoulos, et al., "A Fluorescence-Detected Coordination-Induced Spin State Switch," *Journal of the American Chemical Society* 143 (2021): 3466–3480, https://doi.org/10.1021/jacs.0c12568.

75. K. Sun, J. P. Xue, Z. S. Yao, and J. Tao, "Synergistic Strategies for the Synthesis of Fe(II)-Based Bifunctional Fluorescent Spin-Crossover Materials," *Dalton Transactions* 51 (2022): 16044–16054, https://doi.org/10.1039/D2DT02604J.

76. M. Hasegawa, F. Renz, T. Hara, et al., "Fluorescence Spectra of Fe(II) Spin Crossover Complexes With 2,6-Bis(benzimidazole-2′-yl)Pyridine," *Chemical Physics* 277 (2002): 21–30, https://doi.org/10.1016/S0301-0104(01)00706-6.

77. Y. Jiao, J. Zhu, Y. Guo, W. He, and Z. Guo, "Synergetic Effect Between Spin Crossover and Luminescence in the [Fe(bpp)2][BF4]2 (bpp = 2,6-Bis(pyrazol-1-yl)Pyridine) Complex," *Journal of Materials Chemistry C* 5 (2017): 5214–5222, https://doi.org/10.1039/C7TC00507E.

78. J. M. Holland, C. A. Kilner, M. Thornton-Pett, M. A. Halcrow, J. A. McAllister, and Z. Lu, "An Unusual Abrupt Thermal Spin-State Transition in [FeL2][BF4]2 [L = 2,6-Di(Pyrazol-1-yl)Pyridine]," *Chemical Communications* (2001): 577–578, https://doi.org/10.1039/b100995h.

79. H. Matsukizono, K. Kuroiwa, and N. Kimizuka, "Self-Assembly-Directed Spin Conversion of Iron(II) 1,2,4-Triazole Complexes in Solution and Their Effect on Photorelaxation Processes of Fluorescent Counter Ions," *Chemistry Letters* 37 (2008): 446–447, https://doi.org/10.1246/cl.2008.446.

80. C. Lochenie, K. G. Wagner, M. Karg, and B. Weber, "Modulation of the Ligand-based Fluorescence of 3D Metal Complexes Upon Spin State Change," *Journal of Materials Chemistry C* 3 (2015): 7925–7935, https://doi.org/10.1039/C5TC00837A.

81. C. Lochenie, K. Schötz, F. Panzer, et al., "Spin-Crossover Iron(II) Coordination Polymer With Fluorescent Properties: Correlation Between

Emission Properties and Spin State," *Journal of the American Chemical Society* 140 (2018): 700–709, https://doi.org/10.1021/jacs.7b10571.

82. M. Estrader, J. Salinas Uber, L. A. Barrios, et al., "A Magneto-Optical Molecular Device: Interplay of Spin Crossover, Luminescence, Photomagnetism, and Photochromism," *Angewandte Chemie International Edition* 56 (2017): 15622–15627, https://doi.org/10.1002/anie.201709136.

83. J. Wang, M. Kong, X. J. Song, Y. Jing, Y. Zhao, and Y. Song, "Synergetic Spin-Crossover and Luminescent Properties in a Multifunctional 2D Iron(II) Coordination Polymer," *Inorganic Chemistry* 61 (2022): 20923–20930, https://doi.org/10.1021/acs.inorgchem.2c03350.

84. D. Y. Chen, C. Yi, X. F. Li, et al., "A Mononuclear Iron(ii) Complex Constructed Using a Complementary Ligand Pair Exhibits Intrinsic Luminescence–Spin-Crossover Coupling," *Dalton Transactions* 54 (2025): 2908–2915, https://doi.org/10.1039/D4DT03177F.

85. S. Y. Wang, J. H. Fu, Y. P. Liang, Y. J. He, Y. S. Chen, and Y. T. Chan, "Metallo-Supramolecular Self-Assembly of a Multicomponent Ditrigon Based on Complementary Terpyridine Ligand Pairing," *Journal of the American Chemical Society* 138 (2016): 3651–3654, https://doi.org/10.1021/jacs.6b01005.

86. M. Seredyuk, K. Znovjyak, F. J. Valverde-Munoz, et al., "105 K Wide Room Temperature Spin Transition Memory Due to a Supramolecular Latch Mechanism," *Journal of the American Chemical Society* 144 (2022): 14297–14309, https://doi.org/10.1021/jacs.2c05417.

87. M. Seredyuk, K. Znovjyak, F. J. Valverde-Muñoz, et al., "60 K Wide Hysteresis Embracing Room Temperature in a Fluorescent FeII Spin Transition Complex," *Inorganic Chemistry Frontiers* 12 (2025): 4583–4596, https://doi.org/10.1039/D5QI00856E.

88. F. Renz, H. Spiering, H. A. Goodwin, and P. Gütlich, "Light-perturbed Hysteresis in an Iron(II) Spin-Crossover Compound Observed by the Mössbauer Effect," *Hyperfine Interactions* 126 (2000): 155–158, https://doi.org/10.1023/A:1012609231853.

89. K. Boukheddaden, H. Fourati, Y. Singh, and G. Chastanet, "Evidence of Photo-Thermal Effects on the First-Order Thermo-Induced Spin Transition of [{Fe(NCSe)(py)2}2(m-bpypz)] Spin-Crossover Material," *Magnetochemistry* 5 (2019): 21, https://doi.org/10.3390/magnetochemistry5020021.

90. M. Engeser, L. Fabbrizzi, M. Licchelli, and D. Sacchi, "A Fluorescent Molecular Thermometer Based on the Nickel(II) High-Spin/Low-Spin Interconversion," *Chemical Communications* (1999): 1191–1192, https://doi.org/10.1039/a901931f.

91. F. Robert, A. D. Naik, B. Tinant, R. Robiette, and Y. Garcia, "Insights Into the Origin of Solid-State Photochromism and Thermochromism of N-Salicylideneanils: The Intriguing Case of Aminopyridines," *Chemistry—A European Journal* 15 (2009): 4327–4342, https://doi.org/10.1002/chem.200801932.

92. F. Robert, A. D. Naik, F. Hidara, et al., "Engineering Solid-State Molecular Switches: N-Salicylidene N-Heterocycle Derivatives," *European Journal of Organic Chemistry* 2010 (2010): 621–637, https://doi.org/10.1002/ejoc.200901175.

93. R. González-Prieto, B. Fleury, F. Schramm, et al., "Tuning the Spin-Transition Properties of Pyrene-Decorated 2,6-Bispyrazolylpyridine Based Fe(ii) Complexes," *Dalton Transactions* 40 (2011): 7564–7570, https://doi.org/10.1039/c1dt10420a.

94. C.-F. Wang, M.-J. Sun, Q.-J. Guo, Z.-X. Cao, L.-S. Zheng, and J. Tao, "Multiple Correlations Between Spin Crossover and Fluorescence in a Dinuclear Compound," *Chemical Communications* 52 (2016): 14322–14325, https://doi.org/10.1039/C6CC07810A.

95. O. Roubeau, P. Gamez, and S. J. Teat, "Dinuclear Complexes With a Triple N1,N2-Triazole Bridge That Exhibit Partial Spin Crossover and Weak Antiferromagnetic Interactions," *European Journal of Inorganic Chemistry* 2013 (2012): 934–942, https://doi.org/10.1002/ejic.201201126.

96. C. F. Wang, M. J. Sun, Q. J. Guo, Z. X. Cao, L. S. Zheng, and J. Tao, "Correction: Multiple Correlations Between Spin Crossover and Fluorescence in a Dinuclear Compound," *Chemical Communications* 59 (2023): 10821, https://doi.org/10.1039/D3CC90276E.

97. J. L. Wang, Q. Liu, X. J. Lv, R. L. Wang, C. Y. Duan, and T. Liu, "Magnetic Fluorescent Bifunctional Spin-Crossover Complexes," *Dalton Transactions* 45 (2016): 18552–18558, https://doi.org/10.1039/C6DT03714C.

98. J. L. Wang, Q. Liu, Y. S. Meng, et al., "Fluorescence Modulation via Photoinduced Spin Crossover Switched Energy Transfer From Fluorophores to Fe II Ions," *Chemical Science* 9 (2018): 2892–2897, https://doi.org/10.1039/C7SC05221A.

99. B. X. Luo, Y. Pan, Y. S. Meng, et al., "Construction of Magneto-Fluorescent Bifunctional Spin-Crossover Fe(II) Complex From Pyrene-Decorated Pybox Ligand," *European Journal of Inorganic Chemistry* 2021 (2021): 3992–3999, https://doi.org/10.1002/ejic.202100622.

100. Y. Y. Zhu, C. W. Liu, J. Yin, et al., "Structural Phase Transition in a Multi-Induced Mononuclear Fe II Spin-Crossover Complex," *Dalton Transactions* 44 (2015): 20906–20912, https://doi.org/10.1039/C5DT03216D.

101. Y.-Y. Zhu, H.-Q. Li, Z.-Y. Ding, et al., "Spin Transitions in a Series of [Fe(pybox)2]2+ Complexes Modulated by Ligand Structures, Counter Anions, and Solvents," *Inorganic Chemistry Frontiers* 3 (2016): 1624–1636, https://doi.org/10.1039/C6QI00417B.

102. A. de Bettencourt-Dias, P. S. Barber, S. Viswanathan, et al., "Para-Derivatized Pybox Ligands as Sensitizers in Highly Luminescent Ln(III) Complexes," *Inorganic Chemistry* 49 (2010): 8848–8861, https://doi.org/10.1021/ic101034y.

103. H.-Q. Li, Z.-Y. Ding, Y. Pan, C.-H. Liu, and Y.-Y. Zhu, "Fluorescence Tuning of Zn(ii)-Based Metallo-Supramolecular Coordination Polymers and Their Application for Picric Acid Detection," *Inorganic Chemistry Frontiers* 3 (2016): 1363–1375, https://doi.org/10.1039/C6QI00267F.

104. C. Yi, Y.-S. Meng, L. Zhao, et al., "A Smart Molecule Showing Spin Crossover Responsive Aggregation-Induced Emission," *CCS Chemistry* 5 (2023): 915–924, https://doi.org/10.31635/ccschem.022.202201950.

105. Z. Wang, J. Nie, W. Qin, Q. Hu, and B. Z. Tang, "Gelation Process Visualized by Aggregation-Induced Emission Fluorogens," *Nature Communications* 7 (2016): 12033, https://doi.org/10.1038/ncomms12033.

106. N. Zhang, H. Chen, Y. Fan, et al., "Fluorescent Polymersomes With Aggregation-Induced Emission," *ACS Nano* 12 (2018): 4025–4035, https://doi.org/10.1021/acsnano.8b01755.

107. Y. Shi, G. Yin, Z. Yan, et al., "Helical Sulfono-γ-AApeptides With Aggregation-Induced Emission and Circularly Polarized Luminescence," *Journal of the American Chemical Society* 141 (2019): 12697–12706, https://doi.org/10.1021/jacs.9b05329.

108. J. Yuan, S. Q. Wu, M. J. Liu, O. Sato, and H. Z. Kou, "Rhodamine 6G-Labeled Pyridyl Aroylhydrazone Fe(II) Complex Exhibiting Synergetic Spin Crossover and Fluorescence," *Journal of the American Chemical Society* 140 (2018): 9426–9433, https://doi.org/10.1021/jacs.8b00103.

109. L. Zhang, G. C. Xu, H. B. Xu, et al., "Abrupt Spin Transition Around Room Temperature and Light Induced Properties in FeII Complexes With N4O2 Coordination Sphere," *Chemical Communications* 46 (2010): 2554–2556, https://doi.org/10.1039/b925917a.

110. Y. Zhao, X. B. Zhang, Z. X. Han, et al., "Highly Sensitive and Selective Colorimetric and Off–On Fluorescent Chemosensor for Cu 2+ in Aqueous Solution and Living Cells," *Analytical Chemistry* 81 (2009): 7022–7030, https://doi.org/10.1021/ac901127n.

111. J. Yuan, M.-J. Liu, S.-Q. Wu, et al., "Substituent Effects on the Fluorescent Spin-Crossover Fe(ii) Complexes of Rhodamine 6G Hydrazones," *Inorganic Chemistry Frontiers* 6 (2019): 1170–1176, https://doi.org/10.1039/C9QI00111E.

112. B. Benaicha, K. Van Do, A. Yangui, et al., "Interplay Between Spin-Crossover and Luminescence in a Multifunctional Single Crystal Iron (II) Complex: Towards a New Generation of Molecular Sensors," *Chemical Science* 10 (2019): 6791–6798, https://doi.org/10.1039/c9sc02331c.

113. J. Feng, X. Wang, L. Wang, et al., "Naphthalimide-Tagged Iron(II) Spin Crossover Complex With Synergy of Ratiometric Fluorescence for Thermosensing," *Inorganic Chemistry* 63 (2024): 108–116, https://doi.org/10.1021/acs.inorgchem.3c01789.

114. M. Kaupp, "The Role of Radial Nodes of Atomic Orbitals for Chemical Bonding and the Periodic Table," *Journal of Computational Chemistry* 28 (2007): 320–325, https://doi.org/10.1002/jcc.20522.

115. J. K. McCusker, "Electronic Structure in the Transition Metal Block and Its Implications for Light Harvesting," *Science* 363 (2019): 484–488, https://doi.org/10.1126/science.aav9104.

116. C. Wegeberg and O. S. Wenger, "Luminescent First-Row Transition Metal Complexes," *JACS Au* 1 (2021): 1860–1876, https://doi.org/10.1021/jacsau.1c00353.

117. H. Kurz, C. Lochenie, K. G. Wagner, S. Schneider, M. Karg, and B. Weber, "Synthesis and Optical Properties of Phenanthroline-Derived Schiff Base-Like Dinuclear Ru II –Ni II Complexes," *Chemistry—A European Journal* 24 (2018): 5100–5111, https://doi.org/10.1002/chem.201704632.

118. B. Schäfer, T. Bauer, I. Faus, et al., "A Luminescent Pt $_2$Fe Spin Crossover Complex," *Dalton Transactions* 46 (2017): 2289–2302, https://doi.org/10.1039/C6DT04360G.

119. B. M. Van der Ende, L. Aarts, and A. Meijerink, "Lanthanide Ions as Spectral Converters for Solar Cells," *Physical Chemistry Chemical Physics* 11 (2009): 11081–11095, https://doi.org/10.1039/b913877c.

120. J.-C. G. Bünzli, "Lanthanide Light for Biology and Medical Diagnosis," *Journal of Luminescence* 170 (2016): 866–878, https://doi.org/10.1016/j.jlumin.2015.07.033.

121. Z. Wang and B. Xing, "Near-Infrared Multipurpose Lanthanide-Imaging Nanoprobes," *Chemistry—An Asian Journal* 15 (2020): 2076–2091, https://doi.org/10.1002/asia.202000493.

122. C. Piguet, E. Rivara-Minten, G. Hopfgartner, and J.-C. G. Bünzli, "Molecular Magnetism and Iron(II) Spin-State Equilibrium as Structural Probes in Heterodinuclear D–f Complexes," *Helvetica Chimica Acta* 78 (1995): 1651–1672, https://doi.org/10.1002/hlca.19950780704.

123. C. Piguet, G. Bernardinelli, J. C. G. Bunzli, S. Petoud, and G. Hopfgartner, "The First Structurally Characterized and Strongly Luminescent Self-Assembled Helical Heterodinuclear D–f Complex," *Journal of the Chemical Society, Chemical Communications* (1995): 2575–2577, https://doi.org/10.1039/C39950002575.

124. C. Piguet, E. Rivara-Minten, G. Bernardinelli, J.-C. G. Bünzli, and G. Hopfgartner, "Non-Covalent Lanthanide Podates With Predetermined Physicochemical Properties: Iron(II) Spin-State Equilibria in Self-Assembled Heterodinuclear D–f Supramolecular Complexes," *Journal of the Chemical Society, Dalton Transactions* (1997): 421–434, https://doi.org/10.1039/a605986d.

125. C. Edder, C. Piguet, G. Bernardinelli, et al., "Unusual Electronic Effects of Electron-Withdrawing Sulfonamide Groups in Optically and Magnetically Active Self-Assembled Noncovalent Heterodimetallic D–f Podates," *Inorganic Chemistry* 39 (2000): 5059–5073, https://doi.org/10.1021/ic000687o.

126. C. Edder, C. Piguet, J. C. Bünzli, and G. Hopfgartner, "High-Spin Iron(II) as a Semitransparent Partner for Tuning Europium(III) Luminescence in Heterodimetallic D-f Complexes," *Chemistry—A European Journal* 7 (2001): 3014–3024, https://doi.org/10.1002/1521-3765(20010716)7:14%3c3014::AID-CHEM3014%3e3.0.CO;2-D.

127. N. Deorukhkar, C. Egger, L. Guenee, C. Besnard, and C. Piguet, "Detecting Fe(II) Spin-Crossover by Modulation of Appended Eu(III) Luminescence in a Single Molecule," *Journal of the American Chemical Society* 146 (2024): 308–318, https://doi.org/10.1021/jacs.3c09017.

128. N. Deorukhkar, C. Egger, A. Rosspeintner, and C. Piguet, "Unravelling Kinetics of Intramolecular Nd(III) –>Fe(II) Energy Transfer in Spin Crossover Single Molecules: Dotting the i's and Crossing the T's," *Journal of the American Chemical Society* 146 (2024): 19386–19396, https://doi.org/10.1021/jacs.3c09017.

129. H. Phan, J. J. Hrudka, D. Igimbayeva, L. M. Lawson Daku, and M. Shatruk, "A Simple Approach for Predicting the Spin State of Homoleptic Fe(II) Tris-diimine Complexes," *Journal of the American Chemical Society* 139 (2017): 6437–6447, https://doi.org/10.1021/jacs.7b02098.

130. N. Deorukhkar, T. Lathion, L. Guenee, C. Besnard, and C. Piguet, "The Tyranny of Arm-Wrestling Methyls on Iron(II) Spin State in Pseudo-Octahedral [Fe(didentate)3] Complexes," *Chemistry (Weinheim An Der Bergstrasse, Germany)* 2 (2020): 231–252, https://doi.org/10.3390/chemistry2020015.

131. K. P. Kepp, "Theoretical Study of Spin Crossover in 30 Iron Complexes," *Inorganic Chemistry* 55 (2016): 2717–2727, https://doi.org/10.1021/acs.inorgchem.5b02371.

132. L. Aboshyan-Sorgho, T. Lathion, L. Guenee, C. Besnard, and C. Piguet, "Thermodynamic N-Donor Trans Influence in Labile Pseudo-Octahedral Zinc Complexes: A Delusion?," *Inorganic Chemistry* 53 (2014): 13093–13104, https://doi.org/10.1021/ic5022559.

133. T. Riis-Johannessen, G. Bernardinelli, Y. Filinchuk, S. Clifford, N. D. Favera, and C. Piguet, "Self-Assembly of the First Discrete 3d−4f−4f Triple-Stranded Helicate," *Inorganic Chemistry* 48 (2009): 5512–5525, https://doi.org/10.1021/ic900654m.

134. C. Egger, L. Guenee, N. Deorukhkar, and C. Piguet, "Programming Heterometallic 4f–4f′ Helicates Under Thermodynamic Control: The Circle is Complete," *Dalton Transactions* 53 (2024): 6050–6062, https://doi.org/10.1039/D4DT00610K.

135. A. Zaim, S. V. Eliseeva, L. Guenee, H. Nozary, S. Petoud, and C. Piguet, "Lanthanide-to-Lanthanide Energy-Transfer Processes Operating in Discrete Polynuclear Complexes: Can Trivalent Europium Be Used as a Local Structural Probe?," *Chemistry—A European Journal* 20 (2014): 12172–12182, https://doi.org/10.1002/chem.201403206.

136. S. Petoud, J.-C. G. Bünzli, T. Glanzman, C. Piguet, Q. Xiang, and R. P. Thummel, "Influence of Charge-Transfer States on the Eu(III) Luminescence in Mononuclear Triple Helical Complexes With Tridentate Aromatic Ligands," *Journal of Luminescence* 82 (1999): 69–79, https://doi.org/10.1016/S0022-2313(99)00015-0.

137. S. Floquet, N. Ouali, B. Bocquet, et al., "The First Self-Assembled Trimetallic Lanthanide Helicates Driven by Positive Cooperativity," *Chemistry—A European Journal* 9 (2003): 1860–1875, https://doi.org/10.1002/chem.200390214.

138. C. Egger, N. Deorukhkar, L. Guenee, and C. Piguet, "Modulation of Eu(III)-Centered Luminescence by Fe(II) Spin-Crossover in Extended Trinuclear Helicates," *Inorganic Chemistry* 64 (2025): 13905–13917, https://doi.org/10.1021/acs.inorgchem.5c01928.

139. G. Morselli, C. Reber, and O. S. Wenger, "Molecular Design Principles for Photoactive Transition Metal Complexes: A Guide for "Photo-Motivated" Chemists," *Journal of the American Chemical Society* 147 (2025): 11608–11624, https://doi.org/10.1021/jacs.5c02096.

140. T. Förster, "Experimentelle und Theoretische Untersuchung des Zwischenmolekularen Übergangs von Elektronenanregungsenergie," *Zeitschrift Für Naturforschung A* 4 (1949): 321–327, https://doi.org/10.1515/zna-1949-0501.

141. T. Holstein, S. K. Lyo, and R. Orbach, "Phonon-Assisted Energy Transport in Inhomogeneously Broadened Systems," *Physical Review Letters* 36 (1976): 891–894, https://doi.org/10.1103/PhysRevLett.36.891.

142. L. J. Charbonnière, A. F. Williams, C. Piguet, G. Bernardinelli, and E. Rivara-Minten, "Structural, Magnetic, and Electrochemical Properties of Dinuclear Triple Helices: Comparison With Their Mononuclear Analogues," *Chemistry—A European Journal* 4 (1998): 485–493, https://doi.org/10.1002/(Sici)1521-3765(19980310)4:3⟨485::Aid-Chem485⟩3.0.Co;2-8.

Biographies

Charlotte Egger studied for her BSc and MSc in chemistry at the University of Geneva. In 2025, she completed her PhD under the supervision of Prof. Claude Piguet working on the thermodynamic, magnetic and luminescent properties of polyheterometallic d-f-f helicates. She has a wide range of interests within inorganic and supramolecular chemistries and is actively involved in promoting chemistry in Geneva through the Société Chimique de Genève.

Claude Piguet earned a master's degree in music in 1983 (Oboe, Jean-Pierre Surget) and a PhD degree in coordination chemistry in 1989 (Alan F. Williams). After postdoctoral periods in supramolecular chemistry (Jean-Marie Lehn) and in lanthanide photophysics (Jean-Claude G. Bünzli), he was appointed in as a full professor of inorganic chemistry at the University of Geneva (1999, successor to Christian K. Jørgensen). Claude Piguet earned the Werner Medal from the Swiss Chemical Society in 1995 and the Lecoq de Boisbaudran Award from the European Rare Earth Society in 2009.